The Thesis Committee for Austin Ronald Baird
Certifies that this is the approved version of the following Thesis:

A Framework for Characterizing the Safety of Li-BESS using Performance Based Code Analysis and Testing

Approved by

Supervising Committee:

Ofodike A. Ezekoye, Supervisor

Kevin C. Marr, Co-supervisor

A Framework for Characterizing the Safety of Li-BESS using Performance Based Code Analysis and Testing

by

Austin Ronald Baird

Thesis

Presented to the Faculty of the Graduate School of

The University of Texas at Austin

in Partial Fulfillment

of the Requirements

for the Degree of

Masters of Science in Engineering

The University of Texas at Austin

May 2019

Dedication

This thesis is dedicated to my dad Tim, my mom Kim, my step-dad John and my aunt Christle. Thank you for supporting me in school for the past seven years.

Acknowledgments

First, I want to thank Julie Cordero and Tomas Sanchez for providing the opportunity to work in the Building & Fire Safety Department at Sandia National Laboratories. It has been a great privilege and honor getting accepted into the Critical Skills Masters Program at SNL. A huge thanks go to all the CSMP/MFP program staff for their great work and dedication to my success while at UT Austin. Additionally, I am grateful for being accepted for the National Physical Science Consortium Fellowship, that has been a great honor and achievement.

A huge thank you goes to Dr. Ofodike Ezekoye and Dr. Kevin Marr for bringing me on board and allowing me to work within the UT Fire Research Group. It has been a privilege working within the group, and I have enjoyed working with the battery team. Through their guidance and approach to problems, I feel much more confident in both solving problems and working with a team.

Next, I want to thank all my mentors and previous professors over the years from SNL and UNM. Folks such as Casiano Armenta and John Graveline have really been excellent mentors for the past seven years. Thanks to all of the engineers, professors, and others for mentoring and helping me develop over all these years.

Lastly, thanks to all the folks in the UTFRG who have helped me along the way. Robert for helping in the lab and with the volume production data, Erik for helping me learn how to code better and with the vent gas analysis, Savannah and Juliette for helping run the cone calorimeter testing and Sam for the fabrication of the custom sample trays. All the help has been invaluable.

Sandia National Laboratories is a multimission laboratory managed and operated by National Technology and Engineering Solutions of Sandia LLC, a wholly owned subsidiary of Honeywell International Inc. for the U.S. Department of Energys National Nuclear Security Administration under contract DE-NA0003525. SAND No. 2019-5141 T

Abstract

A Framework for Characterizing the Safety of Li-BESS using Performance Based Code Analysis and Testing

Austin Ronald Baird, M.S.E.
The University of Texas at Austin, 2019

Supervisor: Ofodike A. Ezekoye
Cosupervisor: Kevin C. Marr

Lithium-ion battery energy storage systems (Li-BESS) are becoming increasingly popular in consumer devices, electric vehicles, and aircraft along with industrial, commercial, residential, and utility-scale energy storage applications. Despite the growth of use cases and applications, wide-spread Li-BESS adoption is being hindered by safety concerns related to fire and explosion hazards involving these systems. In the event of thermal runaway, these systems can release flammable gases which can cause fires or explosions. The fire and explosion hazard associated with these cells depends on many factors such as the state of charge, cathode chemistry, electrolyte composition, cell form factor, cell capacity, and failure mode.

Under certain failure conditions, the lithium-ion cells that makeup Li-BESS can undergo a self-heating process. This process results from a series of exothermic reactions that can occur inside the cell. These reactions can result in an uncontrolled release of heat and energy that is commonly referred to as thermal runaway. During

thermal runaway, the battery cells can release flammable gas mixtures. This can lead to a deflagration scenario which is comparable to flammable gas and combustible dust hazards. Deflagration vents can be incorporated into systems containing lithium-ion batteries to minimize and mitigate explosion hazards. Sizing the vents requires an understanding of the battery vent gas characteristics. There are also unique fire hazards associated with lithium-ion cells. Compared to other common combustible commodities, piloted ignition of a lithium-ion cell first results in a violent release of flammable gases. This is followed by the consumption of the other combustible components that make up the cell. The overall fire hazard from a Li-BESS depends on the HRR of the lithium-ion cells, which is dependent on the propagation rate of cell failures in multi-cell modules. Currently, codes and standards do not have provisions for designing fire suppression systems for lithium-ion cells or Li-BESS. One approach to determine the flammability characteristics of lithium-ion cells is by using oxygen consumption (cone) calorimetry. Understanding these characteristics will be important inputs for performance-based analysis for both deflagration and fire safety design.

The goal of this research is to help the various stakeholders within the safety community develop an awareness of fire and explosion hazards associated with Li-BESS. This is done by understanding prescribed methods from safety codes and standards while being able to apply them to this unique hazard. Bench-scale testing flammability and analysis of gas compositions will be performed to even further understand and characterize the lithium-ion cells.

Table of Contents

List of Tables

List of Figures

Chapter 1

Introduction

1.1 History of Safety and Emerging Technology

Industrial safety has improved over the last 100 years through the development and enforcement of industrial codes and standards. In the late 1800s, as hot water boilers became more popular, safety issues materialized. In the early 1900s boiler explosions in Massachusetts caused concern among the community. These events eventually led to the development of the Boiler and Pressure Vessel Code from the American Society of Mechanical Engineers (ASME) (1). Multiple incidents in Massachusetts occurred before the safety community reacted and developed the first boiler code. This historical example shows the need to proactively understand hazards and develop safety guidelines.

Again, in the late 1800s through the mid-1900s, multiple incidents caused community-wide concerns. The National Fire Protection Association (NFPA) developed numerous codes and standard to help combat fire-related incidents. Fires such as the Great Chicago Fire in 1871, Ohio State Penitentiary Fire in 1930 and the Cocoanut Grove Nightclub Fire have led to the development of various codes and standards. Increasing safety for construction materials, life safety codes, and requirement of fire detection and suppression (2) are examples of the increased level of safety. Yet even with the safety and prevention techniques such as smoke removal, stairwell pressurization, and fire detection and suppression, tragic incidents are sometimes the only drivers for communities to adopt and enforce established codes and standards. In 1980 the MGM Grand casino did not use sprinklers throughout the casino, even as they became more common at the time. When a fire erupted, sprinklers would have prevented or slowed the rate of fire spreading throughout the structure. Without automated notification and suppression systems, mass confusion caused unnecessary causalities and property destruction. In contrast, a similar fire in 2008 at the Monte Carlo casino, which did have automated suppression, detection and notification

systems, had no causalities. The damage was minimal and the resort reopened three weeks later. This shows that not only do safety systems and requirements need to be established, but also properly communicated, implemented and inspected (3).

In addition to fire hazards, explosions have caused many tragic incidents. In the late 1800s, a flour plant in Illinois had an explosion that resulted in one causality and multiple structures being destroyed (4). This resulted in NFPA recognizing combustible dust as a hazard. As other incidents occurred, a committee (NFPA 68) was formed to develop standards on explosion protection systems (5). Even with such an early awareness of the hazard, combustible dust incidents still are present in the 21st century. The Occupational Safety and Health Administration (OSHA) creating a Combustible Dust National Emphasis Program (NEP) in 2007 (6).

As new technologies emerge, the hazards posed by the technology are largely unrecognized until tragic hazards occur. As technologies emerge more quickly and deploy more broadly, it is important to develop processes to address safety challenges. This approach can help proactively protect lives, structures, and integrity of emerging technologies.

1.2 Lithium-Ion Battery Energy Storage Systems

The use of lithium-ion cells is rapidly increasing in today's society. They are used at the consumer electronics level to transportation systems and even to grid-level energy storage. At larger fixed-installation sizes, lithium-ion battery energy storage systems are becoming frequently from residential applications to electrical grid scale. In the design of these systems, engineers must balance performance, cost, size, packaging and safety concerns.

1.2.1 Basic Lithium-Ion Battery Understanding

Over 25 years ago, Sony Corporation first introduced the consumer rechargeable lithium-ion battery to the market for use in hand-held electronics. They used lithium cobalt oxide (LCO) for the cathode chemistry, helping give the ability to bring the concept of a "rocking chair" or rechargeable battery to the commercial market. The Li_xCoO_2 cathode was discovered by Dr. John Goodenough in 1980 (7).

The basic principles of a battery can be related to a water tower analogy. The potential or voltage (V) is based on the overall height of the water tower. The capacity (Ah) is analogous to the total mass/volume of water that can be held in the water tower. For a water tower, the total energy is the product of the height and volume of the water tower. For a battery, the energy is the product of the capacity and potential (Wh). The power (W) is the rate of energy transfer. Lithium-ion cells consist of a separated anode and cathode.

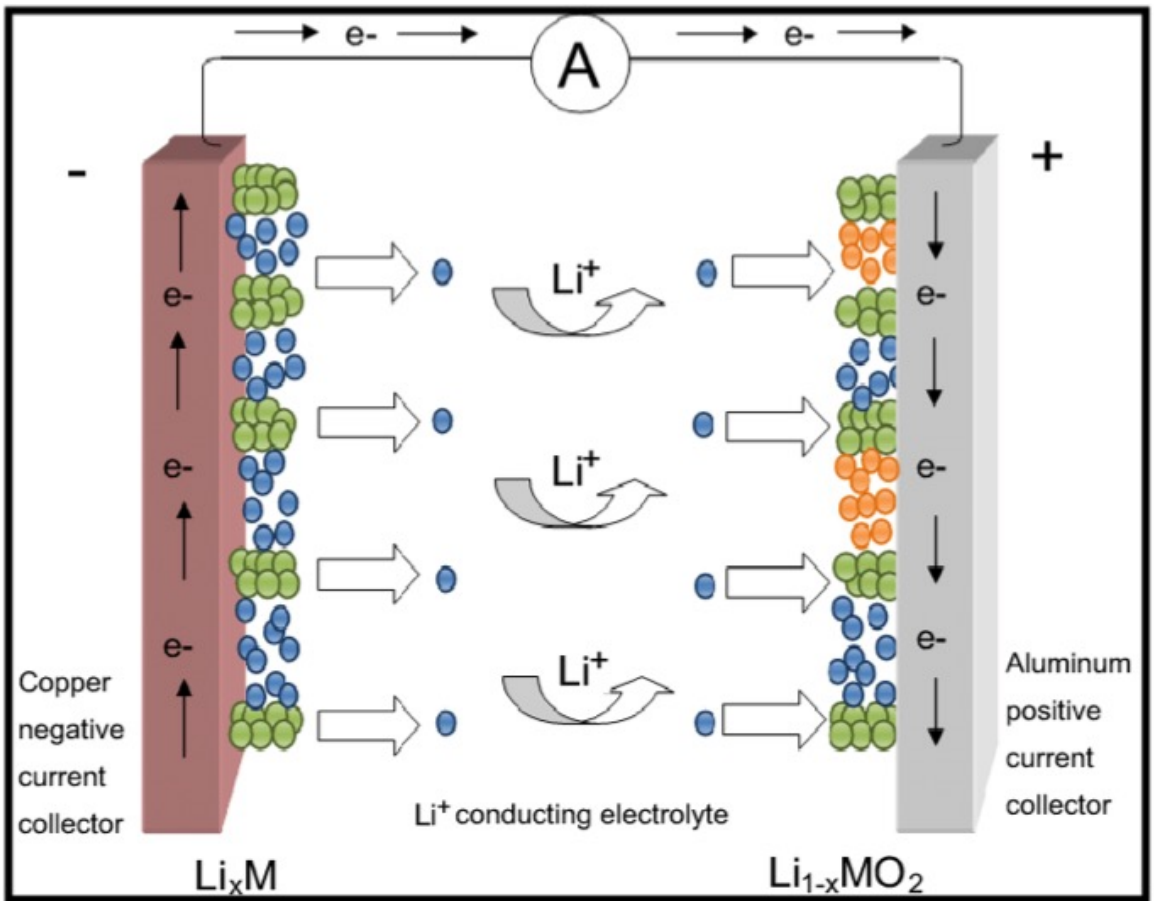

Figure 1.1: Lithium-Ion Battery Charging Schematic

Figure 1.1 above shows the lithium-ion transportation during the charging or discharging process from Bensalah et al. (8). The lithium ions move from the cathode to the anode upon charging and then when discharging move in the opposite direction. An electrolyte is introduced into the separator to promote ion transport during charging and discharging. The charge rate or C-rate is the rate at which the cell can be charged or discharged. For example, a 1000 mAh cell rated for 1C can be charged at 1000 mA. Starting from the discharged state, after one hour this cell should be fully charged. Most manufacturers are conservative on this value to prolong the life of the battery. The State of Charge (SOC) gives an indication of what the capacity level is at based on the nominal voltage range the cell is designed for. The State of Health (SOH) is an indication of how much the cell capacity has faded with respect to a brand-new cell.

Lithium-ion cells are designed with various form factors, capacities, cathode and electrolyte chemistries. A cylindrical cell can be compared to a standard AA or AAA cell in terms of the form. Coin or button cells are similar to a watch battery. Pouch cells are common in phones and are thin and rectangular in shape. They are constructed with a soft pouch encasing the anode, cathode, and separator with two tabs sticking out of the end. Prismatic cells can be compared to car batteries in terms of construction. There are a large variety of cathode and electrolyte chemistries. Cathode chemistries include lithium iron phosphate (LFP), lithium cobalt oxide (LCO), lithium nickel manganese cobalt oxide (NMC), lithium manganese oxide (LMO) and lithium nickel cobalt aluminum (NCA). Each chemistry has various specific energy density (Wh/kg), specific volume (m^3/kg), cost, and application. Additionally, numerous electrolyte chemistries exist, such as ethylene carbonate (EC), dimethyl carbonate (DMC), ethyl methyl carbonate (EMC), diethyl carbonate (DEC), propylene carbonate (PC), and methyl propyl carbonate (MPC).

1.2.2 Safety Concerns

With Li-BESS as an emerging technology, different risks and hazards are presented. This drives the need for analysis to ensure systems are safely integrated at all levels. Energy storage systems can serve a multitude of different roles and purposes. Grid peak shaving can be done when the electrical demand on the grid exceeds the supply, energy from the Li-BESS can be used to compensate. These systems can also be used for establishing a means to store energy from renewable sources such as wind turbines or solar systems. Additionally, backup power is another potential use for Li-BESS. Due to the multitude of functions these systems can have, a greater understanding of how to safely manage them is necessary.

Achieving the desired level of safety is especially important in applications for military, aircraft, spacecraft and in densely populated environments where a Li-BESS failure could lead to a high consequence (9). While performance measures are generally well characterized for battery designers, safety aspects are not well-defined. A catastrophic

failure can occur due to manufacturing defects, thermal abuse, electrical abuse or mechanical damage. Although failure rates are frequently measured and found to be very low, the consequences can be very high, and the fire and explosion hazards must be considered and understood.

Certain failure modes within lithium-ion cells can lead to an exothermic reaction within the sealed cell This cell can then go into thermal runaway. In thermal runaway, reactions increase the overall cell temperature. This builds pressure in the cell and can ultimately lead to rupture and off-gassing from the cell. During thermal runaway, battery cells can generate large amounts of flammable gas consisting of hydrogen, carbon monoxide, and carbon dioxide along with various hydrocarbons such as methane and propane. This can result directly as either a fire, deflagration or combination of both hazards.

1.2.3 Recent Failure Events

There are many examples of lithium-ion cells entering thermal runaway, causing fires and explosions. On small-scales, thermal runaway can be seen regularly in failures of consumer devices such as portable electronics including mobile phones, laptops, and e-cigarettes. Failures with e-cigarettes have caused them to explode near users face head and neck area, causing life-threatening injuries (10). Examples of other consumer electronic incidents are issues with the Samsung Note 7 phone. In 2016 when the phone was plagued by numerous reports of fires and overheating. It took nearly 100 reported incidents in two weeks before the US Consumer Product Safety Commission recalled the devices. The issues were initially diagnosed incorrectly, as a replacement phone that was powered down and unplugged caught fire on an airplane. The investigation showed that there were batteries supplied by two different companies, each with their set own issues. One set, from Samsung SDI, had issues with the tolerance between the battery pouch and the internals of the phone. This caused the electrodes to crimp and short circuit. The batteries from Amperex Technology Limited had quality control issues when the insulation tape was missing on some cells. Additionally, other cells had sharp edges that caused short-circuiting (11).

Regardless of the issue, minor oversights by a well-known and versatile company such as Samsung caused major issues that led to a potential aircraft fire. Consumers also reported burns and injury from the Note 7 cell phone failing. Recently, the computer manufacturer Hewitt & Packard recalled over 100,000 laptops for fire and burn hazards after eight reports of melting and charring since January of 2018 (12). This shows even after previous incidents, new failures still occur.

Larger fires have been reported and investigated within electric automobiles. One example comes from the 2011 Chevrolet Volt crash testing. After the test was completed, the vehicle caught fire over the weekend when no lab personnel was present. The Chevrolet Volt had been involved in a New Car Assessment Program (NCAP) pole test three week prior to the fire (13). This is an impact test with a solid pole for crash testing ratings. During the investigation, it was determined the battery was damaged but only over time did it catch fire. While it was difficult to repeat the failure and fire, this example shows how dangerous and volatile lithium-ion cells can be. In addition to regular use, disposal and recycling of lithium-ion cells require safety considerations. Tesla automobiles have had numerous failures over the past few years. Various incidents range from battery issues caused by crash damage, issues with charging stations, improperly tightened electrical connections, and other issues (14). Each fire reported was very difficult for first responders to control and took hours and up to a whole day to completely extinguish. In some cases, the car reignited days later after the initial fire was extinguished (15). Recently, a Tesla Model S caught fire in Shanghai, China. The vehicle was not in use and parked in a monitored parking garage. Gas started to rapidly vent from the vehicle before igniting causing a large fireball then the whole car was engulfed in flames (16).

The Federal Aviation Administration will not allow lithium-ion cells to be transported in aircraft unless installed in consumer electronics at a state of charge of 30% or lower. This comes after multiple incidents on flights and three aircraft accidents attributed to planes transporting lithium-ion cells. One of those flights was UPS Airlines flight 6 leaving Dubai headed for Germany. The plane contained a large quantity of lithium-ion cells and other

combustibles. A large fire developed, which caused smoke to enter the cockpit. This made it nearly impossible for the pilots to see their instrument clusters. Additionally, the fire caused life support systems to malfunction along with structural components within the plane to fail. This made it difficult to control the plane as the functionality of the systems failed. Unfortunately, the crash resulted in no survivors. In the causal analysis, the fire detection methodology was determined to be inadequate due to the delay from the pallet of cells being covered. This can be read in the report by the FAA (17).

An example of a larger, industrial scale explosion incident is the 2017 train car explosion in Houston, Texas. The train car explosion was caused by discarded lithium-ion cells being transported to a recycling facility. The explosion was so violent windows broke on buildings about 500 feet away (18; 19). Large fire events have also occurred. In 2017, a containerized lithium-ion ESS burned at a utility plant near Brussels, Belgium. The ESS in Belgium was equipped with fire detection and suppression which failed to extinguish the flames (20). In 2018 a cement plant in Jecheon, North Chungcheong Province experienced over $3 million in damage. This was the 15th reported ESS fire in Korea this year (21).

These different incidents show the consequence of what can happen if safety systems are not properly designed, installed, commissioned and maintained for devices that use lithium-ion cells. There are hundreds if not thousands of other reported issues over various scales from small consumer electronics all the way to complete Li-BESS engineered systems. Even small scale systems ranging down to consumer electronics can cause incidents and are a safety hazard. At the SNL 2019 ESS Safety & Reliability Forum, the number of incidents initially reported as 15, which was disputed for the Korea ESS incidents to be anywhere from 15 to 40. With no central repository of Li-BESS incidents, it is difficult to have the facts correct. So, while multiple regions and countries are using the Li-BESS and having similar failures and incidents, there is no way to keep track and update one another on what exactly is happening. This shows a large gap that needs to be closed to reduce incidents and learn from one another. To this day, there are reports of 21 fires occurring in South Korea per other sources (22). This shows how inconsistent reporting of these incidents is.

It is also not clear what safety systems are installed in each of these incidents and how they affected the outcome.

While writing this thesis, a devastating incident occurred in Surprise, Arizona on April 19th, 2019. A passerby noticed smoke coming from the substation site, who then called first responders. A Li-BESS caught fire in the substation prompting the fire department response. A hazmat team was called on site. While trying to investigate the Li-BESS, an explosion in a substation occurred. Eight firefighters were injured, with four being transported to the hospital and one in serious condition (23). It has been reported the explosion caused both chemical skin burns and chemical-inhalation burns (24). A lot of the personal protection equipment the firefighters were wearing was damaged and/or ripped off of the firefighters when the explosion occurred. With details still emerging, it is unclear what the exact cause of this incident is, as numerous investigators are on the scene (25). Fortunately for everybody, there were no fatalities. This incident comes after a 2012 fire had already occurred in Surprise, Arizona (26). After the 2012 incident, various safety improvements have been established such as improving ventilation between cabinets, monitoring of systems and remote alarm capabilities. Even with these improvements, there was still a safety incident seven years later.

These recent incidents show that even with prior knowledge and understanding of Li-BESS failures from incidents that have occurred previously, there is still a lack of understanding and safety of these systems. As meetings, forums, discussions and other methods to learn and improve the safety of Li-BESS are being coordinated, it is clear there is a large gap in the technology advancement verse the safety systems. These incidents show the absolute need to improve and enforce safety systems and methods for Li-BESS right away.

Based on the incidents, there are clearly two hazards from lithium-ion cells and Li-BESS. The first is the fire hazard, which requires an understanding of both the fuel loading and the unique challenge to design and integrate a suppression system into Li-BESS.

Sizing systems to extinguish a Li-BESS fire is a challenge. If special fire protection systems are used such as carbon-dioxide or vapor systems, they must be sized for potentially long-lasting fires and to be fully functional after multiple uses. Explosion hazards need to be mitigated, as shown by both the Houston train car and the Surprise, Arizona incidents. Both hazards exist, and if the fire is extinguished and vent gas is still being produced, this leads to an explosion hazard as flammable gas accumulates. A Li-BESS is a unique hazard and requires an understanding of both the fire and explosion hazards.

1.3 Contents of Thesis

Lithium-Ion Battery Energy storage systems are becoming much more popular and widely used, yet its obvious that there is a lot to understand and learn still regarding the safety analysis. Codes and standards are slowly emerging for this new technology, but they will need to be revised and updated as studies and awareness increases. Yet as with the history of codes and standards as previously mentioned, they tend to be slower than the pace of the technology development. Historically, it takes accidents and/or incidents to bring awareness to the types of problems these technologies present. Different methods to help prevent lithium-ion battery-related incidents can be implemented based on both quantitative and qualitative analysis and understanding. The objective of this thesis is to help evaluate what might lead to a Li-BESS failure. Additionally, the explosion and fire hazards will be characterized. By comparing the characteristics with well-known hazards, existing codes and standards can be modified and used for this upcoming technology.

Chapter two will help cover the failure modes in addition to considerations and brain-storming of what oversights might lead to failures. Additionally, listings of different codes and standards relevant to Li-BESS will help understand what already has been done and what new info/data can be used to mitigate the hazards associated with these systems. Chapter three will show how to characterize the off-gas composition and compare with other similar hazards such as flammable gases and combustible dusts. Different models will estimate the lower flammability limit, laminar flame speed, and maximum overpressure.

These values will then be compared and used to show how to apply code-based deflagration vent size calculations from NFPA 68 to an example application. Some of the effects of obstructions and partial-volume calculations will be performed to further understand how this prescribed method works. Chapter four will provide insight on the fire hazard associated with lithium-ion cells. The heat release rate (HRR) and total heat released will be measured with an oxygen consumption cone calorimeter. The data from this testing can be used to compare lithium-ion cells with other fire hazards and commodities. Better fire and fuel load characterization of cells will support the development of sprinkler design guidelines for lithium-ion cells and Li-BESS. Chapter five will conclude the thesis and help breakdown and understand what additional work needs to be done to further development of Li-BESS safety.

Chapter 2

Understanding of Failures and Hazards

Many factors can lead to a catastrophic failure within Li-BESS. Failures can arise due to a manufacturing defect, inadequate cooling to the battery rack or even at a module level, overcharging, over-cycling, and other component and/or system defects. By using a parameter diagram, the inputs and consequence/outputs can be visually explained for the Li-BESS as seen below:

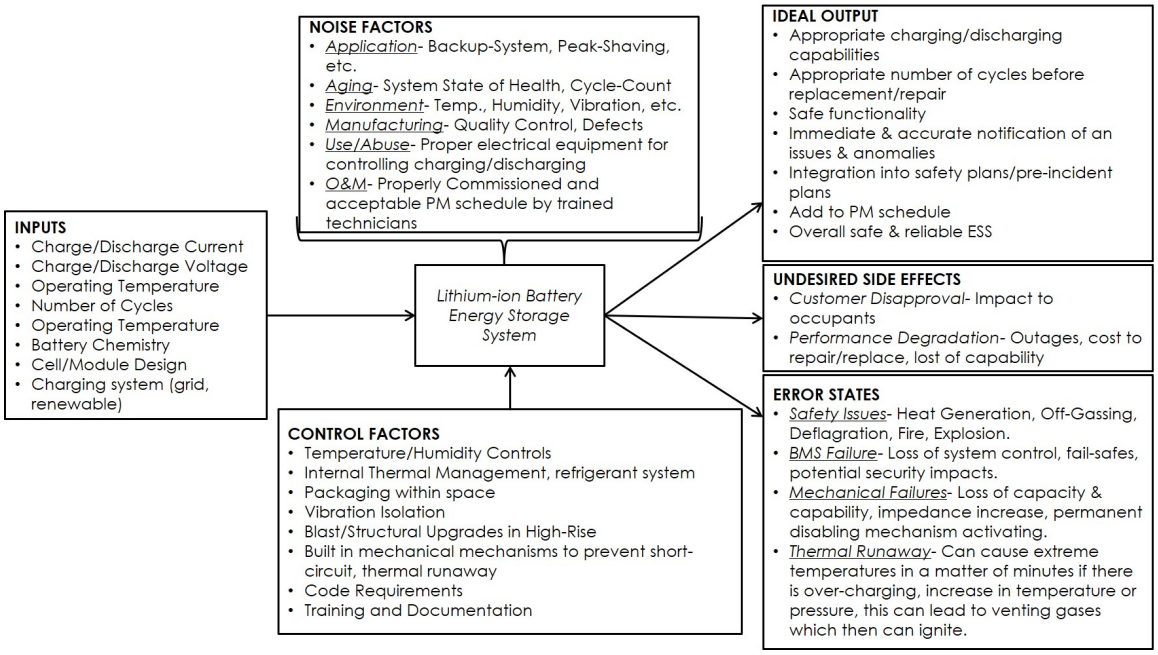

Figure 2.1: Parameter Diagram for Energy Storage Systems

Through the construction of parameter diagrams shown in figure 2.1, control factors, and system noises have been established to help the safety community understand how a Li-BESS operates. These parameter diagrams also show what error states may occur, giving a baseline of what issues must be addressed. Parameter diagrams are generated to establish a greater understanding and visual aid of how different systems interact. Safety

or failure of Li-BESS might evolve from issues involving system ventilation, inspection, testing and maintenance (ITM) scheduling, system commissioning, cooling systems, battery management systems and more. The inputs are derived from potential performance-based requirements such as the capacity, energy density, along with the operating voltage and current. The application type is important to understand for operations such as peak shaving or renewable energy since cycling and usage effects the life of the system. Once these inputs are established, control factors to maintain Li-BESS safety and reliability are used. Examples of control factors can be engineering packaging and mechanical safety mechanisms, along with guidance from codes and standards. Different noise factors such as the environment that the Li-BESS is installed in, the type of usage or over-usage, how the quality control and commissioning are executed can make a difference on whether the system operates correctly. If each of these different noise factors is considered and means to mitigate and prevent them are established, an ideal output with a reliable, safe system will be the outcome. If proper control factors are not executed, error states and undesired side effects such as system failure, safety issues, and customer disapproval will result. By using a recognized approach in the high-level analysis, this should aid in spreading awareness with familiar and established methods. One of the main issues, as seen in the error states, is a thermal runaway, which can cause pressure to build in the cell, ultimately rupturing and off-gassing. This is where fire and explosion hazards develop and must be mitigated.

2.1 Li-BESS Breakdown

Lithium-ion battery energy storage systems are constructed from numerous individual cells. The following explains the hierarchy of how each component in the Li-BESS is related:

Figure 2.2: Lithium-Ion Battery Cell

- Battery Cell- the individual battery cell with an anode, cathode, separator material, and electrolyte. There are multiple geometries such as cylindrical, coin/button, pouch and prismatic as shown in figure 2.2 above (27).

Figure 2.3: Lithium-Ion Battery Module

- Module or pack- multiple cells enclosed in either a series, parallel or combination of series and parallel as shown in figure 2.3 above (28).

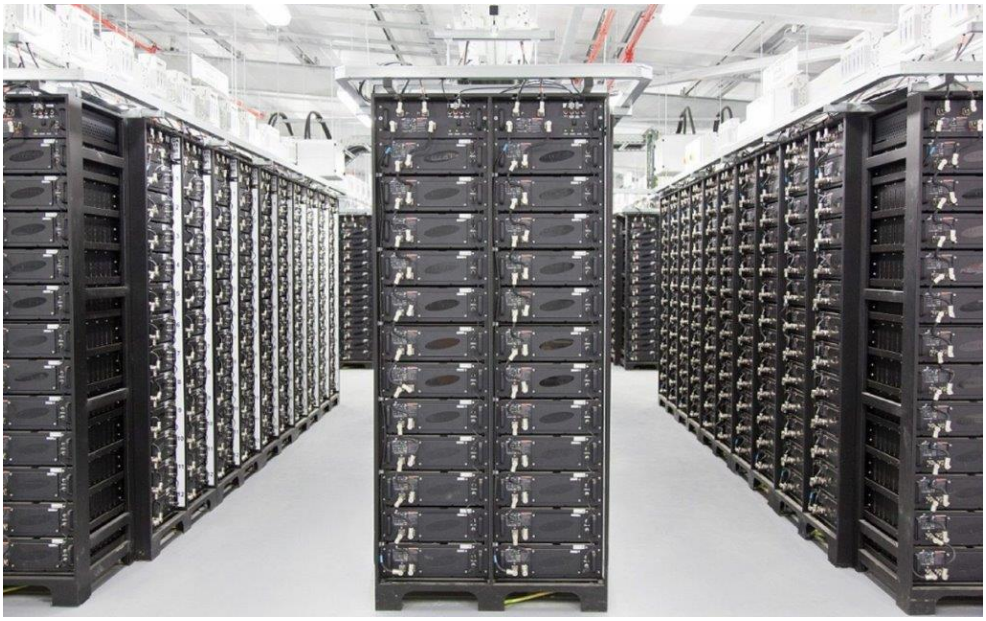

Figure 2.4: Lithium-Ion Battery Racks

- Rack- Multiple module/packs enclosed with control systems, battery, and thermal management systems and connections to make the Li-BESS work properly as shown in figure 2.4 above (29).

- Battery Management System (BMS)- Control system for an energy storage system. Controls current and charging/discharging cycles

- Thermal Management System (TMS)- Controls cooling and heating system to ensure battery cells stay within predetermined set points

2.2 Failure Modes

Failures at the cell level can be summarized by the following list:

- Manufacturing Defects- Inadequate quality control or foreign material introduced between the cathode and anode causing a short

- Thermal Abuse- Lack of adequate cooling, failure of the cooling system, and/or operated or stored outside of manufacturer specified temperature range
- Electrical Abuse- Overcharging/discharging, external short circuit and/or wiring not sized properly
- Mechanical Abuse- Physical damage to the system from abuse or fatigue or lack of vibration isolation

There are a significant number of variables that can cause several different failure modes. Creating fishbone diagrams can help visualize the different layers of issues that can lead to system failure. They provide a starting point on identifying some effects of individual systems or processes on the overall system. These fishbone diagrams are based on discussions within the UTFRG Battery Research Group and are designed to help bring up potential hazards and issues with Li-BESS.

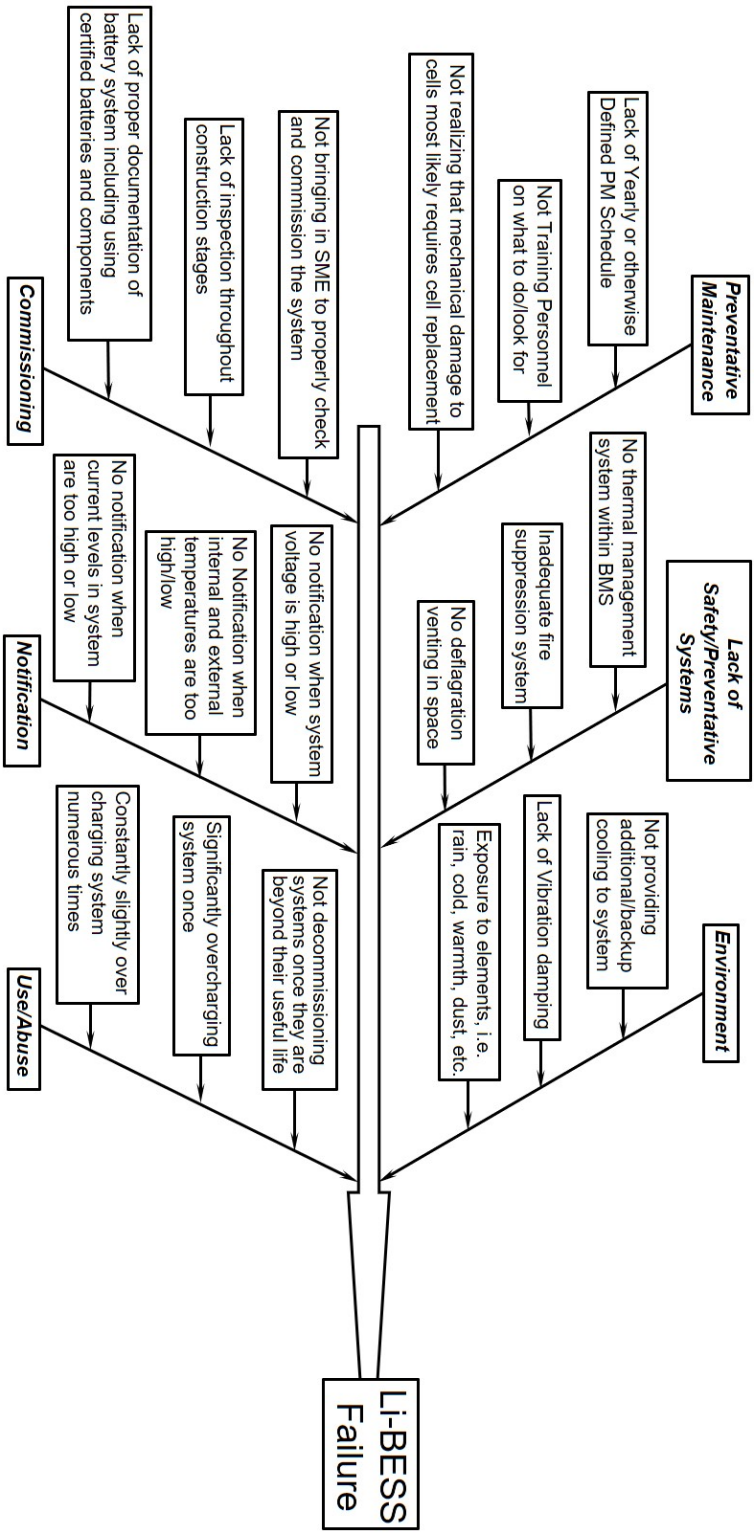

Figure 2.5: Overview Fishbone Diagram for Li-BESS

Figure 2.5 shows the general high-level overview for what can affect a Lithium-ion battery energy storage system and how each might fail. The six main points of failure captured are (1) preventative maintenance, (2) lack of safety and prevention systems, (3) the physical environment the system is installed in, (4) commissioning of the system, (5) notification of system issues, and (6) overall use or abuse of the system. There are additional details associated with each of the levels associated with the operation of a Li-BESS, each which is further covered in the following figures. While these six main components were identified, there could be others that are not identified in this analysis. The following six figures will show different lower level issues. With fishbone diagrams, multiple levels of potential failures can be identified. In this analysis, two levels are identified.

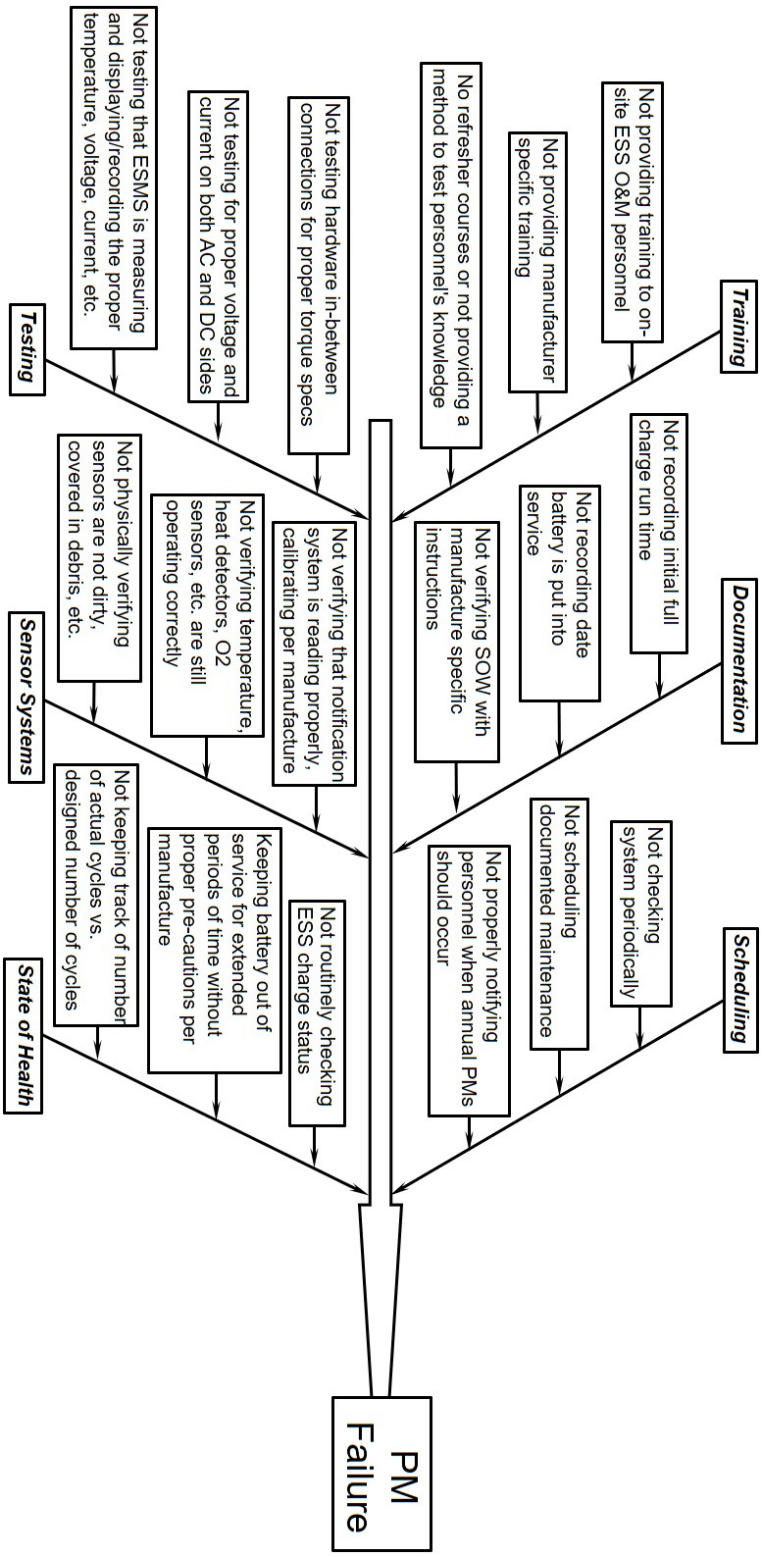

Figure 2.6: Preventative Maintenance Fishbone Diagram

Figure 2.6 shows the breakdown of errors that might occur associated with overall system maintenance. The factors shown associated with preventative maintenance failure are (1) training, (2) documentation, (3) scheduling, (4) testing, (5) sensor systems and (6) the state of health. There can be a breakdown in the training of personnel and manufacturer specific operation methods. Additionally, not having documentation and scheduling can hinder the ability to proactively prevent failure with Li-BESS. Preventative maintenance is intended to help prevent failures and unplanned outages or system shutdowns. One example might be that every year a specific breaker in a Li-BESS must be replaced to ensure it does not fail during standard operation. Depending on how critical the equipment is, availability of spare components, and other factors, system maintenance may be as scheduled needed or using the predictive/preventative algorithm. In some cases, such as Li-BESS, system failure may lead to a safety incident or hazard. This suggests the need for a preventative maintenance method in which the system health is monitored to ensure safe operation. By tracking the state of health, for example, metrics can be established and monitored to diagnose changes in system health. Indications of such changes can then lead to scheduling planned outages such as replacement of cells, modules, racks or the whole system. Measuring temperature changes, any vent gas production or trends in incorrect charging/discharging rates can help identify early failures in order to maintain system safety and reliability. Furthermore, testing the SOH, charging and discharging currents, voltages, and other parameters might be required outside of normal usage depending on how the system is operated. This might be an annual or semi-annual test that is used to monitor the whole system and determine what repairs or replacements are required. Additionally, proper training and documentation are crucial to make sure nothing is overlooked from a maintenance perspective.

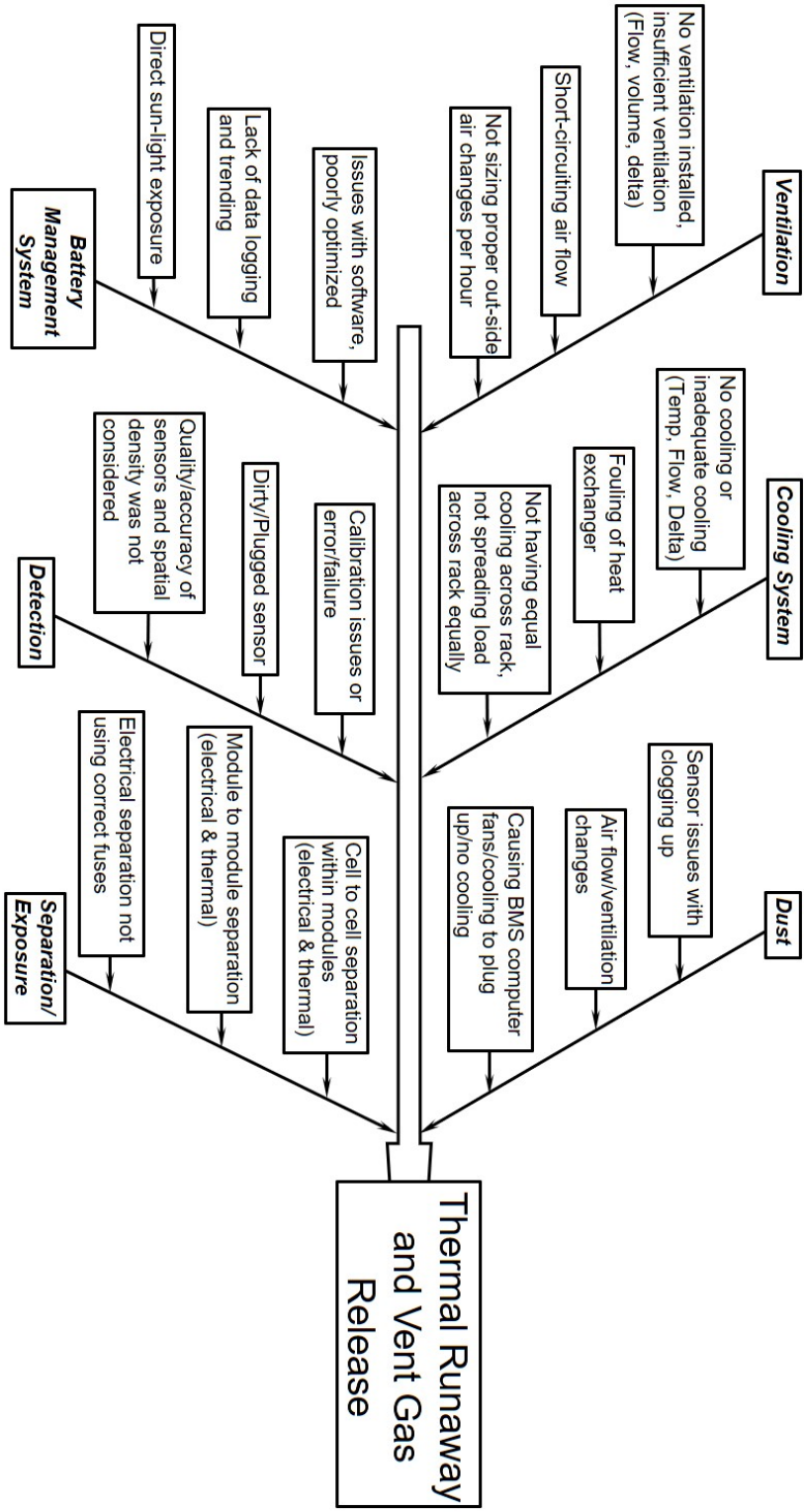

Figure 2.7: Safety and Preventative Systems Fishbone Diagram

Figure 2.7 show how lack of different safety components and parameters might lead to a failure in Li-BESS. The various potential failures of the safety and preventative systems identified above are (1) ventilation, (2) cooling systems, (3) dust control, (4) battery management system, (5) detection and (6) separation/exposure. Ventilation and cooling systems are important to prevent self-heating and thermal runaway. They must be sized properly in addition to being protected from the elements. Contaminates such as dust can reduce air flow and is an environmental factor that must be accounted for. Further discussion on this will be provided below. The battery management system should identify cooling system issues and initiate fail-safe activities such as system shutdown and user notification. Fail-safe activities can include reduction of system capacity or shutting the system down completely. To reduce the capacity, potentially discharging the whole system would lead to a lower potential consequence if a failure were to occur. The rate of discharge is important to establish as discharging too fast could heat cells and can actually cause additional failures. Detection of failures and anomalies is important to feedback into preventive maintenance trends and help understand the overall SOH of the system. The data-logging should be controlled and interpreted by the BMS, as it needs to monitor and control the whole system in the event there are error states. If separation and isolation systems both mechanically, electrically and thermally are not implemented, one single failure can quickly propagate throughout the whole system. Exposure due to lack of separation between cells and/or modules can lead to a complete system failure.

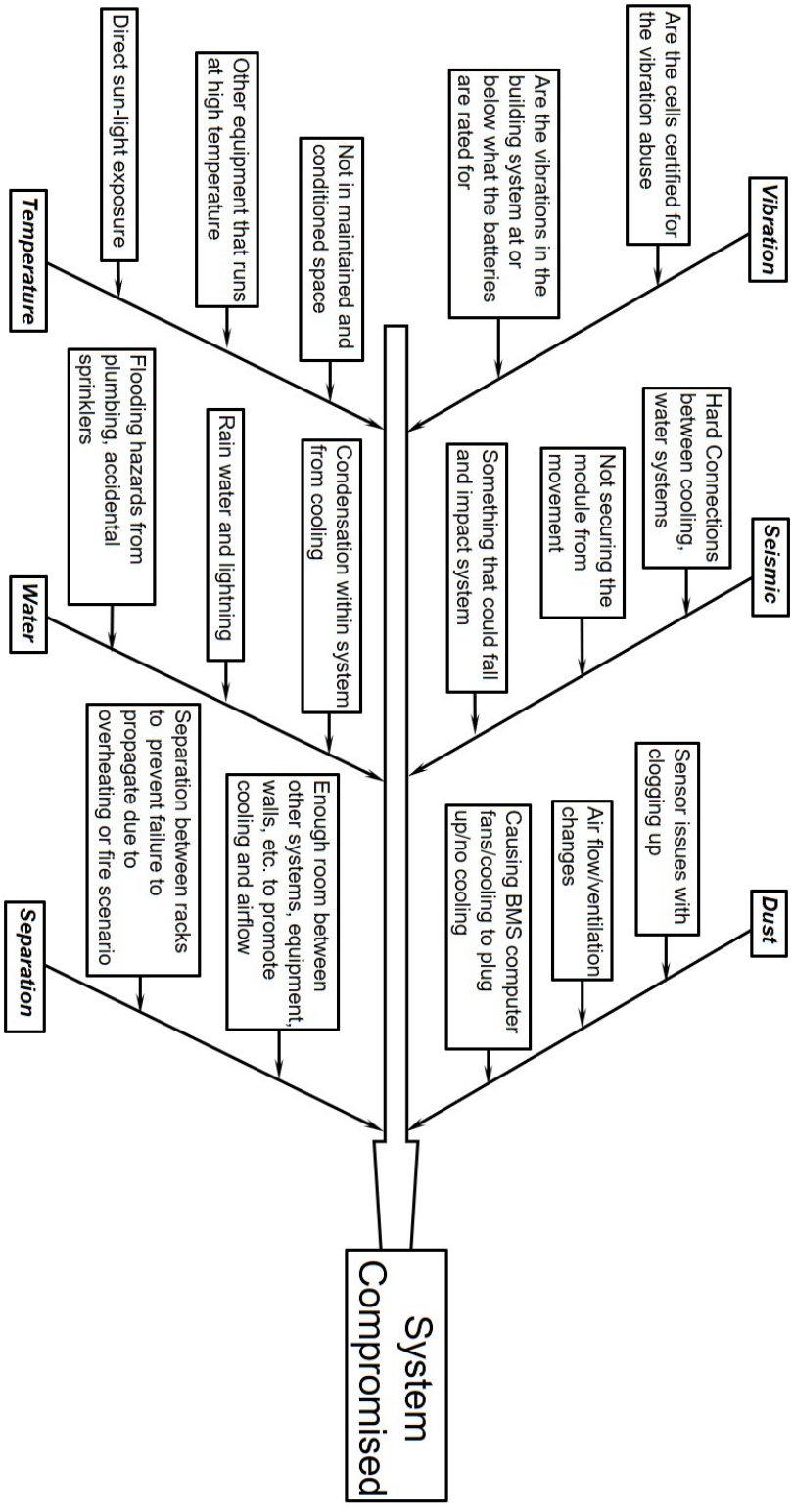

Figure 2.8: Environmental Impacts Fishbone Diagram

Figure 2.8 shows the overall effect or potential issues that might be caused by the surrounding environment of the Li-BESS. Environmental impacts on Li-BESS include (1) vibrations, (2) seismic, (3) dust, (4) temperature, (5) water and (6) separation. Some of these have been previously covered, as each fishbone does interconnect at certain levels. While fire and explosion hazards are considered, other failure protection such as vibration and seismic damage. With the idea that Li-BESS would be installed in mechanical or electrical rooms that are not necessarily cooled, heated, cleaned or environmentally friendly spaces, there are complications that may arise. Vibration from other equipment such as chillers, fans, compressors, and other large equipment may cause tabs on pouch cells to become damaged or the pouch itself to wear out. Environmental impacts such as extreme temperatures or even water may be an issue depending on the quality of construction and location of the actual Li-BESS. Perhaps the system must be raised such that flooding will not cause an electrical malfunction or damage the system. Separation from other equipment might be difficult based on whether it is new or existing space. These issues might lead to different error states that may take time to arise. Shorting out, thermal runaway or physical damage can occur if the environment and system are not matched properly.

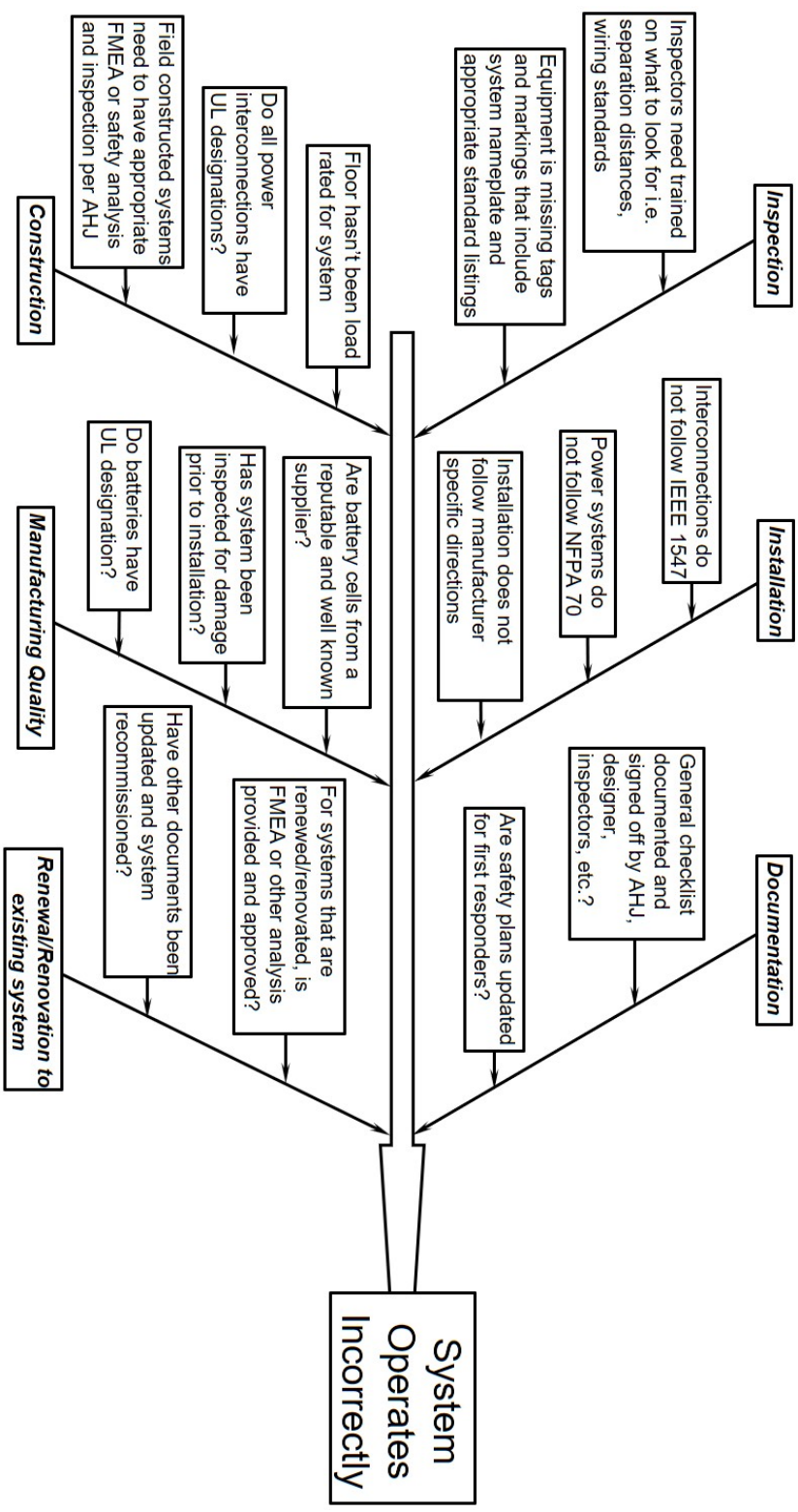

Figure 2.9: Commissioning Fishbone Diagram

Commissioning errors can lead to both long-term and short-term issues and need to be well understood and executed. Figure 2.9 shows some of the potential errors and issues that might lead to system failure. The main errors associated with commissioning Li-BESS is (1) inspection, (2) installation, (3) documentation, (4) construction, (5) manufacturing quality and (6) renewal/renovation of the existing system. With such a new technology that many contractors and designers may not be familiar with, documentation and inspection are crucial to ensure nothing is overlooked. Some literature does exist to provide guidance for the ESS plan review and inspection process. The Pacific Northwest National Laboratories and Sandia National Laboratories Energy Storage System Safety: Plan Review and Inspection Checklist provides a framework for identifying potential issues before they become an incident (30). Having correct listings, reputable suppliers and manufacturers, along with inspecting the systems prior to accepting and installing are crucial to ensure a reliable system. Pre-incident plans and first responder awareness needs to be updated and established during this process and prior to system operation. This directly ties into the next fishbone diagram regarding incident prevention and notification. Additionally, with these systems installed in existing buildings, ensuring both the electrical and building infrastructure need to be verified to handle Li-BESS. Proper documentation and approval of renovated systems must be enforced. This ensures safety is not compromised even on existing systems no matter the level of replacement.

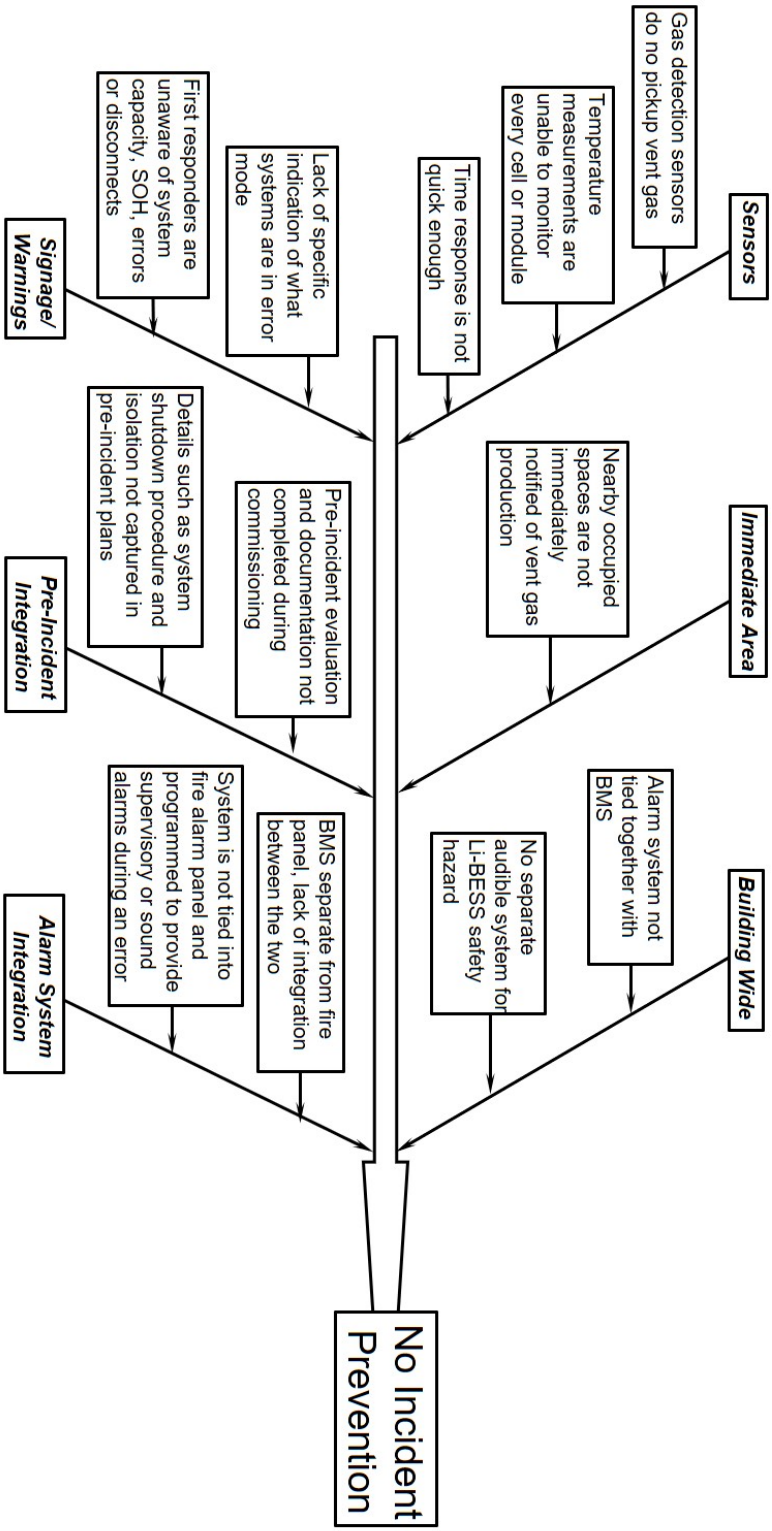

Figure 2.10: Notification Fishbone Diagram

Figure 2.10 shows some of the notification and prevention systems that should be in place to help prevent or catch potential incidents or hazards before they occur. Some of the main notification issues can come from lack of (1) sensors, (2) immediate area notification, (3) building wide notification, (4) signage and warnings, (5) pre-incident plan integration and (6) alarm system integration. Having sensors monitoring temperatures and gas release and providing feedback into BMS is important in identifying errors in the system. The time response on these sensors is also important, as minutes or seconds are important when dealing with potential life safety issues. It is important to have occupant notification in both the immediate area and building-wide in the event of an accident. Integration of a BMS that is monitoring the systems with the fire panel can help proactively prevent life safety issues. Additionally, this can help first responders understand the accident and failures by reviewing the fire alarm panel. This again goes directly into the documentation as shown in figure 2.9. Knowing which specific rack in a complete Li-BESS is failing is important for first responders as they determine what actions to take.

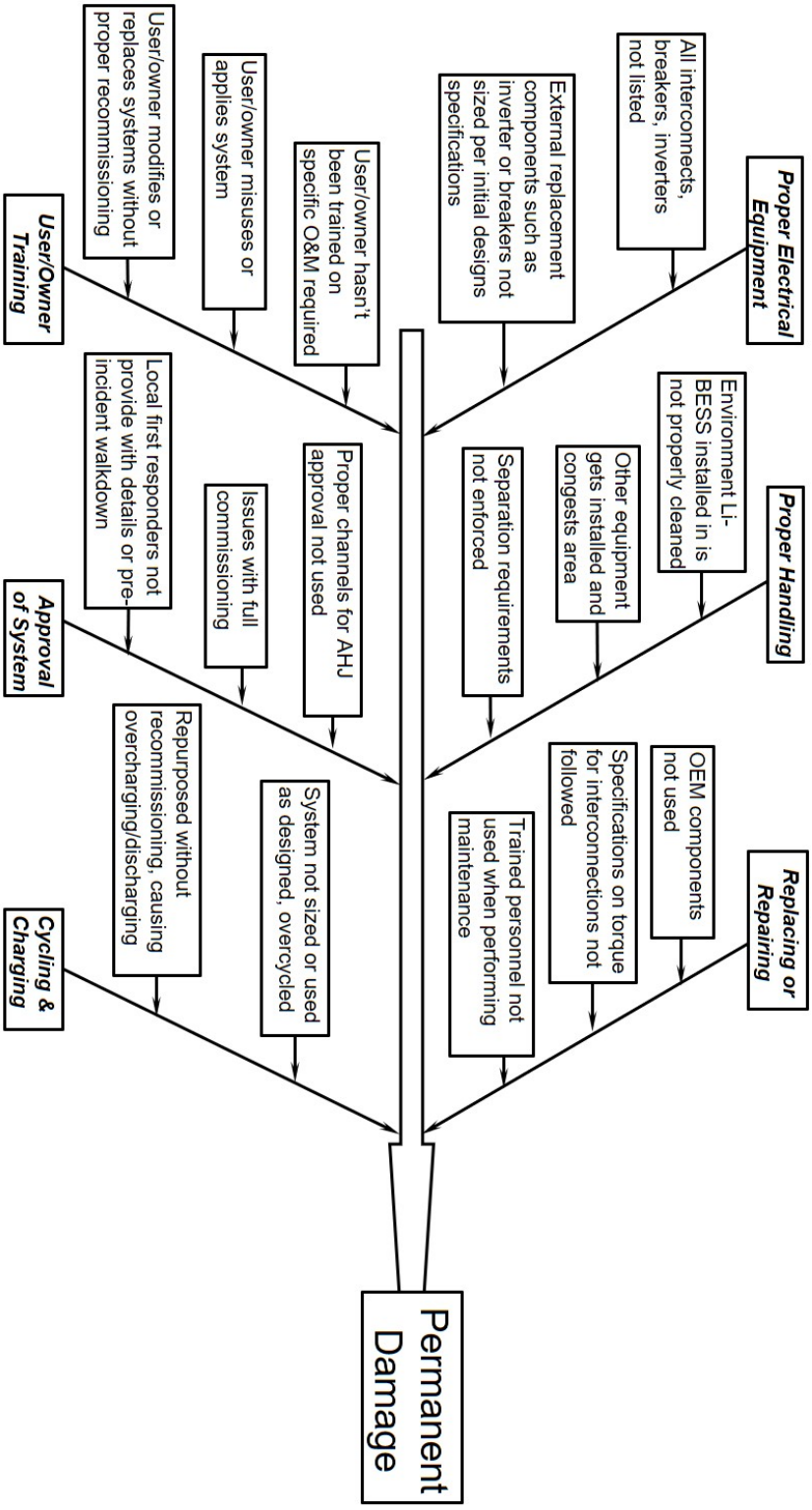

Figure 2.11: Customer Interactions Fishbone Diagram

Figure 2.11 is the last fishbone diagram described and shows potential errors and issues from improper usage. The issues captured are (1) proper electrical equipment, (2) proper handling, (3) correct replacement or repairs, (4) user/owner training, (5) approval of system and (6) proper cycling/charging. Once a Li-BESS has been approved, installed and commissioned the designed safety systems are temporarily fixed. If changes are made to the Li-BESS, such as components replaced, operational parameters changed, or the environment and separations not maintained, this could cause an issue that is not accounted for in the original safety design. By changing the overall operation and purpose, the system may be cycled incorrectly or over-charged/discharged. When the user or owner has the system turned over to them, these issues should be explained and understood due to the potential safety issues surrounding Li-BESS.

2.2.1 Li-BESS Explosion Hazards

This section will compare some of the known hazards of Li-BESS and how they relate to known industrial hazards. From the known failures, an explosion hazard exists due to lithium-ion cell failure. This failure can be related to other hazards such as flammable gas and combustible dust. Explosion hazards are based on inputs from what can be called the "explosion pentagon" in which an oxidizer, ignition source, fuel, confinement, and dispersion need to exist and based on each of those five parameters, an explosion can occur. Examples of explosion hazards are natural gas plants, hydrogen facilities, gas transportation through piping systems, evaporating solvents as part of a process or large chemical spills. Based on the volume of the room and the volume of flammable gas released, the fuel concentration will vary, and this will change the parameters such as flame speed and theoretical maximum overpressure. Additionally, combustible dusts are another known industrial explosion hazard. These range from handling organic grains such as flour, metal grinding, chemical spraying and processing, pharmaceuticals and woodworking. If dust is dispersed as a cloud and ignited, based on confinement, the flash fire can result in an explosion. What should be noted is that while materials such as metals are not a fire hazard when in a solid form. When these materials are dust or powder of particles of roughly 500 μm in diameter based on the specific material (31), there is a potential explosion hazard.

While combustible dusts have many different properties compared to flammable gases, the hazards associated can be related. Understanding well known and researched flammable gases and combustible dusts will be used to help rank Li-BESS deflagration hazards. This will be presented in chapter three.

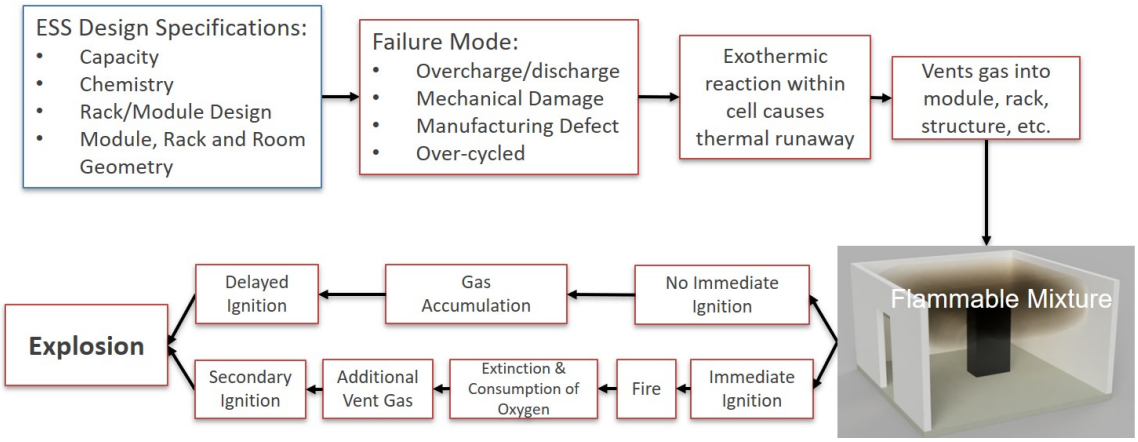

Figure 2.12: Li-BESS Explosion Hazard

Figure 2.12 shows how system design can lead to the generation of a flammable mixture and an eventual explosion in a Li-BESS system. In the event a failure occurs in a Li-BESS, vent gases from failing cells can accumulate at the module, rack or room level. Based on factors such as gas-species, ventilation, concentration, release rates, and total vent gas volume, a flammable mixture can occur. With initial ignition, a fire may occur that consumes surrounding oxygen and can lead to under-ventilated fire extinction. More vent gas is produced from other cells that have failed. Additional ventilation can suddenly happen, for example by firefighters entering the Li-BESS compartment. If secondary or delayed ignition occurs, this can cause an explosion.

2.2.2 Li-BESS Fire Hazards

Li-BESS present a unique fire hazard due to the failure modes and propagation effects. When a lithium-ion cell fails, flammable gases are usually ejected. These gases can remain unburned or might be ignited and burned as a jet-flame. This jet-flame from one

cell in a Li-BESS can heat other cells, converting the potential chemical energy rapidly into thermal energy. With fuel and heat provided by the failed cells, if there is enough oxygen present, a fire hazard will exist. Based on ventilation rates, and whether the Li-BESS is well vented or in a sealed environment, will determine if a fire scenario or explosion scenario will exist. Not only is there the hazard of the flammable gases, but also the various materials used to construct the actual cells add to the fuel load. Cells are constructed using various plastics such as nylon and polypropylene. Additionally, a hazard exists regarding extinguishing strategies. Class C fire extinguishers are used for electrical fires yet using water directly on the cells can help cool down and prevent reignition and slow propagation of failure throughout cells (32). How to treat lithium-ion cells as an overall commodity is still unclear. There is a lack of overall guidance for this unique hazard as a commodity and when used in Li-BESS.

2.3 Relevant Codes & Standards

This section will review some of the relevant codes and standards regarding lithium battery energy storage systems. Some of the standards are mentioned in the Codes 101 document from PNNL/SNL (33). A lot of safety groups are depending on the upcoming NFPA 855 to enforce the safety of Li-BESS. Yet this code has yet to be published, and users will need to be aware of other codes and standards, such as NFPA 13, NFPA 68, NFPA 69, NFPA 70, ASHRAE 21 and appropriate UL standards. The intent of this section is to review the different hazards along with codes and standards associated with mitigating or preventing those hazards while giving some insight on certain gaps or issues that should be addressed.

National Fire Protection Agency Codes and Standards:

- NFPA 1 Fire Code- Ch. 52 Energy Storage Systems (34)
- NFPA 13 Standard for the Installation of Sprinkler Systems (35)
- NFPA 68 Standard on Explosion Protection by Deflagration Venting (36)

- NFPA 69 Standard on Explosion Prevention Systems (37)
- NFPA 70 National Electrical Code (38)
- NFPA 72 National Fire Alarm and Signaling Code (39)
- NFPA 1620 Standard for Pre-Incident Planning (40)
- NFPA 855 Standard for the Installation of Stationary Energy Storage Systems (In-Progress as of Spring 2019) (41)
- NFPA 5000 Building Construction and Safety Code (42)

International Code Council:

- International Fire Code (43)
- International Building Code (44)

Underwriters Lab Standards:

- UL 489 Molded-Case Circuit Breakers, Molded-Case Switches, and Circuit-Breaker Enclosures (45)
- UL 810A Standard for Electrochemical Capacitors (46)
- UL 1642 Standard for Lithium Batteries (47)
- UL 1741 Standard for Inverters, Converters, Controllers and Interconnection System Equipment for Use With Distributed Energy Resources (48)
- UL 1973 Standard for Batteries for Use in Stationary, Vehicle Auxiliary Power and Light Electric Rail (LER) Applications (49)
- UL 9540 Standard for Energy Storage Systems and Equipment (50)
- UL 9540A Test Method for Evaluating Thermal Runaway Fire Propagation in Battery Energy Storage Systems (51)

International Electrical and Electronics Engineers:

- National Electrical Safety Code (52)
- IEEE 1375-2003 Guide for the Protection of Stationary Battery Systems (53)
- IEEE 1547-2018 - IEEE Standard for Interconnection and Interoperability of Distributed Energy Resources with Associated Electric Power Systems Interfaces (54)
- IEEE 1679.1-2017 - IEEE Guide for the Characterization and Evaluation of Lithium-Based Batteries in Stationary Applications (55)
- IEEE 1635-2012/ASHRAE Guideline 21 Guide for the Ventilation and Thermal Management of Batteries for Stationary Applications (56)

Unified Facilities Criteria:

- UFC 3-520-05 Stationary Battery Areas (57)

The various codes and standards are slowly being updated and used for guidance on Li-BESS installations and safety. Different authorities adopt and use different codes or standards. For example, one area of jurisdiction might adopt IFC whereas the other adopted NFPA 1. At this point, using both and meeting the minimum requirements might be the best idea as the various codes are updated on different time intervals. NFPA 1 Fire Code Ch. 52 Energy Storage Systems uses a lot of the verbiage that will be used in the upcoming NFPA 855 Standard for the Installation of Stationary Energy Storage Systems. The most interesting point that should be made is in table 52.3.2.2.1 which mentions Maximum Allowable Quantities (MAQ) of 600 kWh. This is the nominal combined capacity of all systems in space. If the systems in a Control Area exceeds 600 kWh, the area shall meet High Hazard classification requirements per NFPA 101 Life Safety Code. A control area is defined as "*a space bounded by exterior walls, firewalls, fire barriers, horizontal assemblies, roofs or a combination of these*". The term Maximum Allowable Quantity defines the quantity of something allowed in each control area. At different floor levels, the MAQ and number of control areas change. At grade, there are four allowed control areas. Level 2 allows three control areas at 75% of the MAQ, level 3 allows two control areas at 50% of the MAQ, levels 4-6 allow 12.5% of the MAQ at two control areas, with levels 7-9 also having

two control areas at 5% of the MAQ. Above 9 floors, the MAQ is 5% per floor level with one control area. Below grade, the MAQ and number of control areas drop at same as going above grade, but below two floors no control areas or hazardous materials are permitted. Now with a MAQ of 600 kWh in table 52.3.2.2.1 of NFPA 1, the question can be raised as to whether the design and number of control areas apply to table 52.3.2.2.1. With the MAQ mainly slated towards hazardous materials, which are defined as "*A chemical or substance that is classified as a physical hazard material or a health hazard material, whether the chemical or substance is in usable or waste condition*". Whether or not lithium-ion cells are considered hazardous material or not is to be interpreted by the AHJ, but some clarification on how the 600 kWh MAQ should be used. Perhaps this MAQ table should be adjusted to take the type and quantity of electrolyte into account as a hazardous material as discussed by Wang et al. (58). To reduce the classification of the space, Failure Mode and Effect Analysis (FMEA) and another hazard mitigation is required by the AHJ per 52.3.2.4 of NFPA 1.

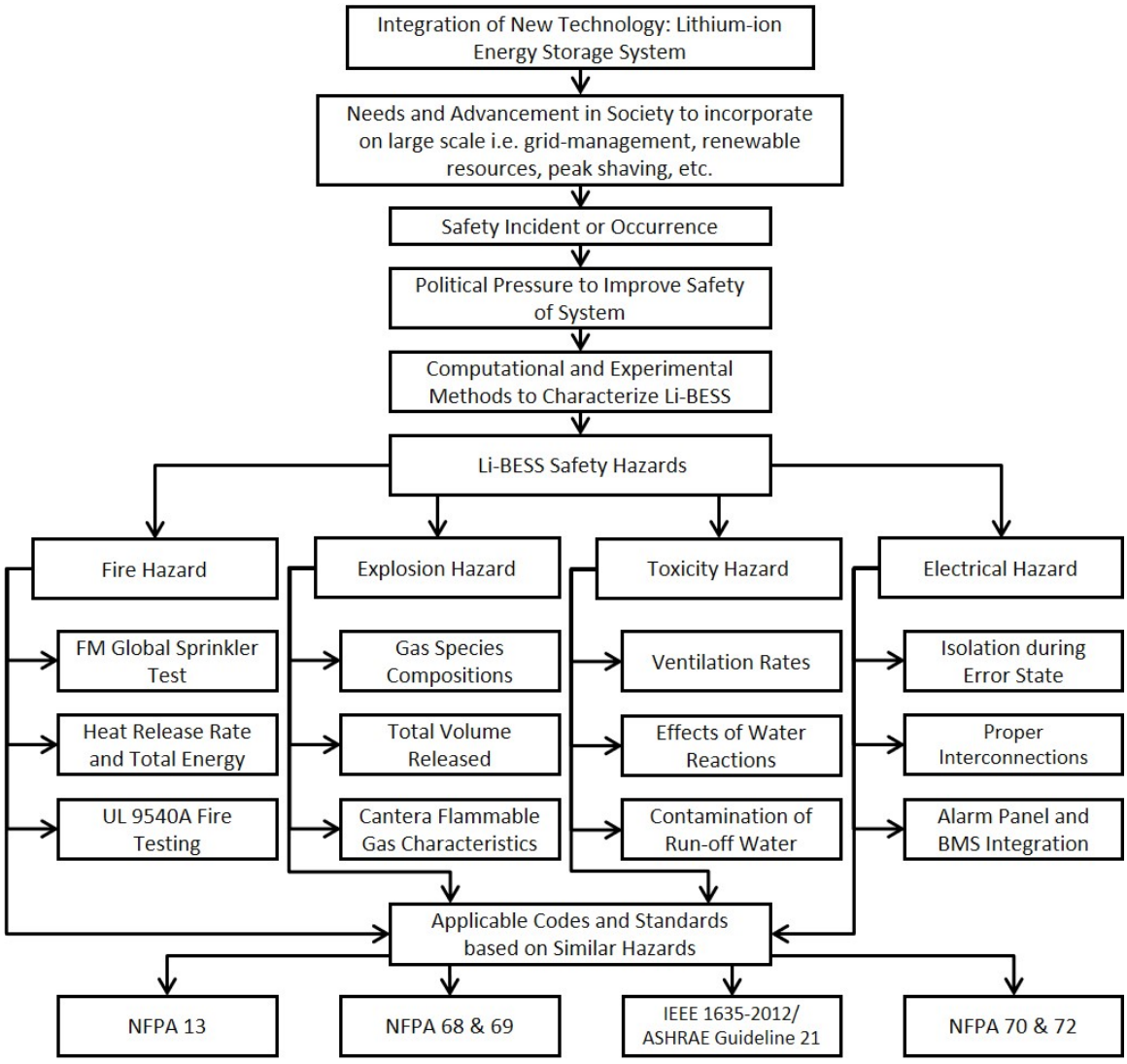

Figure 2.13: Roadmap for Upcoming Technology Safety: Li-BESS

Figure 2.13 shows a visual roadmap of how Li-BESS hazards can be analyzed and what the main hazards and general applicable codes and standards are. The general layout can be applied to other new technologies. As society increases dependence on Li-BESS, incidents occur at various levels. With these incidents, political pressure from the safety community, as well as users/owners, increases to create safe systems. Various computational and experimental methods can be used to further develop and characterize the hazards. The four main hazards identified are fire, explosion, toxicity and electrical safety issues. The main codes identified are NFPA 13, NFPA 68, NFPA 69, IEEE 1635/ASHRAE 21, NFPA

72 and NFPA 70. The focus of this thesis is explosion and fire safety, but a general overview of the electrical and toxicity hazards will be provided in this section.

NFPA 68 Standard on Explosion Protection by Deflagration Venting and NFPA 69 Standard on Explosion Prevention Systems are standards to design and install both active and passive deflagration and explosion safety systems. Industry uses safety standards to control deflagration hazards prescribed in NFPA 68 Standard on Explosion Protection by Deflagration Venting and NFPA 69 Standard on Explosion Prevention Systems. NFPA 68 is used to size deflagration vents. Deflagration vents are a passive pressure relief system that is sized to release the overpressure of a deflagration while keeping the structural integrity of the structure in place. NFPA 69 focuses on active systems such as oxidant reduction, combustible reaction reduction, controlling ignition sources, and isolation methods. Oxidant reduction will reduce the level of oxygen by adding an inert gas to purge the environment so that a fire or explosion cannot occur. Reducing the combustible concentration is done by ensuring the gas concentration of flammable gas is never to reach the lower flammability limit. This is can be done through ventilation or dilution. Detection of gases can be used to shut down specific ignition sources in a space that may trigger an explosion. Passive and active methods to isolate explosions such as active chemical barriers and actuated valves or with diverters and flame arrestors. In some cases, one standard or method compared to the other might be the better choice. Some scenarios may require either a combination of both or performance-based solutions. Yet with Li-BESS it should be noted methods prescribed in NFPA 69 are difficult if not impossible. One example is controlling ignition sources. When lithium-ion cells thermally runaway and fail, they self-heat and this failure can lead to high temperatures. With this elevated temperature, there's a higher probability of ignition occurring and no method to prevent it. Application of NFPA 68 vent sizing will be discussed in chapter three.

NFPA 13 Standard for the Installation of Sprinkler Systems is used for the minimum design and installation of sprinkler systems and NFPA 72 National Fire Alarm and Signaling Code specifies the design, installation, and maintenance of fire alarm systems. It is interesting

neither NFPA 13 or 72 provide specifications for lithium-ion cells. NFPA 13 specifically notes omitting lithium-ion and other cells with combustible electrolytes. NFPA 72 also does not have any specific designs or guidance for smoke or heat detection locations for Li-BESS. Performance-based designs would be required for both fire alarm and sprinkler systems. With lithium-ion cells enclosed inside of modules which are enclosed inside of racks, it is difficult to get water directly on the actual cells.

FM Global has conducted tests to evaluate the bulk storage of lithium-ion cells of different construction types and packaging configurations (59). The testing was with a reduced commodity due to the extensive cost of large quantities of lithium-ion cells and was intended to show the effects of stored lithium-ion cell fires. Since sprinkler and suppression guidance is not provided in NFPA 13, the FM Global testing was intended to give recommendations on how to approach sizing sprinklers with known commodities. This test helped understand and compare lithium-ion cells with other large scale fire hazards. UL 9540A testing also takes into account sprinkler testing only if installation testing is done. Yet the specifications of the sprinkler system are required from the client to perform the test. Chapter four will provide more information on NFPA 13, and how to characterize the fire hazard of lithium-ion cells through bench-scale testing.

IEEE 1635-2012/ASHRAE Guideline 21 Guide for the Ventilation and Thermal Management of Batteries for Stationary Applications is intended to provide information and a guide for designing ventilation and thermal management for BESS. As described in section 2.2.1, both the composition and volume of gases can be dangerous because they are flammable. ASHRAE 21 was last updated in 2012 and does not have guidelines for lithium-ion cells. With further knowledge of the species and volume of the flammable gas mixtures that can be vented from Li-BESS, this standard should be updated accordingly regarding proper ventilation standards. In continuous use or controlled with a gas detection system, NFPA 1 52.3.2.8 requires 1 $ft^3/min/ft^2$ or 5.1 $L/sec/m^2$. But in the event of emergency venting during Li-BESS failure, based on the volume and rate of gas vented and the composition, this may not be enough to prevent the lower flammability limit from being

reached. Chapter three will discuss the LFL and explosion scenarios in more detail.

Additionally, if the water is used to suppress a Li-BESS fire, there is a potential for toxic chemicals from the decomposition of the cells to get into the run-off water. Campion et al. (60) discusses how at elevated temperatures, the electrolyte produces toxic compounds. Campion reported alkyl fluorides and the fluorinated phosphorous compounds, alkyldifluoro- phosphate and dialkylfluorophosphate during the thermal decomposition. Additionally, Hammami et al. (61) reported toxic alkylfluoroethers from the electrolyte and cathode reacting. Ribiere et al. (62) determined the total amount of hydrogen fluoride, carbon dioxide, nitric oxide, sulfur dioxide, and hydrogen chloride. By determining the total amount of toxic gases produced, the time to different toxicity limits was determined as a function of the total battery system capacity. These studies show there is a need to understand the quantity of these toxic compounds and how they can be collected and properly disposed of in the event a suppression system capturing these toxic chemicals.

NFPA 70 National Electrical Code Article 706 gives requirements for energy storage systems. Along with citing numerous IEEE standards that were listed above, it gives guidelines for electrical disconnection methods, circuit sizes, over-current protection, interconnections and installation of ESS. While the electrical disconnects are required to be within sight of the ESS or out of sight if it is capable of being locked open, it could be argued the latter is safer for emergency response. NFPA published a one-page emergency response reference guide for first responders (63). The first step when assessing the scene of a BESS fire is to locate emergency stops and the location of the battery room. Also understanding the type of battery rack and the safety data sheet (SDS) is also suggested. The SDS will specify the occupational health and safety concerns related to exposure to the chemical mixtures associated with lithium-ion cells. The second step is to shut down the equipment if there is a fire or life safety issue. The third step is to monitor for toxic and flammable gas build up along with the BESS with thermal imaging cameras and ventilating as needed. The critical issue with this method comes when the BESS must be deactivated. This means without a remote disconnect, exposure to the system might occur. This is a

safety concern and perhaps a requirement in both NFPA 70 and the evolving NFPA 855 standard specify or require a remote disconnect feature to minimize exposure to toxic and flammable gases.

Figure 2.14: Li-BESS Double V-Diagram

V-Diagrams or V-Models are intended to help visualize the development of a product or system (64). Figure 2.14 shows a double V-Diagram that shows the steps to both design the system and deploy safety testing or modeling at all levels. This helps understand both the system design and safety integration while also what levels need testing and what documentation needs to be completed. The design and construction timeline help visualize the higher-level steps to go from concept to final commissioned product. The scope of work or SOW is defined based on the customer's expectations and requirements. From there, an understanding of what works and what specific systems can be derived from the systems requirement document (SRD). Using the various codes and standards, the system safety requirements can be listed in parallel with the Li-BESS requirements. Bench-scale and other testing or models can be used to validate the safety and performance of the cells, module and rack designs and the safety requirements of each can be verified. In addition, once the system is fully defined and specified, documentation of this can be added to the safety plans. The authority having jurisdiction (AHJ), architect and engineering firm or consultant (A&E) and the fire department inspectors can commission and approve the installation and safety features after installation. Once these steps have been completed, the system can be turned over to the customer. Lessons learned and what unique challenges were addressed can be documented to help improve future safety and streamline the design process in future applications.

UL9540A can be tied into figure 2.14, as it provides testing standards at a cell, module, unit, and installation level. The cell level testing is intended for understanding the characteristics of the cell design and how it fails and goes into thermal runaway. Understanding the species of the cell vent gas and lower flammability limit contributes directly to NFPA 1 Ch. 52 with respect to the gas concentration cannot hit 25% of LFL. Additionally, this contributes directly to understanding if there is an explosion hazard and how to compute laminar flame speeds, theoretical maximum overpressures and implement NFPA 68 to size deflagration vents. The next level of testing is the module design in UL 9540A. This test provides characteristics of a burning module. The heat release rate and observations of the test are recorded. The fire load and fire characteristics provide

necessary data for designing sprinkler and suppression systems especially since NFPA 13 has no lithium-ion cell design information. The unit level test gives a large scope and provides not only the whole unit heat release rate and gas generation data but also the heat flux and target wall temperatures. This data again can provide a means to help further understand the fuel load of a complete system. Additionally, how to separate Li-BESS from other combustibles, what materials and fire ratings that nearby walls and barriers must have can be derived from this test. The full test including fire mitigation helps understand the functionality and effectiveness of the fire and safety mitigation systems. Each level of the UL9540A testing is captured in the V-diagram at the cell, module, rack, and system level. With code requirements and known hazards, a starting point to help understand both qualitatively and quantitatively how to design safety systems for Li-BESS, figure 2.14 helps visualize the process. This can also be used for other technologies and applied as needed for other safety or performance systems.

Chapter 3

Deflagration Analysis

The intent of this chapter is to present and evaluate models that can be used to determine critical inputs for the analysis of fire and explosion hazard consequences. As discussed in section 2.3, Li-BESS presents a potential explosion hazard. This section describes three metrics that are key to understanding the significance of an explosion: lower flammability limit, flame speed, and maximum overpressure. These metrics are key inputs into the analysis of explosion consequences. In thermal runaway, reactions increase cell temperature, build pressure in the cell, and can ultimately lead to off-gassing due to a rupture in the cell. During thermal runaway, battery cells can generate large amounts of flammable gas consisting of hydrogen, carbon monoxide, and carbon dioxide along with various hydrocarbons such as methane and propane. The vent gas composition break down will be provided in the literature review.

The lower flammability limit (LFL) is used to determine the volume fraction at which an explosion and fire hazard exists. The laminar flame speed is the speed at which the flame propagates relative to unburned fuel mixture. This measurement is important for understanding the explosion potential and the vent area needed to mitigate an explosion event. The maximum constant volume adiabatic pressure is used to characterize the worst-case explosion event in which the explosion is completely confined. In addition, the various metrics can be used to help rank and compare with already known deflagration hazards such as combustible dust and flammable gases. By using NFPA 68 to size deflagration vents for different explosion hazards, this can help take into account all of the different metrics and rank the Li-BESS explosion hazard and safety requirements.

3.1 Vent Gas Literature Review

Many experiments have been performed to characterize the vent gas from lithium-ion cells in thermal runaway. These experiments record the compositions for cells with different chemistries at varying states-of-charge (SOC's). The cathode chemistries that have been analyzed are lithium-cobalt oxide (LCO), lithium-manganese-cobalt oxide (NMC), lithium-iron-phosphate (LFP) and lithium-nickel-cobalt-aluminum oxide (NCA). The results of the said review are summarized in table 3.1 below:

Table 3.1: Summary of Cell Vent Gas Literature

Reference	**Type of Cell**	**Cathode Chemistry**	**Electrolyte**	**Initial SOC (%)**	**Failure Environment**	**Failure Test**
Kumai (1999) (65)	18650	LCO	PC:EMC: DEC:DMC	0%	Vacuum	Cycled/Overcharged/ Overdischarged at 25 C
Ohsaki (2005) (66)	Prismatic 633048	LCO	EC:EMC	OCH	N/P	Overcharged at 1 C Rate
Kong (2005) (67)	18650	LCO, LMO, LFP	EC:DEC	OCH	Ambient Conditions	Overcharged
Doughty (2005) (68)	18650	NCA	EC:PC:EMC & EC:EMC	100%	N/P	Thermal-Abuse (ARC)
Abraham (2006) (69)	18650	NCA	EC:EMC	100%	N/P	Thermal-Abuse (ARC)
Roth (2008) (70)	18650	NCA	EC:EMC	100%	Sealed Container	Thermal-Abuse (ARC)
Ribiere (2011) (62)	Pouch Cells	LMO	EC:DEC:DMC	0/50/100%	Air	Thermal-Abuse (Tewarson calorimeter)
Somandepalli (2014) (71)	Pouch Cells	LCO	ED:DEC	50/100/150%	Argon	Thermal Abuse (Combustion chamber)
Golubkov (2014) (72)	18650	LCO/NMC, NMC, LFP	DMC:EMC:EC & DMC:EMC:EC:PC	100%	Argon	Thermal Abuse (Reactor Chamber)
Larsson (2014) (73)	Battery Packs	LFP	N/P	0/50/100%	Air	Thermal Abuse (Fire Test Chamber)
Spinner (2015) (74)	18650	LCO	DMC:EC:PC	N/P	N/P	Thermal Abuse on Overcharged Cells(Fire Test Chamber)
Fu (2015) (75)	18650	LCO	N/P	0/50/65/ 70/100%	Air	Thermal-Abuse (Cone-calorimeter)
Yuan (2015) (76)	Prismatic	LFP	EC:DEC:EM	Varied from 100% to 190%	Air	Overcharged
Golubkov (2015) (77)	18650	NCA, LFP	EC:DMC:EMC:MPC EC:DMC:EMC:PC	Varied from 0% to 143%	Inert Gas	Thermal Abuse
Sun (2016) (78)	18650	LCO, LMO, NMC, LFP	N/P	OCH	Air	Thermal Abuse on Overcharged Cells (Combustion Chamber)
Zheng (2016) (79)	Pouch Cells	LFP	EC:DMC:EMC	0%	N/P	Overdischarged (Glove Box)
FAA Study (2016) (80)	18650	LCO	N/P	0% thru 100%	Nitrogen 10 psia	Thermal-Abuse (Cone-calorimeter)
Lammer (2017) (81)	18650- (32A, 35E, MJ1)	NCA	N/P	100%	Inert Gas	Thermal Abuse
Larsson (2017) (82)	Pouch, Cylindrical	LCO, LFP, NCA-LATP	N/P	100%	Air	Thermal Abuse (Fire Test Chamber)
Fernandes (2018) (83)	Cylindrical, 26650	LFP	DMC:EMC: EC:PC	190%	Air Tight Polypropylene Enclosure	Overcharged (Explosion Proof Room)

The intent of table 3.1 is to show the various cell failures tests, types of cells and electrolyte compositions. While a comparison of the vent gas compositions is by SOC and

cathode chemistry, it is important to understand these parameters. If the authors did not provide the failure environment specifically, it was noted as N/P. For tests that involved open flames or cone calorimetry, it was inferred that failure occurred in the air. If a failure occurs in a non-inert environment, the reported vent gas composition will be slightly different due to some reactions taking place with the surrounding atmosphere. The vent gas composition break-down from the literature review can be viewed in figure 3.1 below.

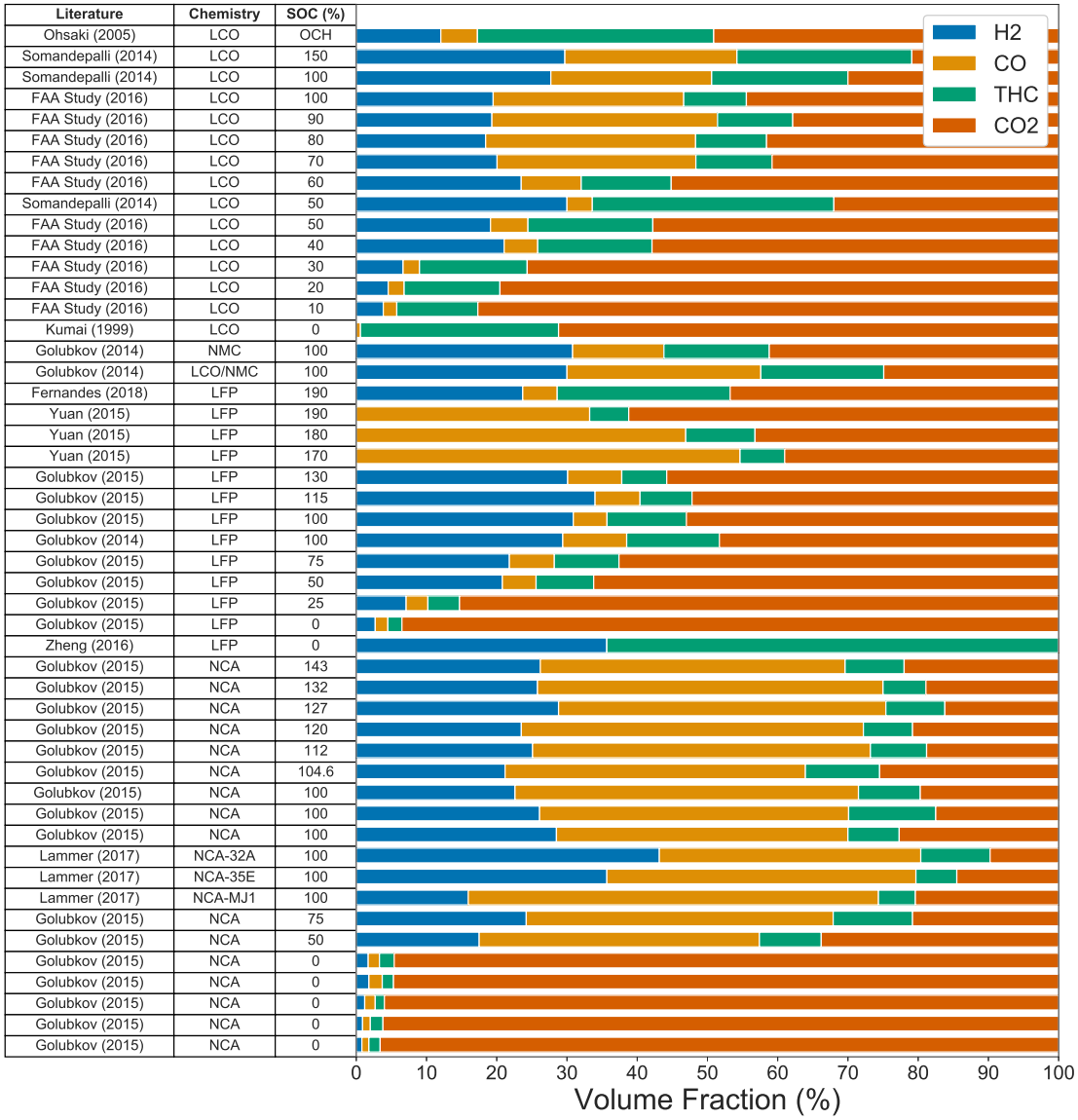

Figure 3.1: Battery Vent Gas Species Compositions from Literature

Figure 3.1 shows all the species composition from the reviewed literature by volume fraction. This review gives only the composition break down and not the total volume released. Many of the failure tests are through thermal abuse using, for example, ARC (Accelerating Rate Calorimetry) testing. In 2014, Somandepalli et al. (71) used a heating wire to cause cells to thermally runaway and vent gas. This was done in a sealed test chamber filled with argon. The vent gas composition of the LCO cells showed that as the SOC increases, the volume fraction of carbon-monoxide increases with the carbon-dioxide and hydrocarbons decreasing. Golubkov et al. (72; 77) performed failure tests similar to Somandepalli in both 2014 and 2015. Golubkov at al. used a variety of cathode chemistries and varied the SOC in both papers. Heaters were used to fail the cells in inert environments. The tests showed for NCA cells that for SOC greater than 75%, the volume fraction of carbon-dioxide decreases significantly; hydrogen takes up about 25% volume and carbon-monoxide takes up a significant fraction of the NCA vent gas volume. When looking at the 2014 study by Golubkov et al., the cathode chemistry varied between LCO/NMC, NMC, and LFP. These three cathode chemistries at 100% SOC showed nearly constant volume fraction of hydrogen, but a decrease in carbon-dioxide when comparing the LCO/NMC and NMC with the LFP chemistry. An FAA study by Maloney et al. (80) was performed in 2016 at 10 psia in an inert environment to characterize the effects of varying SOC on vent gas composition. Using LCO cells, they found that as the SOC increases, the volume fraction of carbon-dioxide decreases. Additionally, Somandepalli measured the lower flammability limit by determining at what concentration value for the maximum pressure could be measured. In 2017, Lammer et al. (81) reported that 18650 cells from different manufacturers with the same cathode chemistry produce different vent gas compositions. They attributed these differences to different manufacturing techniques and environments affecting cell chemistry.

In the reviewed literature, overcharge testing was not as common. The first over-charged test reviewed was in 1999 with Kumai et al. (65), in which an LCO 18650 cell was cycled by over-charging and over-discharging until failure in a vacuum-tight vessel. The main components of the vent gas composition for the over-discharged cell were carbon-

monoxide, and methane. Again in 2005, Ohaski et al. (66) overcharged a prismatic LCO battery at a rate of 1 C until failure occurred and measured the vent gas composition. This was done by collecting the vent gas and analyzing it with gas chromatography. The next over-charged test reviewed was in 2015 by Yuan et al. (76). They overcharged prismatic LFP cells at high states of charge. The vent gas composition is reported to have anywhere from 5% to 18% air, which was normalized out in Figure 3.1 below. The testing by Zheng et al. (79) in 2016 specifies the vent gas composition for an over-discharged LFP pouch cell. These pouch cells were cycled multiple times from nominally 0% to nominally 100% SOC and the capacity loss was measured along with observations of physical degradation of the pouch cells. The final over-charged testing that was reviewed was in 2018 by Fernandes et al. (83). This overcharge test was performed on cylindrical LFP cells at 190% SOC and the vent gas composition consisted of carbon-dioxide, hydrogen, and hydrocarbons. Looking at each composition break-down in Figure 3.1, a noticeable difference is the fact that Kumai showed that LCO cells at a SOC of 0% have a very high amount of carbon dioxide compared to other overcharge tests. Yet Zheng showed a large amount of hydrogen and hydrocarbons with a test on an LFP cell. The data from Yuan and Kumai were not used in the models in section 3.0 because there was no hydrogen reported. For the Fernandes test having the same cathode chemistry and SOC as Yuan, hydrogen accounted for about 25% of the volume of the vent gas composition. Fernandes also brought up this variation when reviewing Yuan's work. Kumai specifically states that hydrogen was not measured or reported yet in other similar electrolyte systems it is.

The overall trends from the literature review of the vent gas compositions can be seen in Figure 4.1. For each cell chemistry, the general trend is that as the SOC increases, the amount of hydrogen, carbon monoxide and hydrocarbon fraction increases as the amount of carbon-dioxide production decreases. The LCO cells have about 25% to 30% carbon-dioxide by volume at 100% SOC while the LFP cells have about 30% to 40% at 100% SOC. The NCA cells have the least amount of carbon dioxide, at about 10% to 25% and upwards of 40% hydrogen by volume.

While the species composition is used to characterize the vent-gas from lithium-ion cells, the total volume of vent gas is also important to understand. The UTFRG Battery Group has performed experiments to determine how the total vent gas volume is affected by the total energy storage capacity. These values were compared with data from the FAA Report (80) and Somandepalli et al. (71):

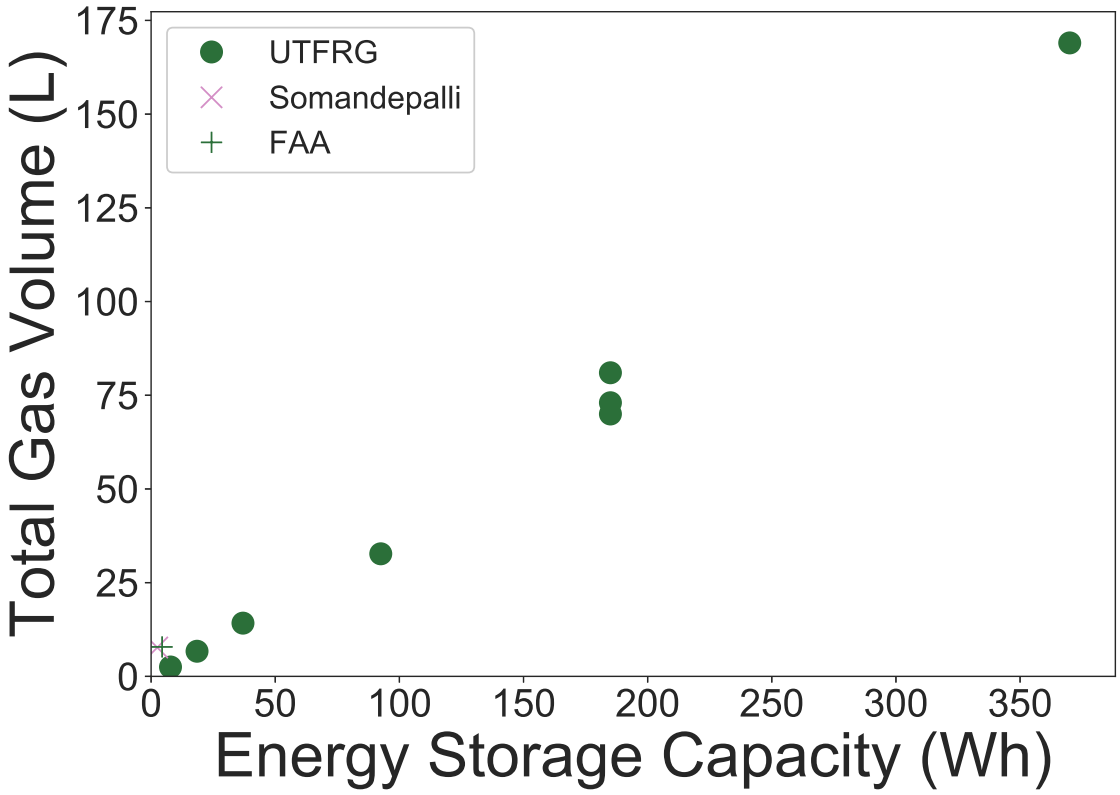

Figure 3.2: Volume Production vs. Capacity

Figure 3.2 shows how the total gas volume scales with the total energy capacity in Wh. The overall trend is linear and gives a value of about 0.46 L/Wh. The largest array size tested is 370 Wh. An array of five 10 Ah cells and two sets of arrays with ten 5 Ah cells were tested, giving similar volume releases. This volume production result is a starting point to help understand the gas production from failed lithium-ion cells. Since a lot of reported volumes are for single cells, using array testing further contributes to a real-world application to help understand what the explosion hazard might be during a failure.

3.2 Gas Mixture Models

The following subsections will give a detailed understanding of the models used to provide an understanding of the different hazards of the various battery cell chemistries and states of charge and how the results vary based on failure tests. Cantera was used as the tool to compute the lower flammability limit, laminar flame speeds, adiabatic temperatures, and maximum overpressure. With these metrics computed, decisions and designs of safety systems for explosion protection can be established for Li-BESS.

Cantera is an open source chemical kinetics program that runs through Python, MATLAB, Fortran or C++ (84). The program has a one-dimensional flame function that allows freely-propagating premixed laminar flames to be analyzed. Other similar functions include burner-stabilized flames and counterflow diffusion flames. Each model is steady-state and quasi-1D. A multitude of inputs is utilized with conservation equations such as energy and species balancing equations. Other programs such as Chemkin by Ansys were considered, but Cantera was selected as its open source nature enables broader use. To start using Cantera, the volume fractions of each species in the fuel and air compositions are defined. The mixture of fuel and air can be adjusted by altering the equivalence ratio. Transport data and molecular properties for gas species used in Cantera comes from GRI-Mech.

GRI-Mech was a sponsored study by the Gas Research Institute (GRI) through computations and experiments at the University of California at Berkley, Stanford University, the University of Texas at Austin and SRI International. Using GRI-Mech, accurate chemical reactions can be modeled for natural gas flames (85). Some of the different parameters in GRI-Mech include elementary chemical reaction rates, transport coefficients, molar heat capacity, entropy, and standard enthalpy. The data are open-source but are about twenty years old and are no longer updated and supported. Due to the nature of the program and the overall goal, many of the species from the hydrocarbons measured by researchers in the literature review for the battery vent gas composition measured were not included in GRI-Mech. Taking this into account, many of the species were binned and

the volume fraction of those species was added to propane. The binned species consist of hydrocarbons, C_xH_y, with a value for x of three or greater. With the larger molecular mass, propane is the most similar species to the ones not in Cantera. With most of the vent gas compositions obtained from available literature having less than 10% of the gas by volume being binned into propane, it did not have a large effect on the overall flame speed. A sensitivity study was performed by binning the volume fraction into propane compared to methane and the results are further discussed in section 3.2.3.

3.2.1 Lower Flammability Limit

The first metric to establish is estimating the range of lower flammability limits (LFL) for different cathode chemistries. The LFL is important for fire and explosion analysis because it defines the volume fraction of fuel required to create the potential for a fire or explosion. Different codes, standards, and practices have specific requirements regarding LFL. This is the main motivation behind understanding and investigating LFL further. One example is NFPA 1 Ch. 52 states that ventilation is required to keep the flammable gas concentration limited to 25% of LFL otherwise a ventilation rate of 1 CFM/ft^2 (5.1 L/sec/m^2) must be maintained or activated with gas detection.

Different methods to estimate the LFL for the battery vent gas compositions has been performed in literature. Somandepalli et al. (71) determined LFL experimentally using a combustion vessel and noting the fuel concentration at which the maximum overpressure was greater than atmospheric pressure. The FAA study (80) used Le Chatelier's mixing rule (86) given in equation 3.1, which gives the lower flammability limit of the mixture based on the different volume or mole fractions for fuel.

$$\frac{1}{X_{\mathrm{L}}} = \sum_{i=1}^{fuels} \frac{X_{\mathrm{i}}}{X_{\mathrm{L_i}}} \tag{3.1}$$

Using Le Chatelier's Law to compute the LFL of each cathode chemistry at 100% SOC gives various ranges based on the cathode chemistry: LCO ranging from 6.5% to 7.5%, the LFP ranging from 8.3% to 8.7% and NCA cells ranging from 6.2% to 9.8%. The NCA

cells have such a larger range for LFL due to the various sets of data at 100% SOC with different failure tests.

Le Chatelier's law is mainly intended for only hydrocarbons and may not be appropriate for battery vent gas. This is due to the large amount of hydrogen and carbon-monoxide as well as inert diluent carbon-dioxide. Another method to determine LFL for an air-fuel-diluent mixture is to calculate the critical adiabatic flame temperature (CAFT). This method is appropriate for mixtures which contain inert diluents such as carbon-dioxide (87) as seen in equation 3.2.

$$X_{\mathrm{L}}(T_{\mathrm{u}}) = \frac{\tilde{c}_{\mathrm{p,u}}(1573K - T_{\mathrm{u}})}{\triangle h_{\mathrm{c}}} \tag{3.2}$$

This method has an error when applied to the battery vent gas due to hydrogen having an adiabatic flame temperature at LFL a lot lower than 1573. The study by Zlochower et al. (88) shows the theoretical adiabatic flame temperature for hydrocarbons such as ethylene and methane range from 1390 to 1484 K at LFL. Hydrogen has a theoretical adiabatic flame temperature of approximately 734 K at LFL from Le et al. (89). Other methods such as Beyler's Method and the method described by Ma et al. (90) also have a limitation in predicting LFL for gas mixtures involving hydrogen, hydrocarbons, and diluents.

The EPA has a paper prepared by the U.S. EPA OAQPS regarding designing and operating flares (91) that is currently in peer-review. The intent of this paper is to help understand the performance of flares used in various industrial applications. Table G.5 in the paper provides experimentally measured LFL values for mixtures of hydrogen, methane, nitrogen, and carbon-dioxide compared to computed results. Jones et al. (92) use tables of flammability limits for carbon-monoxide, methane, and hydrogen in carbon-dioxide to develop a method to determine the mixture LFL with Le Chatelier's method. These tables were developed through multiple tests by pulling measured gas volume into an explosion tube. From there gas mixture was set to atmospheric pressure and as the tube was opened,

the mixture was exposed to a flame. By adjusting the volume of the gas mixture to the amount of air in the tube, the flammability limits were determined. From there, the tables were developed and used to determine the LFL of various flammable gas and diluent mixtures.

The first step for applying this method is to split inert gas into different binned groups and combining a specified quantity with each individual combustible gas species. The developed tables by Jones give the LFL of each new gas mixture based on the ratio of combustible to inert gas. For example, if there was a mixture with 50% carbon-dioxide, 30% hydrogen and 20% methane, carbon-dioxide can be split in half and each half combined with the hydrogen and methane. This would give flammable gas to inert gas ratios of 1.2 for the hydrogen and carbon-dioxide mix and 0.8 for the methane and carbon-dioxide mix. The LFL for these flammable gas to inert gas ratios can be looked up in tables provided by Jones. The next step is to input those values into Le Chatelier's equation 3.1, to determine the LFL. The LFL for the binned mixtures is 9.0% for the hydrogen and carbon-dioxide mix at 55% volume percent and 10.0% for the methane and carbon-dioxide mix at 45% volume percent. This gives a mixture of LFL of 9.4% when using 3.1. How the diluent is split according to Jones does make a difference. Using the example with 50% carbon-dioxide, 30% hydrogen and 20% methane, the percent volume of carbon-dioxide can be split and binned to equal 30% and 20%. Combining the 30% volume percent with hydrogen and 20% volume percent with methane gives and LFL of 9.8%. This is 0.4% higher than the previous binning method.

To use the method by Jones for the lithium-ion cells, it should be noted that the hydrocarbons will be binned into methane. The tables used by Jones do not include other hydrocarbons. While there is some uncertainty in using this method since splitting of the diluent to combine with the combustible gas can be varied, it is used to rank or understand how flammability limit varies for each cathode chemistry. With most codes and standards requiring the space to not allow the gas concentration to reach 25% of LFL, this safety factor will help mitigate uncertainties. The paper flare paper by the EPA shows a less than 10%

error compared with experimental results. It is also shown that as the hydrogen amount is lower compared to the total combustibles, roughly 33% or less, the predicted LFL is higher than the actual LFL. This is due to the enhancement in combustion from hydrogen. Most of the vent gas compositions at 100% SOC have a combustible gas composition of 35% to 50% hydrogen.

The study by Bounaceur et al. (93) in 2017 furthers the understanding of approaches on predicting the lower flammability limit for gas mixtures with inert gases. Through this study, a step-by-step method is provided by using a modified version of the CAFT method. The adiabatic flame temperature in this study was computed using Chemkin II which is a similar program to Cantera. According to Bounaceur, hydrogen has an adiabatic temperature criterion of 629 K compared to 1417 K to 1706 K for carbon dioxide and multiple hydrocarbons. The study shows a summation of the adiabatic temperatures, calling this T_{blend} as a simple linear approximation in addition to the CAFT method.

$$T_{\mathrm{L,blend}} = \sum_{i=1}^{fuels} \alpha_{\mathrm{i}} T_{\mathrm{L,i}} \tag{3.3}$$

Where 3.3 is the summation of the adiabatic flame temperatures, $T_{L,blend}$, scaled by the mole fraction of fuel, α_i. According to Bounaceur, the method has an uncertainty of about 15 K. By estimating the blended adiabatic temperature in addition to using the CAFT method, an additional method to estimating the LFL of inert, hydrogen, carbon monoxide and hydrocarbons have been established.

Additional work from studies such as the thesis by Terpstra et al. (94) in 2012 or the dissertation by Hai Le et al. (89) in 2013 show that even with research nearly 100 years ago there is still a gap in the overall understanding of lower flammability limit estimations. With the safety community relying on models to predict behaviors such as laminar flame speed, adiabatic flame temperature and maximum-overpressure, models for estimating the lower flammability limit should be further studied to reduce reliance on testing.

Table 3.2: EPA Gas Mixtures

	Mixture 1	Mixture 2	Mixture 3
Carbon Dioxide	60.6	68.4	69.8
Methane	29.0	21.1	15.1
Hydrogen	10.4	10.5	15.1

The three different mixtures used in this comparison are referred to in the EPA Flares report in table G.5 (91) are provided in table 3.2 above.

Table 3.3: Comparing LFL Calculation Methods with EPA Table

Mixture 1	Tabulated Value	% Error	Mixture 2	Tabulated Value	% Error	Mixture 3	Tabulated Value	% Error
Experimental	13.2	-	**Experimental**	15.9	-	**Experimental**	16.4	-
Le Chatelier's	11.9	10.9	**Le Chatelier's**	14.6	9.1	**Le Chatelier's**	14.7	11.6
CAFT	17.9	26.3	**CAFT**	24.3	34.4	**CAFT**	29.4	44.2
Jones	12.7	3.9	**Jones**	15.9	0.2	**Jones**	16.1	1.9
Bounaceur's	12.6	4.8	**Bounaceur's**	15.7	1.5	**Bounaceur's**	16	2.6

Table 3.3 compares the various methods described to calculate the lower flammability limit in percent volume comparing the various gas mixtures from table 3.2. It is clear by using the method provided by Jones to use a modified gas mixture prior to inputting the LFL values into equation 3.1 based takes into account the diluents. This shows with a very small percent error between the experimental data. The method by Jones has an error of less than 5% while Le Chatelier's is much higher near 10%. One issue with the method by Jones is the fact that the binned compositions are up to the user. In this case, the diluent was binned equally with each flammable gas. How the user completes this binning will influence the outcome and uncertainty. Yet this method shows results that are very close to experimental data, as seen in the EPA flare paper and table 3.3 above. Also, the method by Jones is simple compared with some other methodologies and can be performed with spreadsheets.

As discussed previously, using the constant adiabatic flame temperature method has a high error due to hydrogen having a lower flame temperature compared to hydrocarbons. This is validated, as the error using the CAFT method is 26% to 44%. The method by Bounaceur using the adiabatic mixing of the fuels gives results very similar to Jones. The error with this method is just slightly higher than Jones and compared to the CAFT method

it takes into account the hydrogen issues by scaling the adiabatic flame temperature. Both Jones and Bounaceur use modified versions of the known LFL computations in order to account for inert diluents and mixing hydrogen with hydrocarbons and carbon-dioxide.

The methods reviewed show two well-known methods to estimate lower flammability limit: Le Chatelier's Law and CAFT. While both methods have low uncertainty in specific applications, the battery vent gas includes hydrocarbons, hydrogen, carbon monoxide, and inert diluents. Modified versions of these methods were used to validate with experimental data to determine if they are appropriate for lithium-ion cell vent gas. Based on the lower error from experimental to computed, this validates by Jones and Bounaceur as potential methods to compute LFL for battery vent gas compositions.

3.2.2 Battery Vent Gas LFL

The LFL and adiabatic temperature criteria values for the battery species comes from various literature sources such as the studies by Bounaceur et al. (93) and Vidal et al. (95). The LFL values for each individual species is are used for predicting the vent gas composition lower flammability limits with Le Chatelier's Principle.

Table 3.4: LFL and Adiabatic Criteria for Vent Gas

	CO	**H2**	**CH4**	**C2H4**	**C2H6**	**C3H8**
T_{ad} Criteria (K)	1417	629	1480	1369	1602	1509
LFL (%Volume)	12.5	4	5	2.7	3	2.1

Table 3.4 gives the adiabatic temperature criteria used in the method by Bounaceur et al. When comparing the LFL values obtained using the method by Jones with experimental data from Somandepalli et al., there are differences in the results. When comparing with Somandepalli, the LFL reported was 6.3% for the 100% SOC test. Yet the computed values show 8.1%. The method by Bounaceur gives a value of 8.5%. Computations for LFL using the species composition from the study by Somandepalli et al. at 100% SOC are shown in the table below:

Table 3.5: Comparing LFL Calculation Methods with Experimental Data

Somandepalli (2014) LCO	Tabulated Value	%Error
Experimental	6.3	-
Le Chatelier's	6.5	3.08
CAFT	10.3	38.83
Jones	8.1	22.22
Bounaceur's	5.8	-8.62

Table 3.5 compares the experimental data from Somandepalli with the four different methods to calculate LFL in this section. Since the method by Jones only provides tables for methane and the battery vent gas composition includes multiple hydrocarbons, this will cause uncertainty. For the other methods, any species not in Cantera are binned with propane. Since the LFL for methane is approximately 5% whereas propane has an LFL of roughly 2%, this could account for the difference in the calculated value to be higher than that of the experiment by Somandepalli. When comparing with Bounaceur's method, the results are a lot lower compared with the experimental data. The reason behind this could be the larger amount of hydrogen and carbon-monoxide compared to the other species in the vent gas composition. For the fuel composition measured from the LCO cell at 100% SOC, hydrogen is 45.7% and carbon-monoxide is 37.8% of the fuel by volume. This causes the overall mixed temperature to be 1066 K. When using the CAFT method, the prediction was a lot higher due to the high adiabatic temperature assumed. The limitation of Bounaceur's method might come when the species composition has a large fraction of hydrogen. In this case, Le Chatelier's method actually has the lowest error between the different methods. As shown in the dissertation by Zhao (96), based on the fuel species and the diluent volume fraction, the percent error can be low. The trends show with methane and propane blends, as the number of diluent increases, so does the percent error from the experimental value. In table 3.3, with a diluent of about 60% to 70%, the error using Le Chatelier's method has a larger percent error compared to Jone's and Bounaceur's method has a much smaller error.

Table 3.6: LFL Predictions for Battery Vent Gas

	Le Chatelier's	CAFT	Jone's	Bounaceur's
LCO	6.5 to 7.5	10.3 to 13.6	8.1 to 8.8	5.8 to 8.5
LFP	8.3 to 8.7	18.2 to 20.6	9.4 to 10.0	8.6 to 8.7
NCA	6.2 to 9.8	13.7 to 16.7	6.7 to 10.9	7.6 to 11.8

Looking at table 3.6, the predictions for LFL of the battery vent gas have a large range of results based on the method used. Each method has its own set of uncertainties and constraints on how it can be applied. Clearly, the CAFT method is going to have the largest error and should not be used for hydrocarbon, hydrogen, carbon-monoxide and inert diluent mixtures. The estimated LFL is much higher than any of the other methods, as mentioned due to the hydrogen effect and adiabatic flame criteria being so much lower. By modifying the CAFT method with a mixed adiabatic temperature, Bounaceur's method is a lot more reasonable and has about the same error as Jone's method when compared with experimental data in table 3.3. Le Chatelier's method works and is well known but based on the mixture the other provided methods could have a lower uncertainty.

3.2.3 Laminar Flame Speed Analysis

Once a flammable mixture has been created, an ignition source can cause the mixture to ignite. In the event a cell is in thermal runaway, this can raise the local temperature and cause piloted ignition. This will generate a flame front that will propagate through the unburned gas mixture at a speed known as the laminar flame speed (S_L). This flame speed generally increases with increasing temperature and decreases with increasing pressure. The laminar flame speed can be estimated for some hydrocarbons as follows (97) :

$$S_L \cong \frac{1}{p^n} * T^m \tag{3.4}$$

Where T and p are the temperature and pressure of the unburned gas. This flame speed is an essential input for calculating explosion pressures and vent requirements needed to design safety systems.

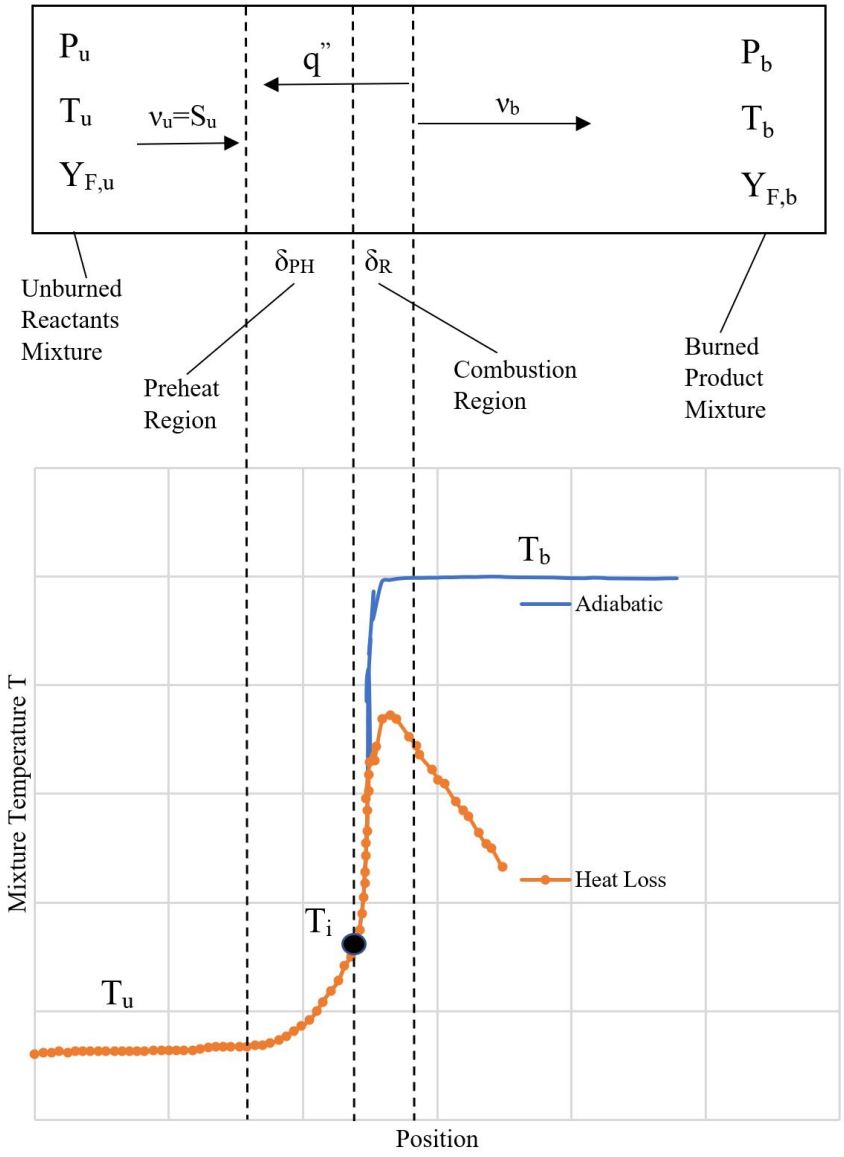

Figure 3.3: Laminar Flame Structure Diagram

Figure 3.3 (87) gives an overview of the actual laminar flame construction. As the fuel and oxidizers approach the flame front, their temperature increases due to an increase in conduction and radiation heat transfer from the flame front. As the temperature increases, there is a chemical reaction as the temperature becomes locally high enough to ignite the reactant. The reaction regime continues to propagate as a flame front, as reactions chain together and continue to engulf the reactants. This is due to the excess energy from

combustion raising the temperature, helping spread the flame front. Propagation speeds below the speed of sound are known as deflagration and speeds above the speed of sound are known as detonation. The speed of sound is c = 343 m/s in dry air at 20 °C. Anything above would become a detonation. There is a deflagration to detonation transition (DDT) where turbulent conditions can cause a deflagration flame propagation to accelerate into a detonation wave. This detonation wave must develop in front of the flame front due to conservation laws, which cause a shockwave in front of the flame to form. Additionally, turbulent conditions can come from obstacles the wavefront has to accelerate around and other disturbances (87). Deflagration speeds vary from less than 1 m/s up to 3 m/s whereas detonation speeds are anywhere from 1.5 to 2.8 km/s (98) and cause a pressure rise.

The equivalence ratio is defined as the mass ratio of fuel to air compared to the stoichiometric mass ratio of fuel to air. When it equals one, this means there is no excess fuel or air, giving a balanced reaction. As the equivalence ratio goes above one, this means there is excess fuel or a rich mixture. As the equivalence ratio goes below one, this is considered a lean mixture as there is left over oxygen on the product side of the reaction. The laminar flame speed is at a maximum near the stoichiometric conditions for hydrocarbons, usually with an equivalence ratio just over one (97). Cantera can automatically balance the fuel and oxidizer mixture through the range of equivalence ratios. The equivalence ratio is defined as follows :

$$\Phi = \frac{(\frac{\text{Mass of Available Fuel}}{\text{Mass of Available Air}})}{\text{Stoichiometric-Fuel-to-Air-Ratio}} \tag{3.5}$$

Hydrocarbon Laminar Flame Speed Comparison

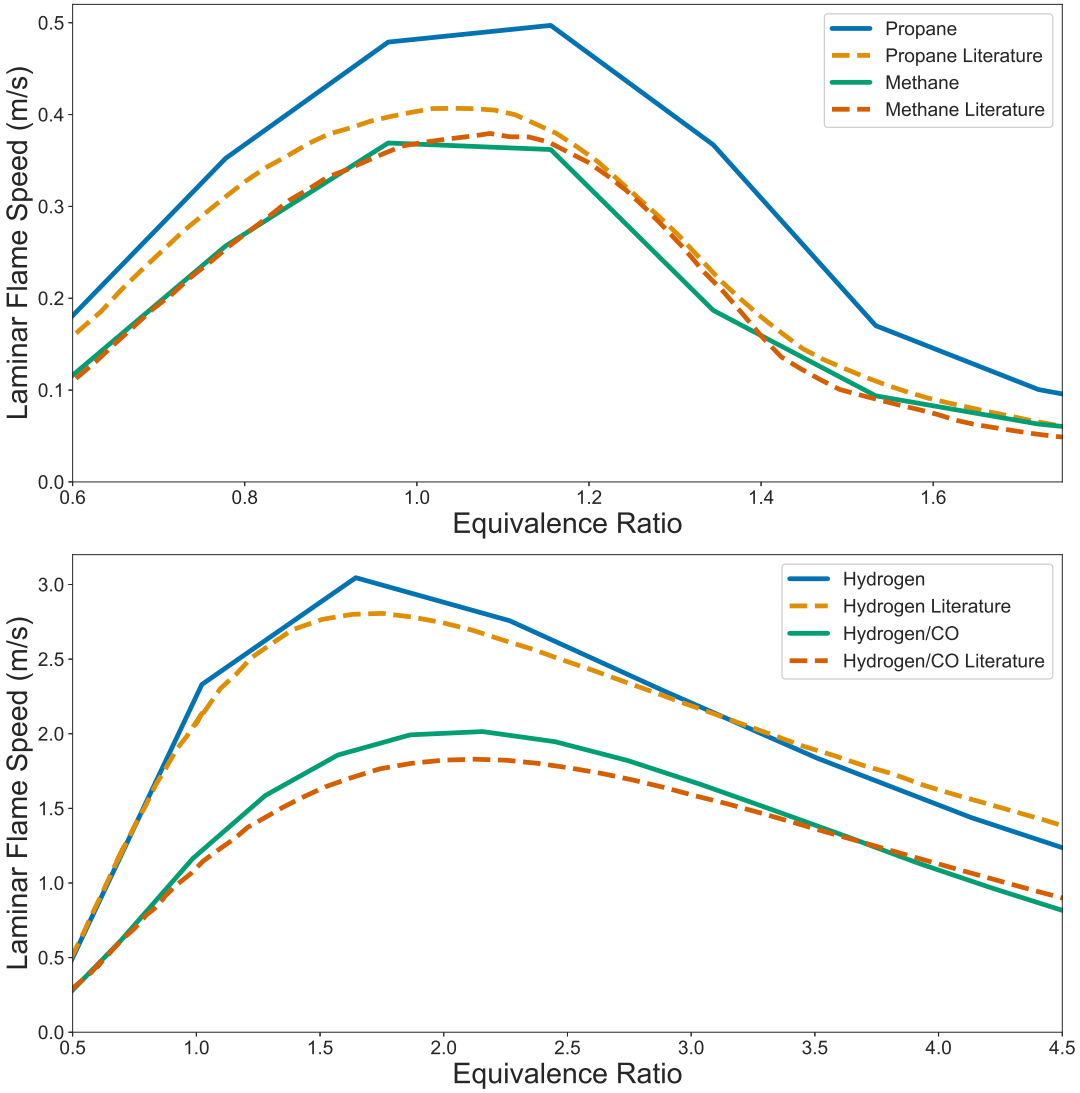

Figure 3.4: Cantera Model Verification with Literature

The results from figure 3.4 show the computed laminar flame speeds for propane and methane from Cantera compared with literature values (99) along with hydrogen and a hydrogen/carbon-monoxide mixture from Cantera compared with literature values (99; 100). The temperature and pressure were set at 300 Kelvin and one atmosphere.

Table 3.7: Maximum Flame Speed Comparison

Max Flame Speed (cm/s)	Propane	Methane	Hydrogen	Hydrogen/CO
Literature	0.41	0.38	2.81	1.83
Computed	0.50	0.37	3.05	2.01
Percent Difference (%)	22.21	2.73	8.53	10.12

Comparing the computed values for methane compared to the literature values, there is almost no deviation in the two. Only once the equivalence ratio is above 1.20 do the flame speeds vary slightly, but the difference is small. When comparing propane in the same fashion, there is a more obvious deviation between the two. Figure 3.4 shows that the laminar flame speed for propane is slightly higher than the literature values by about 6-10 cm/s. Yet when looking at the overall compositions of the battery vent gas from 3.1, with the hydrocarbons only taking up about 15% to 25% of the composition by volume and propane only taking up a fraction of that volume, this was not a large concern with the model. Also, when comparing with other literature that used Cantera such as Johnsplass et al. (101), the propane flame speed compared with the study are very similar in terms of peak flame speeds, showing there is something in Cantera causing the deviation. Similarly, the hydrogen and carbon-monoxide mixture model is slightly higher than the literature, but again only by about 25 cm/s at the peak. The peak flame speeds are well above the 250 cm/s. It should be noted that hydrogen has a much higher flame speed than propane and methane, which will be discussed when comparing different battery vent gas compositions. Overall, all the literature reviews show close comparisons with the models from Cantera. The only species with a large deviation is propane. Between propane not being the dominant species in the battery gas mixtures and the sensitivity study not showing drastic changes when the volume percentage of propane changes, it was not considered a major concern.

When comparing the literature for different flame speeds of higher order hydrocarbons (102; 103; 99) , it can be noted that n-butane, n-pentane, and toluene have extremely similar laminar flame speed profiles when compared to propane. It appears that each of the different higher-level hydrocarbons has similar properties. Also, many of the higher order hydrocarbon species in the original compositions are of a small percentage by volume. This

gives a basis behind 'binning' the original species not included in GRI-Mech into propane. To ensure that this assumption was valid, a sensitivity study was performed by varying the binned species across from 100% propane to 100% methane and a 50/50 mixture by volume.

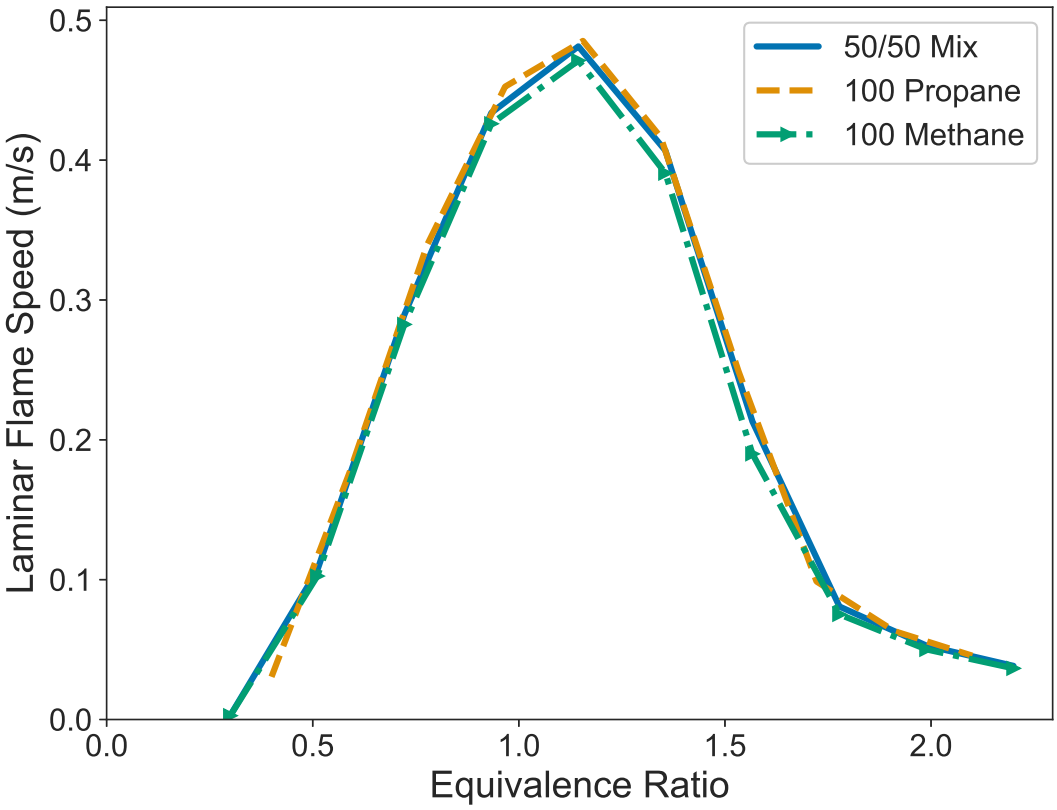

Figure 3.5: Propane and Methane Sensitivity Review

Figure 3.5 compares the flame speed of one battery gas composition by binning the hydrocarbons not available in Cantera into either methane, propane or split between both. Comparing the maximum flame speed of using methane as the binned gas verse propane gives a difference of 1.5 cm/s at the peak flame speed. This difference is small when the peak is almost 50 cm/s for each binned groups.

3.2.4 Maximum Pressure

The final explosion characteristic discussed is the maximum constant volume adiabatic overpressure. This is the pressure that is generated when the gas is combusted in a perfectly adiabatic, constant volume process. This pressure is dependent on the temperature, species composition of the burned gas and how the flame propagates. The maximum overpressure is computed as the theoretical pressure the gas could possibly generate and is an important input into explosion consequences. Cantera was used to calculate this pressure, which is known as the maximum pressure or P_{max}. The values for P_{max} vary depending on the chemical energy contained in the mixture as well as the energy required to heat the products after combustion.

$$\frac{P_{\max}}{P_0} = \frac{n_b T_b}{n_0 T_0} \tag{3.6}$$

Equation 3.6 gives the relationship between the initial pressure and pressure after non-vented deflagration based on the number of moles of reactants, the number of moles after burning occurs and initial and burned gas temperatures. The constant volume adiabatic reaction used for determining P_{max} is a thermochemical problem (31).

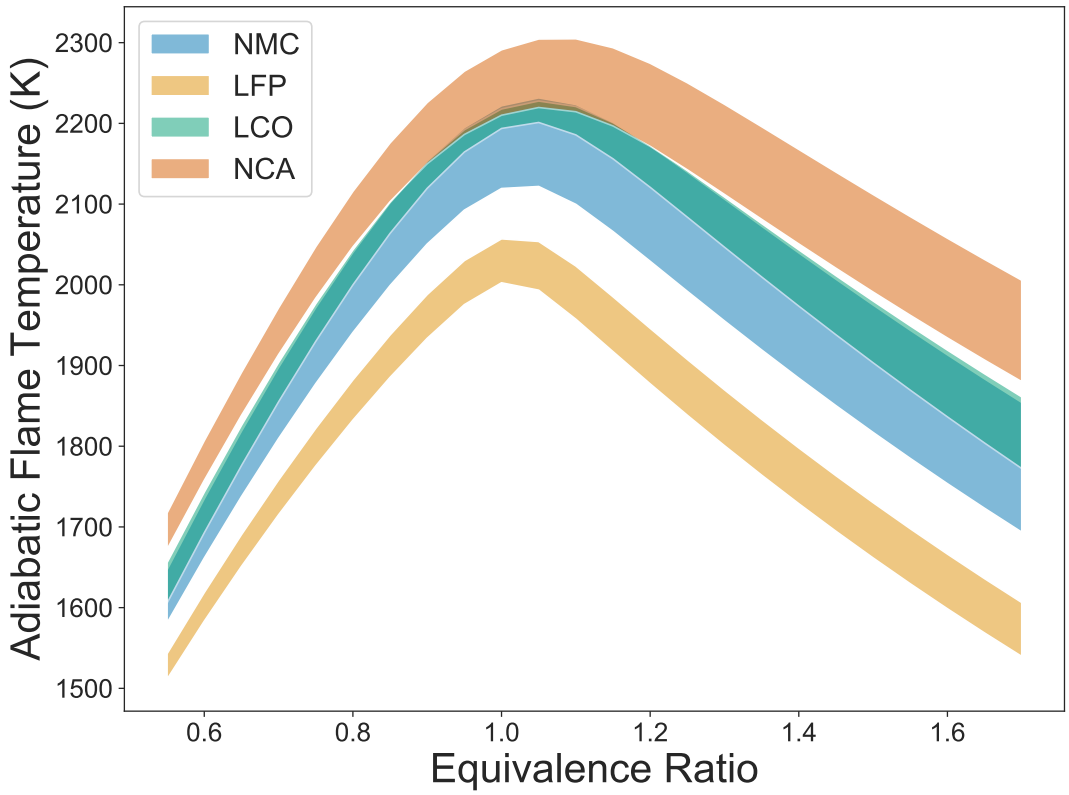

Figure 3.6: Adiabatic Flame Temperature by Cathode Chemistry at 100% SOC

Figure 3.6 shows the different bands give the minimum to maximum theoretical maximum adiabatic flame temperature, T_{ad}, the range for each cathode chemistry vent gas composition at 100% SOC. Using the equilibrium solver in Cantera with the various vent gas species gives the adiabatic flame temperature. As shown in equation 3.6, P_{max} is dependent on this flame temperature, as well as the total number of moles before and after deflagration. The maximum T_{ad} comes at an equivalence ratio between 1.1 to 1.2, with the NCA, LCO, and LFP chemistries having a much higher temperature compared to the LFP chemistry.

3.3 Results of Models using Battery Vent Gas

The first set of results to discuss is for laminar flame speed. To help validate the model even further, comparisons to a similar study by Johnsplass et al. (101) who used

the data from the 2014 paper by Golubkov et al. (72) to model the laminar flame speeds. The paper by Johnsplass used the species compositions from Golubkov to determine the laminar flame speeds as a function of the equivalence ratio using Cantera. The three flame speed plots that Johnsplass presented were compared to help further validate the model. The battery vent gas compositions were for LFP, LCO and NMC chemistries, in which the flame speed plots compared to Johnplass were observed to be very similar and have very close overall peak flame speed. This assured that the model aligns with other studies and could be used to predict the flame speeds for other vent gas compositions.

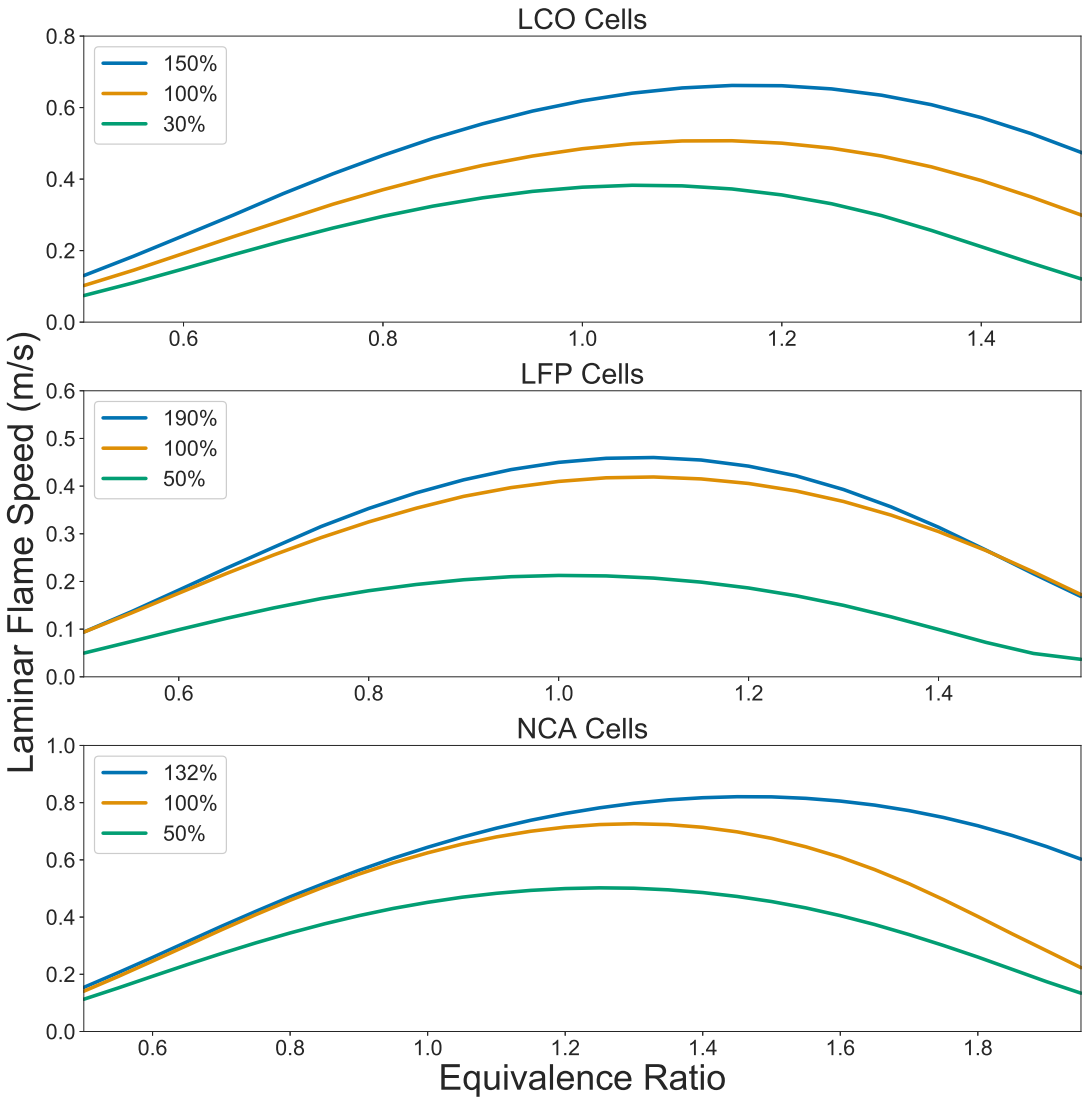

Figure 3.7: Laminar Flame Speed Plots by Cathode Chemistry

Figure 3.7 gives the laminar flame speeds at varying states of charge organized by the failed cells cathode chemistry. Not all results were given, rather a range of flame speeds with increasing SOC. The results show that as the state of charge in the cell increases, the overall laminar flame speed increases. There are some interesting observations to note. The LCO cells have a peak flame speed of anywhere from 0.4 to 0.6 m/s as the SOC increases. The peak values are at an equivalence ratio of roughly 1.1. The LFP cells have a lower overall flame speed, with a peak between 0.4 and 0.5 ms/. The literature gives higher

overall SOC tests when compared to the LCO cells in which there are only two sets of data with a cell over 100% SOC. By referring to Table 3.1, the volume fraction of carbon-dioxide in the vent gas composition begins to increase with the SOC for LFP cells. This is possibly why at higher SOC the flame speeds are not increasing to the range of the other cells. Lastly, the NCA cells have the highest overall flame speed between 0.6 to 0.8 for the peaks at an equivalence ratio of 1.2 to 1.4. This can directly be linked to an increased amount of hydrogen and much less carbon dioxide in the vent gas compositions for the NCA cells.

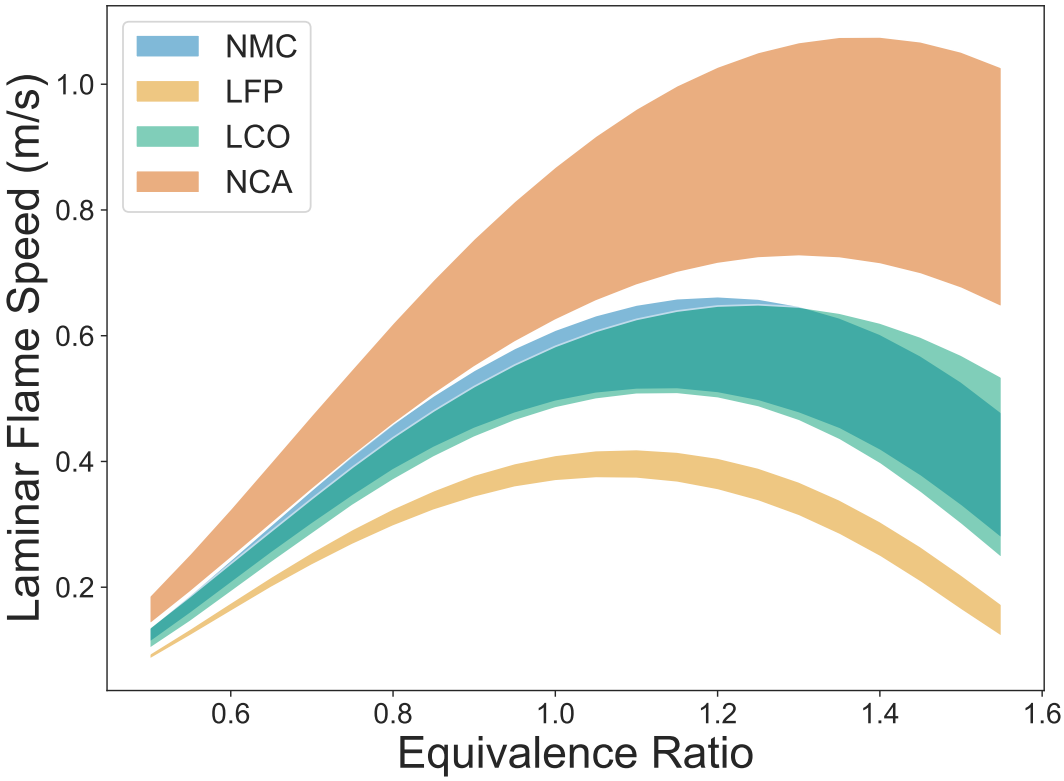

Figure 3.8: Laminar Flame Speed Plots by Cathode Chemistry at 100 % SOC

Figure 3.8 shows the range of flame speeds at 100% SOC for varying chemistries. This figure clearly shows a large difference in the flame speeds for different chemistries at the same SOC. While flammable gas hazards are mainly based on the concentration in space, the results from the flame speed model show that understanding the specific cell state of charge, cathode chemistry, and even form factor is important as they vary for each case as

shown in the literature review. Figure 3.8 also shows that NCA cells clearly have a larger flame speed.

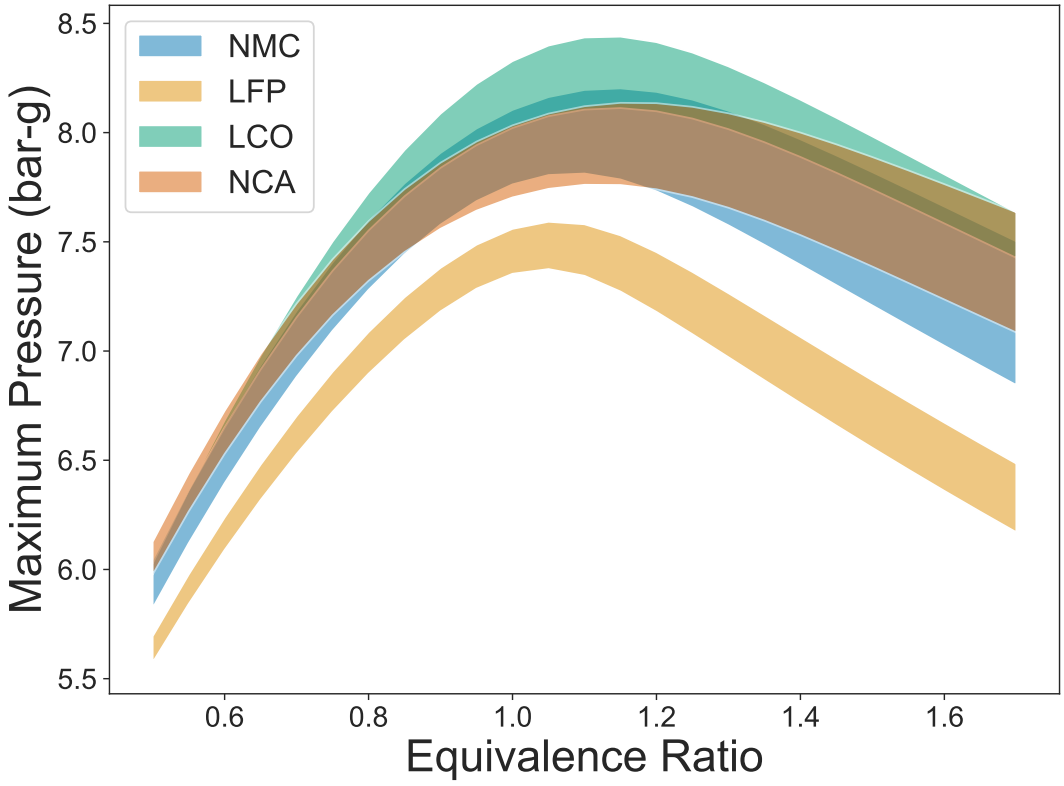

Figure 3.9: Maximum overpressure by Cathode Chemistry at 100% SOC

Figure 3.9 shows the range of pressure for the maximum pressure at 100% SOC for varying chemistries. The maximum overpressure values for different chemistries show less of a variation than the laminar flame speed. The NCA cell chemistry has a lower overall overpressure due to the composition containing more hydrogen, thus having a lower overall molar mass compared to the LCO chemistry vent gas composition. As with the laminar flame speeds, the maximum overpressure is lower for the LFP cells compared with the NCA and LCO cells. Also, as the equivalence ratio increases, the variation in flame speeds and maximum overpressure increases.

3.4 Ranking Vent Gas Hazards

Table 3.8: Range of Battery Cell Model Results at 100% SOC

Cell Chemistry	Lower Flammability Limit (%)	Peak Laminar Flame Speed (m/s)	Maximum overpressure (bar-g)
LCO	5.8 to 8.8	0.50 to 0.66	7.81 to 8.44
LFP	8.6 to 10.0	0.37 to 0.42	7.38 to 7.60
NCA	6.7 to 11.8	0.69 to 1.07	7.74 to 8.13

Table 3.8 shows the range for the lower flammability limit, maximum flame speed, and maximum overpressure. The lower flammability limit values are presented taking the minimum and maximum values from the method by Jones and Bounaceur to establish a range. The values for the flame speed and maximum overpressure are displayed for the equivalence ratio which the maximum flame speed occurs to quantify the hazards of each cell chemistry.

The results overall show that the LFP cell chemistry generally has a higher flammability limit at 100% SOC, which allows more gas to accumulate before reaching a deflagration or fire hazard compared with the NCA or LCO cells. The NCA cells do have one instance where the LFL is higher at 100% SOC, which is the results from Lammer (2017) as seen in table 3.1 which has a higher amount of carbon dioxide compared to the other NCA vent gas compositions. The LFP cells also have a lower overall maximum overpressure and laminar flame speed. This is important when considering safety as both values increase, so does the associated hazard and level of risk. When building structures are intended to house flammable gases such as hydrogen, methane or propane, an understanding of the maximum overpressure and laminar flame speed directly is needed to design via performance or prescribed safety systems.

The NCA cells have a higher concentration of hydrogen by volume and much less carbon dioxide, which is an inert diluent. The overall, hydrocarbons have similar concentrations per volume for all the cells as seen in figure 3.1. In 2015, Li et. al. (104) performed experiments in an explosion tube to compare hydrogen with the hydrocarbon methane.

The experiments compared the flame speed and rate of pressure rise of the two gases when ignited in the explosion tube. The overall conclusions when comparing the two gases is that hydrogen has a higher explosion intensity and will lead to a more massive burst or blast damage. This can directly be associated with the higher flame speed and maximum overpressure shown in the models for NCA and LCO from the effects of hydrogen compared with methane or other hydrocarbons. This directly correlates into the NCA and LCO cells having a higher quantifiable level of hazard compared with the LFP cells when comparing all the models.

With the electrical energy density of NCA and LCO cells being higher, the benefit is a lower overall system weight compared to the LFP cells as shown in the table by Wu et al. (105). Yet with higher pressures and flame speeds, the module and rack designs safety systems should be designed to accommodate the higher consequence level from a deflagration event based on the cell chemistry. To compensate for higher potential burst damage from NCA cells, the module and rack designs may change with heavier duty and thicker materials. Using this approach will potentially cause reconsideration in industries such as aerospace where weight is a large factor and the electrical energy density is measured with the mass of the safety systems being considered.

The intent of this section was to review the hazards associated with different lithium-ion battery cells based on known literature. By understanding the battery vent gas, the lower flammability limit, laminar flame speed, and maximum overpressure were computed. By comparing the overall trends for different chemistries, the level of hazard can be compared. The conclusion was that NCA and LCO cells provide a higher hazard during a failure where off-gassing occurs. With a higher computed lower flammability limit and lower laminar flame speeds and maximum overpressures, the LFP battery can be considered when balancing the performance and allowable risk compared with the NCA and LCO cells. All the computations were completed using methodology and tools are freely available allowing users to analyze their own specific cases. This gives the ability for the safety community to design systems based on their own battery cell parameters.

The findings in this section are based on numerous tests performed over nearly the past 20 years. Each test comprises of specific cell chemistry, electrolyte, form factor, manufacturer, failure mode, cell capacity, SOC and experimental setup. This shows that while a lot of data was covered, to further understand the associated risks and hazards of each of the specific cell parameters encompass need to be investigated. The large range of values within the results from each model shows there is a large variation in the various data sets provided. This shows the need for additional testing to further develop and validate the models. As more testing is completed to understand the species composition along with the gas production and rates at the cell, module and rack levels, further quantifications can be developed to understand the hazards.

3.5 Deflagration Application

In order to characterize Li-BESS deflagration hazards, a comparison with other well-known explosion hazards will be made by comparing deflagration vent sizes. For example, a purpose-built lithium-ion energy storage system container using an off-the-shelf type iso-container is a common way to install a large system on a site without the need for building a structure around it. The example in this application will be a 20 ft x 8 ft x 8 ft (6.1 m x 2.44 m x 2.44 m) container that has a signal Li-BESS rack inside. The total surface area that can have vents installed is 608 ft^2 (65.2 m^2). The structure is assumed to have an ultimate strength of approximately 1.30 psi-g or 0.09 bar-g. The vent sizes for the highest laminar flame speed based on Cantera results will be computed using the methods prescribed in NFPA 68 for each lithium-ion battery chemistry at 100% SOC. Various flammable gases and combustible dusts will also be used to calculate the vent sizes and comparisons will be made.

3.5.1 Explosion Scenario

Determining whether an explosion scenario might occur in the event of a Li-BESS failure depends on if and how quickly it takes to reach the lower flammability limit. Yet various factors will affect this time, such as the vent gas species, total BESS capacity, room ventilation, and gas release rate. The total size of the Li-BESS is important to understand based on how much gas is produced. To characterize the flammable gas, not only does the species matter but so does the concentration. As shown in the vent gas analysis, the flame speed, and overpressure peak when the equivalence ratio is above one or fuel rich. Quantifying the worst case fuel concentration in a space is critical to design the safety systems.

Figure 3.2 shows a slope of roughly 0.46 L of vent gas per kWh. This will be used to determine the total gas volume produced for various capacity systems. With propagation analysis and the total rate at which the vent gas is released still being researched and determined, a conservative number of two hours to total release will be used. The total exhaust rate will match that of the NFPA 1 Ch. 52 requirements at 1 CFM/ft^2 (5.1 L/sec/m^2). For the iso-container, the total ventilation rate is 160 CFM or 76 L/s. By using conservation of mass, the total volume of gas released, and the exhaust rate can be used to determine the time it takes to reach the lower flammability limit. Applying this to the iso-container with the volume already known will show how long different Li-BESS with varying capacities take to reach LFL during failure.

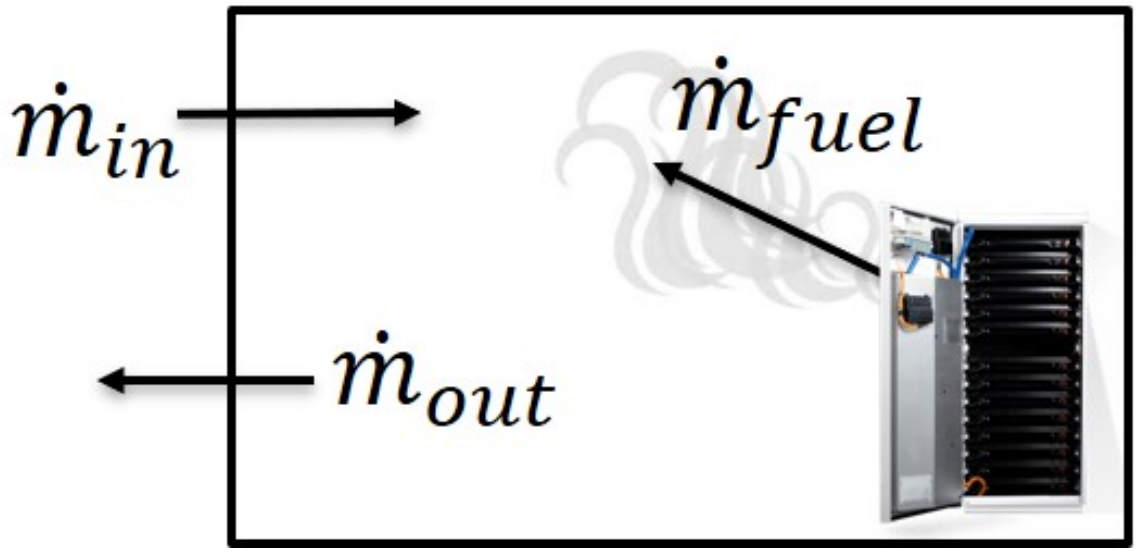

Figure 3.10: Li-BESS Explosion Example

Figure 3.11 shows a simple case of what the mass flows of a perfectly mixed scenario looks like. By using conservation of mass and differentiating, the total change in mass is based on the total inlet and exhaust through space and the rate at which the fuel is vented from the system. With the ventilation and the fuel venting rate known, the fuel concentration over time can be computed. The total enclosure volume is $\mathrm{V_{enc}} = 36.32\ \mathrm{m}^3$.

$$V_{\mathrm{enc}} \frac{dC}{dt} = \rho_{\mathrm{in}} Q_{\mathrm{in}} - \rho Q_{\mathrm{out}} \tag{3.7}$$

Equation 3.7 shows the basic form of conservation of mass for a non-steady state scenario.

$$Q = 14.844m^2 * (0.0051m^3/sec/m^2) = 0.076m^3/sec \tag{3.8}$$

The total volume flow rate from NFPA 1 Ch. 52 is as shown in equation 3.8 after being multiplied by the floor area of the iso-container.

$$\rho(t) = \rho_{\mathrm{fuel}}(1 - e^{-(\frac{Q}{V_{\mathrm{enc}}})t}) \tag{3.9}$$

$$X_{\mathrm{f}}(t) = \frac{\rho_{\mathrm{fuel}} M_{\mathrm{air}}}{\rho_{\mathrm{out}} M_{\mathrm{fuel}}}(1 - e^{-(\frac{Q}{V_{\mathrm{enc}}})t}) \tag{3.10}$$

Using equation 3.10, the time at which the lower flammability limit is reached for various Li-BESS can be obtained. After rearranging and solving the ODE for the conservation of mass in a non-steady state scenario in equation 3.9, the total moles of fuel compared to the total moles exhausted gives the concentration within the iso-container. As the time approaches infinity, the effects of the exponential function go to zero and equilibrium is reached where the concentration of the air and gas becomes constant. This is seen in figure 3.11 below. This is a simple model to help visualize the lower flammability limit and how various system sizes take different times to reach the lower flammability limit if reached at all. This simple model gives a basic understanding of how the volume of space, air ventilation and the failure characteristics of the Li-BESS vent gas hazard.

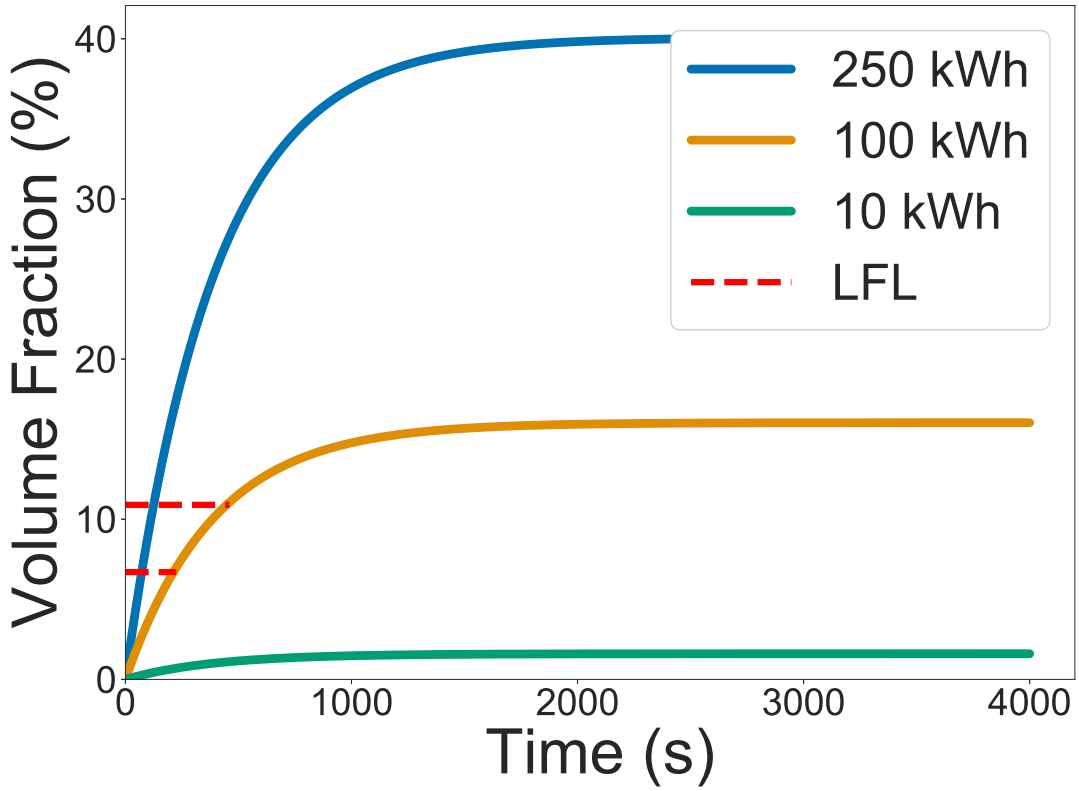

Figure 3.11: Li-BESS Time to LFL

Figure 3.11 shows various capacity systems and how long it takes to reach the lower flammability limit in the given iso-container. The lower flammability range is based on table 3.8 with the three different chemistries. It takes anywhere from about 100 or so seconds for

the 250-kWh system to reach LFL. The 100 kWh takes anywhere from 225 to 460 seconds and the 10-kWh system never actually achieves a gas concentration at LFL. This again is based on the assumptions provided above.

Additionally, the upper flammability limit (UFL) can be used to understand how a sealed system might reach UFL. Note that the 'sealed' system will be assumed to have enough leakage to allow excess gases to leave and keep the pressure from rising.

$$X_{\mathrm{u}} = 6.5\sqrt{X_{\mathrm{L}}} \tag{3.11}$$

A quick method to compute UFL is from equation 3.11 above (87). Using the higher LFL value for the LCO cells at 100% SOC gives a UFL of 21.5% volume.

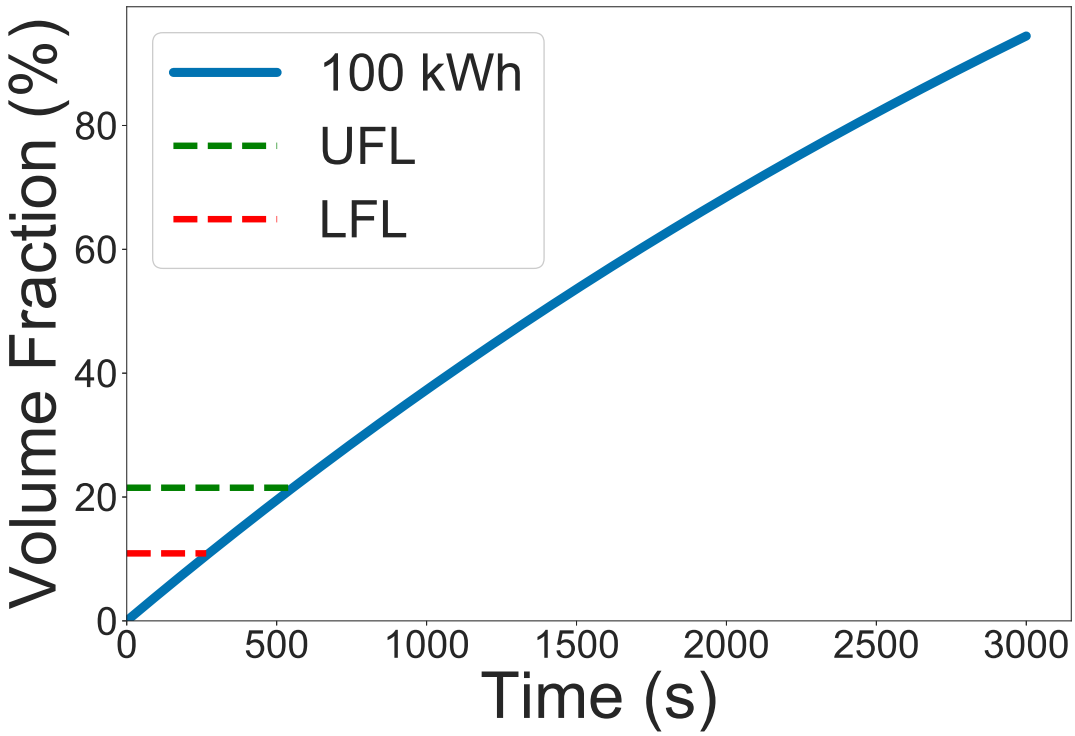

Figure 3.12: Li-BESS UFL Sealed System

While UFL was not explored in this study to that extent that LFL was, it is important to understand. In a sealed system, the gas concentration exceeded the UFL

for this example. This can lead to a delayed ignition explosion condition, with a rich fuel mixture. With the peak flame speed and overpressure occurring with an equivalence ratio above one, this sealed Li-BESS could lead to a higher hazard. If firefighters attempt to enter and inspect and/or shut the system off, the gas concentration can suddenly be reduced below UFL and lead to an explosion scenario.

3.5.2 Deflagration Vent Sizing Guide

With an explosion being potentially occurring in the iso-container example, there are various approaches to prevent or reduce the effects from deflagrations as mentioned in chapter two. In this example, NFPA 68 Ch. 7 will be applied to determine the total vent size for flammable gas mixtures. It will be assumed that a total of ten deflagration vents will be used along the iso-container.

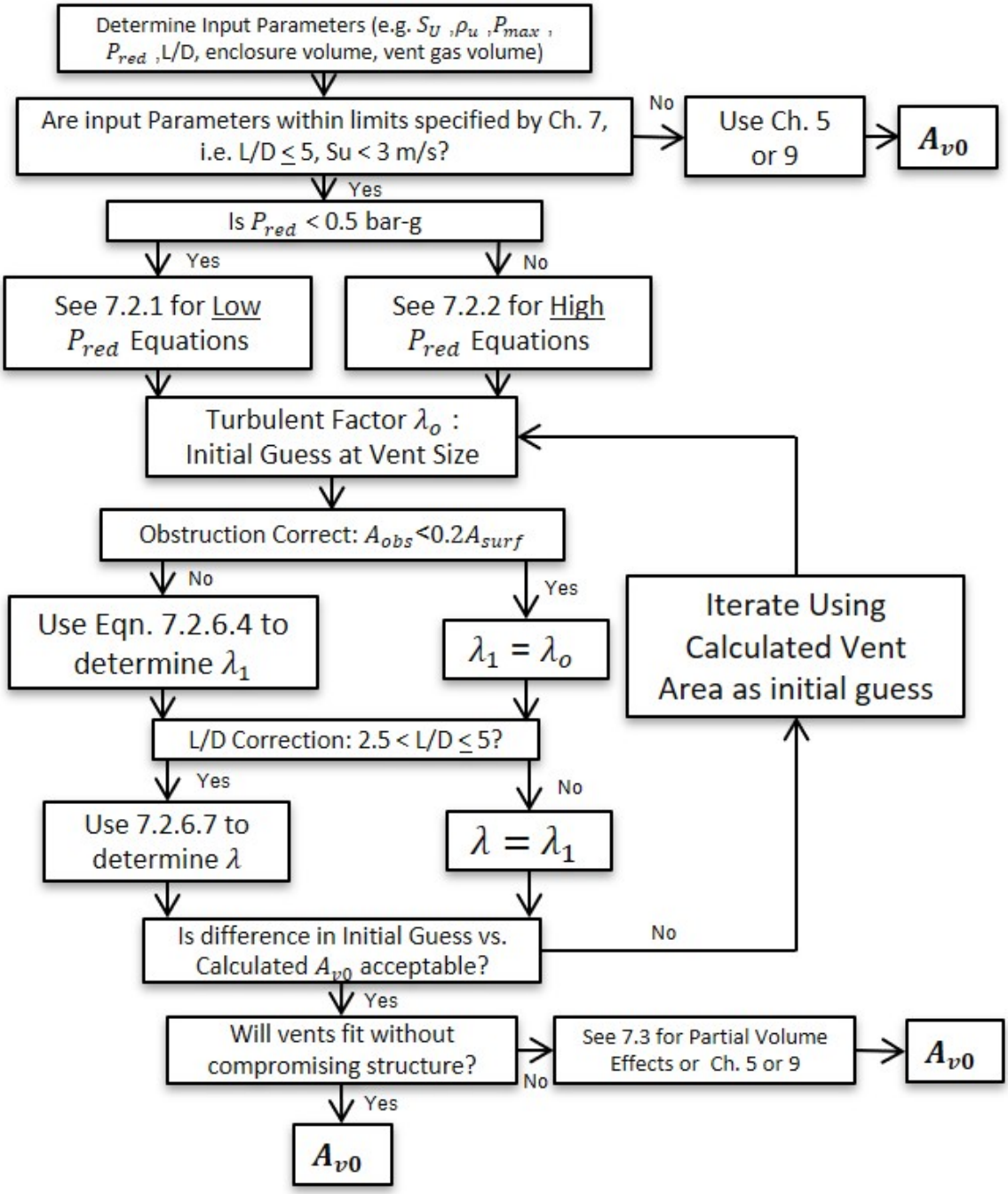

Figure 3.13: NFPA 68 Vent Sizing Flow Chart

Figure 3.13 shows the general flow chart provides to help visualize the process to size deflagration vents. Based on inputs such as flame speed, maximum-pressure, unburned gas density and known parameters such as L/D, enclosure volume, and the total enclosure

ultimate strength, different calculations are used. Based on the limitations of NFPA 68 such as the L/D correlation being less than 5 and the laminar flame speed less than 3 m/s, this method can be used. If these limitations are exceeded, a performance-based analysis must be made within the guidance of NFPA 68 Ch. s five or nine. There are two sets of equations to calculate the vent size: high or low P_{red}. The reduced pressure or P_{red} is the maximum pressure in a vented enclosure. This is unlike P_{max} or the maximum pressure in a non-vented enclosure. The reduced pressure will be based on 2/3 of the total ultimate strength of the structure being analyzed. The following list gives all the variables required for NFPA 68 Deflagration Vent Calculations:

A_{v0} = the vent area calculated from Equation 7.2.1a or 7.2.2a (m^2)

A_S = the enclosure internal surface area determined according to 7.2.5 (m^2)

a_u = unburned gas-air mixture sound speed

C_d = vent flow discharge coefficient, assumed to be 0.70 unless vent occupies a complete wall, then use 0.80

G_u = unburned gas-air mixture sonic flow mass flux (kg/m^2-s)

P_0 = the enclosure pressure prior to ignition (bar-g)

P_{max} = the maximum pressure developed in a contained deflagration by ignition of the same gas-air mixture (bar-g)

P_{red} = the maximum pressure developed in a vented enclosure during a vented deflagration (bar-g)

P_{stat} = vent burst pressure (bar-g)

S_u = fundamental burning velocity of gas-air mixture (m/s)

γ_b = ratio of specific heats for burned gas-air mixture

λ= turbulent flame enhancement factor based on obstructions and L/D, determined according to 7.2.6

μ_u = Unburned gas-air dynamic viscosity (kg/m-s)

ρ_u = mass density of unburned gas-air mixture (kg/(m^3))

In Cantera, the various gas properties can be computed by balancing the species based on the inputted equivalence ratio. The unburned density and gas-air dynamic viscosity are directly computed in Cantera as a gas property. Other values, such as flame speed, maximum pressure, and the sound speed of the gas are computed with separate codes. If the burned properties are needed, then it must go through an equilibrium process using Gibbs free energy method. The burned gas ratio of specific heats can then be computed after this step. The sonic flow mass flux used was based on the prescribed value in NFPA 68. the requirement is the enclosure is at ambient temperatures, 230.1 kg/m^2-s. Additionally, P_0 is assumed to be slightly below atmospheric based on ASHRAE 21, and is assumed to be 1 bar-g. The vent flow discharge coefficient, C_d, is prescribed from NFPA 68 and will be set at 0.70. The total available surface area, A_S, is 56.5 m^2. The cross-sectional area down the long axis of the iso-container is 5.96 m^2.

Most non-purpose-built structures are going to be under the 0.5 bar-g threshold and considered a low P_{red} structure. For example, Annex I in NFPA 68 gives the example of a steel frame, metal-clad building to have an ultimate structure strength of 0.072 bar-g. In this case, the iso-container is assumed to have an ultimate strength of 0.09 bar-g, as it is like the metal-clad type structure, but with thicker walls and rather than fasteners, a welded structure. Using the 2/3 method to find the reduced pressure value, this would give a value of 0.06 for P_{red}.

Based on figure 3.13, the flame speeds must be less than 3 m/s and the L/D must be less than or equal to 5. The hydraulic diameter is assumed to be based on the area along the longer axis of the iso-container. The length to hydraulic diameter ratio is based on the overall length of the structure over the hydraulic diameter, D_{he}. Equation 3.12 gives the prescribed method to determine the general hydraulic diameter from NFPA 68:

$$D_{he} = 4\frac{A_{eff}}{p} \tag{3.12}$$

Plugging in the effective area of 5.95 m^2 and the perimeter of 9.76 m gives a D_{he} of 2.43 m. Then the L/D can be computed with the length being 6.1 m and L/D equal to be 2.50. With this being the case, there is a required L/D correction factor that must be computed. With this known, and the flame speeds for the battery vent gas no more than 1.07 m/s as shown in table 3.8, the vent size calculations can be made through this prescribed method.

Now that all of the inputs and parameters are established, the next step in the flow chart is to determine which vent size equation will be used. Equation 3.13 and equation 3.14 give the low inertia and low P_{red} equations to size the vent area. Low inertia is based on the overall mass per surface area ratio of the deflagration vent panel, which is required to be less than 40 kg/m^2. If the vent panel is greater or equal to 40 kg/m^2, panel inertia effects must be accounted for. In this example, it is assumed the panel is less than 40 kg/m^2.

$$A_{v0} = \frac{AsC}{\sqrt{P_{red}}} \tag{3.13}$$

$$C = \frac{S_L \rho_u \lambda}{2 G_u C_d} \left[\left(\frac{P_{max}+1}{P_0+1} \right)^{1/\gamma b} - 1 \right] (P_0+1)^{1/2} \tag{3.14}$$

If P_{red} is greater than 0.5 bar-g, then the following will be used to compute the deflagration vent size:

$$A_{v0} = A_s \frac{S_L \rho_u \lambda}{G_u C_d} \frac{\left[1 - \left(\frac{P_{\text{red}}+1}{P_{\text{max}}+1} \right)^{1/\gamma b} \right]}{\left[\left(\frac{P_{red}+1}{P_{max}+1} \right)^{1/\gamma b} - \delta \right]} \tag{3.15}$$

Equation 3.15 gives the vent sizing method for a P_{red} is greater than 0.5 bar-g. is based on the rupture or burst pressure, P_{stat}, specified for the deflagration vent as seen in equation 3.16.

$$\delta = \frac{\left[\left(\frac{P_{\text{stat}}+1}{P_0+1} \right)^{1/\gamma b} - 1 \right]}{\left[\left(\frac{P_{max}+1}{P_0+1} \right)^{1/\gamma b} - 1 \right]} \tag{3.16}$$

With the value for P_{red} being 0.06 bar-g, equations 3.13 and 3.14 will be used to determine the deflagration vent area. Ultimately, all of the inputs for C, the Low Inertia Vent Area Coefficient, need to be computed for equation 3.14. Following the flow chart the first turbulence factor, λ_0, needs to be computed.

$$\lambda_0 = \phi_1 \phi_2 \tag{3.17}$$

λ_0 is a function of ϕ_1 and ϕ_2 as shown in equation 3.17.

$$\phi_1 = \begin{bmatrix} 1, \text{ if } \quad Re_f < 4000 \\ (\frac{Re_f}{4000})^{0.39}, \text{ if } \quad Re_f \geq 4000 \end{bmatrix} \tag{3.18}$$

Equation 3.18 gives the first factor to determine the turbulent flame enhancement factor, λ_0. ϕ_1 is based on the Reynolds number of the flame front through the hydraulic diameter of the structure. The Reynolds number is a dimensionless value that measures the ratio of inertial forces to the viscous force which described characteristics that are used to understand the laminar or turbulent flow. The general form is based on the following:

$$Re = \frac{\rho v l}{\mu} \tag{3.19}$$

Where ρ is the density in units of mass/volume, v is the velocity in distance over length and l is the characteristic length. By placing the dynamic viscosity μ in the denominator with units of mass/length-time, the Reynolds number becomes dimensionless.

$$Re_f = \frac{\rho_u S_u (D_{he}/2)}{\mu_u} \tag{3.20}$$

Equation 3.20 gives the calculation for the Reynolds number for the flame front through the hydraulic diameter. The flame speed, unburned gas mixture and dynamic viscosity are computed in Cantera. Once ϕ_1 is computed, ϕ_2 must also be computed. One thing to note on how this calculation is not quite straightforward is the fact that ϕ_2 is based off the Reynolds number through the actual deflagration vent. This requires a guess at the initial vent size. The vent size is then calculated and numerous iterations of the calculation

with the previous resulting vent area inputted as the guessed value used until the resulting value has an acceptable error compared to the guessed value.

$$\phi_2 = max\left[1, \beta_1(\frac{Re_v}{10^6})^{(\frac{\beta_2}{S_u})^{0.5}}\right] \tag{3.21}$$

For equation 3.21, the values for β_1 and β_2 are prescribed constants from NFPA 68, with β_1 being 1.23 and unit-less and β_2 being 2.37x10^{-3} m/s.

$$Re_v = \frac{\rho_u u_v (D_v/2)}{\mu_u} \tag{3.22}$$

The Reynolds number through the actual vent is shown to be dependent on the hydraulic diameter of the vent itself, D_v as shown in equation 3.22 above. Again, D_v is initially guessed and through iterative calculations using the resulting vent hydraulic diameter as the new guessed value.

$$u_v = min\left[\sqrt{\frac{2 \times 10^{0.5} P_{red}}{\rho_u}}, a_u\right] \tag{3.23}$$

The velocity used to calculate the Reynolds number through the vent is based on the effect of choked flow. When the flow of fluid reaches Mach 1 or the speed of sound, the flow is choked and limited to this velocity. The velocity of the mixture through the vent is based on either the pressure and density or the speed of sound of the mixture, whichever is more limiting.

Now that λ_0 can be computed, the next step is to understand how the obstructions and L/D effects are accounted for in the calculations. Obstructions are various equipment and internal structures based on the following:

- Piping, tubing or conduit that is bigger than 1/2" (12.7 mm)
- Structural items such as columns, beams, and joints
- Stairways and railings
- Any other equipment with dimensions ranging from 2" to 20" (50.8 mm to 508 mm)

If the total surface area of the obstructions, A_{obs}, is less than or equal to 20% of the total structure surface area, then λ_1 is equal to λ_0. If A_{obs} is greater than 20% of the surface area of the structure, use equation 3.24 below to determine the obstruction factor:

$$\lambda_1 = \lambda_0 \exp\left(\sqrt{\frac{A_{obs}}{A_S} - 0.2}\right) \tag{3.24}$$

Various obstructions can cause the flame front to propagate quicker. This is due to the flame acceleration around the obstructions. This can cause turbulence, drastically increasing the flame speed into the hundreds of meters per second which causes higher pressures and can lead to more damage from deflagration. The study by Gexcon (106; 107) showed various scenarios of deflagration inside of an iso-container. The different tests showed the effects of hydrogen gas explosions due to change in hydrogen volume, deflagration vent sizes, and various obstructions. As the obstructions increased due to additional gas cylinders and pipe-racks the maximum pressures raised from 0.146 bar-g to about 0.25 bar-g.

$$\lambda = \lambda_1 \left[1 + \left(\frac{L/D}{2.5} - 1\right)^2\right] \tag{3.25}$$

Once the effects of obstructions are determined, the final flame enhancement factor to determine is for the L/D relationship. As determined before, L/D is exactly 2.5 for this iso-container. Based on equation 3.25, this would mean λ_1 would equal λ. This is also the case for any L/D less than 2.5. If the L/D value is between 2.5 and 5, equation 3.25 applies. Anything over 5 for L/D, as previously mentioned other methods not prescribed in NFPA 68 Ch. 7 will need to be used. Essentially, as L/D increases, the flame speed also does as there is more confinement involved with a long and narrow structure such as a pipe or tunnel. In a non-vented case with a higher L/D, the flame front will propagate from one end to the other, decelerating as pressure begins to build due to the trapped fuel on the opposite end. In some cases, the flame will propagate in two directions based on the ignition point. With the large L/D, there is the potential for the flame speed to increase to transition from deflagration to a detonation (108). This is the main reason NFPA 68 limits the L/D to prevent the calculations from breaking down due and staying conservative.

Once the flame enhancement factor has been set, the results for the vent area can be computed using equation 3.13 and 3.14. These results are then used to input as the guessed results in the calculation for the Reynolds number through the vent.

3.5.3 Combustible Dust

While combustible dust is not the focus point of this analysis, it will be used to use as a further comparison to the vent gas deflagration hazard. The deflagration index, K_{st} (bar-m/s), is used to rank the explosion hazard of combustible dust. Another important parameter for the analysis of explosion scenarios is the rate of pressure rise. The rate of pressure rise is usually compared using the parameter Kg, which is calculated using the maximum rate of pressure rise $\frac{dp}{dt}$ and the volume V as shown below.

$$K_g = \frac{dp}{dt} V^{\frac{1}{3}} \tag{3.26}$$

The combustible dust index has three classes, with a class one having a K_{st} value from 0 to 200 bar-m/s, class two having a K_{st} value from 200 to 300 bar-m/s and class three having a K_{st} value above 300 bar-m/s (109). Some examples of a class one are sugars, powdered milk, a class two can be wood flour, cellulose and a class three could be aluminum or magnesium (36). While the flame speed is used to analyze flammable gases, this deflagration index is still used in deflagration safety standards, such as NFPA 68. Deflagration vents will be sized in accordance with NFPA 68 Ch. 8 for this iso-container example.

3.5.4 Vent Size Results

The method used to compute the deflagration vent size for the flammable gas mixtures was to take the equivalence ratio for the highest possible flame speed. This is conservative since the flame speed is directly multiplied in equation 3.14 so as it increases, the vent size directly increases. Once the concentration of gas is determined, it is assumed

the total iso-container is filled to the with the specific gas composition and worst-case concentration.

Table 3.9: Deflagration Vent Size for Explosion Hazards

Deflagration Hazard:	**Flame Speed (m/s)**	**Kst (bar-m/s)**	**P_{max} (bar-g)**	**Vent Size (m^2)**
Class 1 Dust: Sugar	–	138	8.5	5.2
Class 3 Dust: Aluminum	–	415	12.4	19
Propane	0.40	–	8.6	5.2
Hydrogen	2.80	–	7.4	33
LCO 100% SOC	0.49 - 0.65	–	7.8 - 8.4	6.7 to 10
LFP 100% SOC	0.37 - 0.42	–	7.4 - 7.6	4.0 to 4.9
NCA 100% SOC	0.69 - 1.07	–	7.7 - 8.1	10 to 32

Table 3.9 shows various vent sizes for the prescribed iso-container. Two different combustible dusts, sugar at a class one and aluminum at class two were added as a comparison. As discussed before, the combustible dust used the deflagration index, whereas flammable gases use the flame speed to size the vents. Appendix A gives the code used to compute the vent sizes for flammable gas hazards.

The various compositions for each cathode chemistry at 100% SOC are also presented in table 3.9 along with hydrogen and methane. The range for compositions with the highest and lowest flame speed from various literature are shown also. This gives an understanding of how the three compositions compare with known hazards. As shown earlier, the LFP chemistry has the lowest flame speed and P_{max} compared to LCO and NCA. This shows with the results of the deflagration vent size being much less than the lower end sizes for both LCO and NCA cell chemistry. The NCA cell chemistry shows a much higher vent size on the upper end of the range at 32 m^2, like hydrogen. This is due to both a higher flame speed, but also a higher P_{max}. The NCA cells can be compared somewhere along the lines of class three combustible dust and hydrogen. This factor should be highly considered in designing systems using NCA cells. Additionally, with the results from table 3.1 consisting of varying form factor types, failures, and cell capacities, these effects must be further investigated to understand how they affect the species compositions. But this vent size analysis helps understand how Li-BESS systems compare with well-known hazards that have already been researched and mitigated.

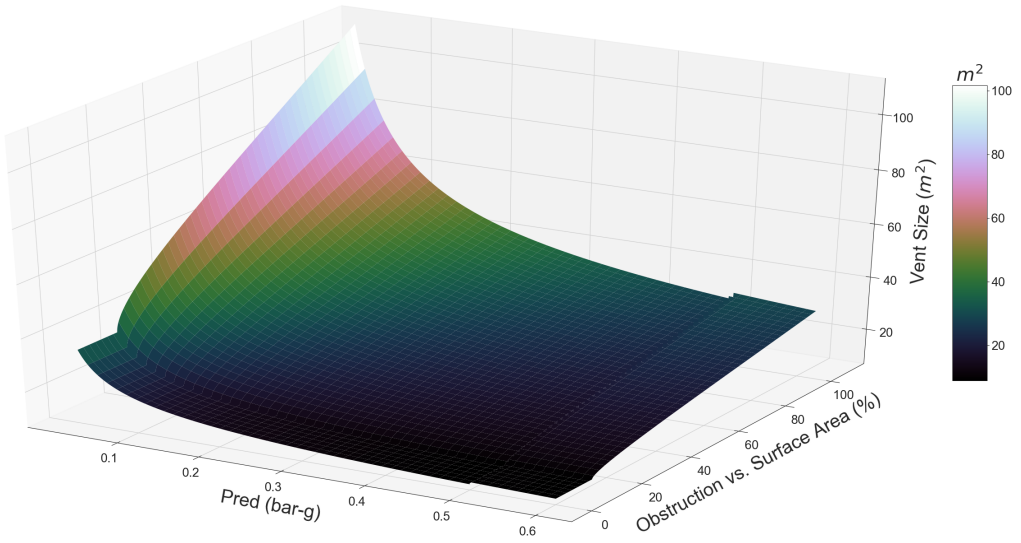

Figure 3.14: Vent Size vs Obstruction vs Pred

Figure 3.14 above shows the effect of obstructions and P_{red} on the total vent size. The iso-container application with the NCA cell chemistry and composition with the highest flame speed was used for this analysis. This shows both how a higher P_{red}, from 0.05 to 0.15 bar-g, reduces the vent area to roughly half. The biggest contribution to a large required vent area is based on the number of obstructions. With purpose-built iso-containers containing all the necessary equipment to operate Li-BESS which includes conduit, control equipment, transformers, inverters, cooling systems, structural beams and reinforcements and other various objects that meet the criteria. As these obstructions increase, the total required vent area increases as shown in equation 3.24, as an exponential function of the square root of the obstruction surface area to container surface area. The total vent size drastically increases as the obstruction area gets above about 30% especially at lower P_{red} values below 0.1 bar-g.

Table 3.10: Obstruction Examples

Obstruction Description	Dimensions	Quantity	Obstruction Area (m^2)	% of Total Surface Area
Conduit, Large	50.8 mm round by 1.82 m long	10	0.036	0.0637
Conduit, Small	12.7 mm round by 1.82 m long	60	0.013	0.0230
Control Systems	0.5 m^3	6	7.5	13.27
HVAC Equipment	0.2 m by 0.2 m by 0.1 m	5	0.02	0.0354
Fire Panel	0.2 m by 0.2 m by 0.05 m	2	0.004	0.0071
Total Obstruction Area Percentage of Iso-container Surface Area (%)				13.40

Table 3.10 shows various examples of obstructions that might be found inside of the energy storage iso-container. While the total surface area of the obstructions does not exceed 20% of the total surface area in these examples, if these energy storage systems were installed in equipment rooms packed with additional equipment and conduit it could exceed this threshold. With large numerous conduits and piping systems along with pumps, control panels, structural members and more. As these systems are installed in different locations, it is important to understand these obstructions and how the vent size is greatly affected by them.

Studies have been performed to show the effects of blockage or obstructions on both flame speeds and overpressure. Various experiments to determine the effect of blockage on flame speeds and overpressure were performed in a cylindrical vessel by Na'Inna at al. (110). Methane was ignited, and the maximum flame speed and pressure was determined. As the blockage ratio increased, from 0 to 0.4, the flame speed went up by about 4-5 times and the maximum pressure went up by about 10 to 12 times. Blockage due to a cross-sectional area, not a surface area would make more sense. NFPA 68 specifies the total external area surface area of obstructions rather than a cross-sectional area. This needs to be further investigated and updated.

3.6 Partial Volume Effects

If the vent area calculated using a full volume deflagration cannot be feasibly integrated without having issues with the actual structure, partial volume effects are permissible. Rather than assuming the iso-container or other space is filled completely with a specified gas, a specific volume of gas can be used. This is more of a performance based design and is less conservative.

$$X_r = (\frac{V_{gas}/V_{enc}}{x_{st}}) \tag{3.27}$$

Equation 3.27 gives the partial fill fraction based on the stoichiometric volume concentration and the ratio of gas volume to structure volume. If the fraction is less than one, the partial volume method can be used. Essentially, what equation 3.27 shows is whether the mixture in the space is fuel rich or fuel lean, based on the stoichiometric concentration. If the mixture is fuel lean, then partial volume computations are allowed. If the mixture is fuel rich, then the initial vent area must be used.

$$A_{vl} = A_{v0}{X_r}^{-1/3}\sqrt{\frac{X_r - \Pi}{1 - \Pi}} \tag{3.28}$$

$$\Pi = P_{red}/P_{max} \tag{3.29}$$

Based on equations 3.28 and 3.29, the partial volume vent area is based on the ratio of pressures and the partial volume fill fraction in order to reduce the total area. The most difficult part of this method is to determine the total volume and composition of a gas cloud that is produced by Li-BESS. In other scenarios might be better understood such as a gas leak. If the flow rate of a gas leak can is known, along with the response rate to shut the gas leakage off, the total volume in the space can be calculated. Additionally, with a single gas, the stoichiometric concentration can easily be understood. Yet, with Li-BESS the volume and composition are based on the state of charge, form factor, failure, capacity, and chemistry, showing how this method should be implemented as conservatively as possible.

Using the iso-container with a total enclosure volume, V_{enc}, equal to 36.32 m^3, using figure 3.2 showing the total volume release of 0.46 L/Wh, the partial method can be used. Based on figure 3.11, a 30-kWh system can be used in conjunction with the volume to capacity production to determine the volume produced, V_{gas}. A 30-kWh system would produce 13800 liters of gas or 13.8 m^3.

Table 3.11: Partial Volume Calculations

System Capacity (kWh)	Total Volume Produced (m^3)	Cell Chemistry	Stoichiometric Fuel Concentration	Pmax (bar-g)	Fill Fraction	Initial Vent Size (m^2)	Partial Volume Vent Size (m^2)	Difference from Full Volume (%)
30	13.8	LFP	0.28	7.6	1.36	4.9	4.9	0
		LCO	0.238	8.4	1.60	10	10	0
		NCA	0.249	8.1	1.53	32	32	0
15	6.9	LFP	0.28	7.6	0.68	4.9	3.5	28
		LCO	0.238	8.4	0.80	10	8.3	17
		NCA	0.249	8.1	0.76	32	25.5	20
7.5	3.45	LFP	0.28	7.6	0.34	4.9	2.0	60
		LCO	0.238	8.4	0.40	10	4.6	54
		NCA	0.249	8.1	0.38	32	14	55

Using equations 3.27, 3.28 and 3.29, table 3.11 shows how the partial volume calculations based on the total volume produced from various sized Li-BESS systems. Based on the requirement for X_r to be less than one for partial volume calculations to be allowed, only the 7.5 and 15 kWh systems meet this requirement. The 30-kWh system produces too much gas by volume based on the rate of 0.46 L/Wh. It will still require the same sized vents as calculated in table 3.9. The partial volume effects for the 15 kWh systems reduced the total vent area by 17-20%. The 7.5 kWh system has a much larger reduction in total vent size, anywhere from 54-60%. For the NCA cell chemistry, the vent size reduced by 18 m^2 or 32% of the total iso-container available surface area. As noted, before, this more of a performance-based calculation, with assumptions of the total volume playing a large role in this reduction of vent area.

Computing the deflagration vent size for the example iso-container is done with an understanding of the Li-BESS chemical species and characteristics along with prescribed standards. By using NFPA 68 to size deflagration vents for various cell chemistries, an understanding of how the explosion hazard of Li-BESS ranks with other well-known species was established. Taking this known prescriptive method and exercising is at this level helps understand the hazard. This is a great starting point for this understanding and should be further researched and understood.

Chapter 4

Lithium-Ion Cell Fuel Load and Fire Guidelines

In addition to explosion hazards, Li-BESS present a unique fire hazard. As previously mentioned, the suppression system designs for these systems are challenging and no formal guidance is available. This presents a unique challenge for the safety community. While some large-scale tests have been conducted on both bulk storage of lithium-ion cells along with Li-BESS, an understanding of the small-scale testing is important to help characterize and understand these larger scale tests. Various tests using oxygen consumption calorimetry will be performed in order to help understand on a cell and cell array level how the heat release rate and total heat released compares with other commodities.

4.1 Current Suppression Methods

As mentioned in chapter two, NFPA 13 does not have any guidance for designing sprinkler systems for lithium-ion cells in general. This applies to both Li-BESS and individual lithium-ion cells. Yet the current draft for NFPA 855 states that water is the preferred agent for fighting lithium-ion battery fires. At a large-scale level, FM Global has performed two sets of tests: flammability of lithium-ion cells in bulk storage (59) and development of sprinkler protection for Li-BESS (111). This bulk storage test compared various lithium-ion commodities in rack storage with cartoned unexpanded plastic and class 2 commodities. When comparing the heat release rate, lithium-ion cylindrical and polymer cells have small bump followed by a large increase in the HRR with multiple bumps as the lithium-ion cells and other combustibles were involved in the fire. The class 2 commodity and cartoned unexpanded plastic commodity had a lot quicker and sharper HRR, with one large spike compared with the lithium-ion cells.

With bulk storage, sprinkler effectiveness is based on activation time, coverage and

capacity. Li-BESS present a unique hazard due to the sealed nature of the system. With the racks being closed, this prevents effective coverage of a suppression system directly onto a lithium-ion battery fire. Additionally, the electrical energy present in these systems presents an additional hazard. NFPA 13 Ch. 8 does not require sprinkler systems in electrical rooms when there is only dedicated electrical equipment, dry-type electrical equipment enclosed by two-hour fire barriers and no combustible storage. With the possibility of Li-BESS installed in an existing electrical type room, suppression systems may not be installed. This makes it difficult to enforce suppression systems for Li-BESS with lack of documentation or understanding on whether it is needed or not. The presentation by Ben Ditch from FM Global at the 2018 NFPA SUPDET Suppression Program Presentation gave a preview of the large-scale testing performed to evaluate sprinkler performance on Li-BESS. This test has yet to be fully released but gives some ideas of free burning and sprinkled Li-BESS and what their recommended sprinkler design practice is.

One similar comparison to Li-BESS is server racks in term of the shape of the system and electrical hazard. Again, with Li-BESS, using a suppression system that involves water can lead to an electrical hazard. Additionally, remote locations do not necessarily have the quantity of water required to fight these fires. If these systems are installed at a substation in a remote location without a consistent water supply provided, fighting a Li-BESS fire will be difficult. As shown in chapter two, various lithium-ion battery fires have been extinguished by constant water. A recent example shows a BMW i8 all-electric car being dunked into a pool of water as a method to extinguish the fire and left there while the batteries would be cooled and was no longer a hazard (112). Telsa has guidelines that suggest it takes approximately 3000 gallons of water to fight a fire for 2016+ Model S all-electric vehicle or to use other methods such as CO_2, dry chemicals or foam if enough water is not available (113). Tesla also suggests allowing the battery to burn for up to 24 hours while protecting all exposures. Leading back into the remote location, such as a sub-station or a renewable resource system, a fire without enough water could lead to a potential wild-land fire hazard. This brings up an entirely other hazard based on issues with extinguished fires within these systems. These systems might require a large water supply, that may not be easily

transported to a remote location. With Li-BESS racks being enclosed, it is difficult to get water directly on the cells, which shows how the method of almost flooding the system is needed. This is just an example of how difficult it is to quantify what the safety community should do in terms of suppression, especially without proper guidance to size the water system in NFPA 13 for lithium-ion cells. NFPA 13 Ch. 5 gives the following break-down for classification of commodities:

- Class I: Noncombustible product placed on wood pallets, within corrugated cartons, paper or shrink-wrapped
- Class II: Noncombustible product within wood crates, multi-layered corrugated cartons or equivalent
- Class III: Wood, paper, natural fibers or group C plastics
- Class IV: Group B plastics, Containers containing 5%-15% group A unexpanded plastics or 5% to 25% group A expanded plastics, or refer to figures 5.6.3.3.3

Each of these different classes of commodities requires different sprinkler design approaches and requirements. NFPA 13 Ch. 14 gives various sprinkler density requirements. For various classes and storage heights, the requirements such as K-factor, operating pressure, and sprinkler density. The K-factor rates the discharge rate from the nozzle of a sprinkler head. Understanding these commodities and how lithium-ion cells are characterized by bench-scale cone calorimeter testing will help establish the fire hazard associated with Li-BESS.

By understanding the smaller scale of how lithium-ion cells fail when burning, and comparing to larger tests, characterizations and comparisons with other similar fire hazards can be established. The array testing will provide an understanding of how long it takes for one failed cell to propagate that failure to another. Additionally, this will help bring an understanding of whether or not single cell data can be scaled to larger failures. This exploratory type testing can help establish a way to further evaluate and understand the fire safety of lithium-ion cells with both qualitative and quantitative analysis.

4.2 Cone Calorimeter Testing

The heat release rate (HRR) is the rate at which combustion occurs and produces heat and is measured in Watts. Full-scale HRR testing can be used to determine the characteristics of full room fires. The total heat released (THR) is the total heat generated from the complete combustion of a sample and is measured in Joules. The THR from a bench-scale test can be used to obtain the heat of combustion. This can then be used when summing fuel loads in a space to characterize the overall fire hazard. The heat of combustion is the heat released per mass burnt and is a way to quantify fuel loads in units of kJ/g. In testing larger scale fires, items such as sofas, furniture, and bulk storage of commodities will help understand how fires evolve within the space and help make materials safer. Small-scale or bench-scale testing is used to characterize certain materials such as plastics and foams in order to compare and rank them with another. Understanding bench-scale data can help understand and predict full-scale HRR and THR.

The bench-scale cone calorimeter uses the concept of oxygen consumption to measure the HRR. With the exhaust gas oxygen concentration known, the HRR in kW is given by the following per Chow et al. (114):

$$\dot{q} = E(\dot{m}^0{}_{O_2} - \dot{m}_{O_2}) \tag{4.1}$$

From equation 4.1, the mass flow of air from the intake gas, $\dot{m}^0{}_{O_2}$ and the mass flow of air in the exhaust gas, $\dot{m}_{O_2}$ is measured and the oxygen consumed directly is proportional to the HRR. As previously discussed, E is based on the heat of combustion to the oxygen consumed and for most fuels, it equals 13.1 MJ/kg_{O_2} (115). Additional corrections for incomplete combustion where other species such as CO, CO_2 and H_2O are present in the exhaust stream, additional corrections can be made using the following for incomplete combustion of carbon monoxide and soot:

$$\dot{q} = E(\dot{m}^0{}_{O_2} - \dot{m}_{O_2}) - (E_{CO} - E)\Delta\dot{m}^{CO}{}_{O_2} - (E_S - E)\Delta\dot{m}^{S}{}_{O_2} \tag{4.2}$$

In equation 4.2 according to Chow, E_{CO} is approximately 17.7 MJ/kg_{O_2} and E_S is approximately 12.3 MJ/kg_{O_2}. Understanding and interpreting the results from these calculations can be used for several metrics in such as predicting fire behavior, understanding and ranking various hazards, and testing fireproofing and resistant materials. The THR is based on the area under the curve and is calculated from the following:

$$THR = \int_0^\infty \dot{q} dt \tag{4.3}$$

Equation 4.3 shows how to compute the total heat released or THR. The HRR shows how quickly a sample will take to burn and relates the fire size and hazard. The THR gives an idea of how much heat the sample releases in that time. Various materials could have different HRR curves, with one having a shorter burn time but a larger peak than the other. Yet the THR could be very similar. The HRR is important to understand due to having an object burns can affect any exposures.

4.3 Flammability Literature Review

Numerous studies have been conducted to determine the HRR and THR from burning lithium-ion cells. In 2012, Ribiere et al. (62) used a Tewarson calorimeter to determine the HRR of 2.9 Ah pouch cells. A Tewarson calorimeter is similar to the mentioned cone calorimeter, but rather than having a conical heater above the sample, infrared heaters are placed along the sides and pointed at the sample (116). A tube is used to entrap the gases coming due to the combustion of the sample, which is pulled into the collection hood and analyzed. These HRRs were compared with other fuels such as gasoline, PMMA, and polyethylene. The HRR of cells at 0%, 50% and 100% SOC were determined while burning the cells with a heat flux of 35 kW/m^2. Somandepalli et al. (117) also performed similar experiments using oxygen consumption calorimetry, but with LCO 2.1 Ah pouch cells. A heat flux of 35 kW/m^2 was also used to burn cells at 0%, 50% and 100% SOC.

Cylindrical cells, such as 18650 size, are more volatile compared to pouch cells due to the construction and configuration. Unlike a pouch cell, the 18650 cell has a rolled electrode or 'jelly roll'. The roll is placed into a hard-cylindrical case with a burst disk or safety vent on the end. Quintiere et al. (118) with the University of Maryland and the FAA conducted additional testing at the cell level to determine the flammability and fire hazards associated with cylindrical cells. Specifically, 2.6 Ah 18650 LCO cells were tested. An oxygen consumption cone calorimeter was used to determine the HRR, and THR for various heat fluxes to burn the cell. A modified version of the standard ASTM E1345 sample holder was used to capture vent gases ejected from burning cell. These tests were performed using various heat flux settings and for cells having a range of different SOC. The FAA also performed thermal capacitance calorimetry to determine the energy required for cell failure. Fu et al. in 2015 (75) exposed 18650 type cells a heat flux ranging from 30 to 60 kW/m^2 on cells with a SOC ranging from 0% to 100%. With 18650's being so volatile, Fu et al. noted the time to 'explosion' with the pressure build up released from the burst disk. In 2015 and 2016, Liu et al. (119; 120) used a copper slug calorimeter to determine the heat required to induce a failure. Three different cathode chemistries were used in these experiments, including LCO, NMC, and LFP at varying SOC. The slug calorimeter was placed with a hot wire above it in a standard cone calorimeter. This determined the HRR and the failure point of the cylindrical cells.

While individual cell flammability testing shows the properties of various cells, understanding the effects of propagation and how the hazard scales up is also important. In 2015, Ping et al. (121) performed full-scale burning tests on an off the shelf 10 Ah LFP cells in a 5-cell array. The largest face of the cells was pointed in the horizontal direction and exposed to a 3-kW heater. The setup was placed in an ISO 9705 Full-Scale Room Fire Test for Surface Products apparatus. The gas flue was collected and analyzed to determine the HRR. Thermocouples were placed on the outside of the cell array on all sides except for the bottom. Three tests were conducted with arrays at 0%, 50% and 100% SOC. The effect of SOC and the HRR was determined, as the SOC increases, so do the peak HRR. The peak HRR at 0% SOC is 7.7 kW, at 50% SOC it is 15.5 kW and at 100% SOC it peaks

at 18.9% kW. As the SOC increases, the HRR nearly triples from 0% SOC to 100% SOC. In 2016, Larsson et al. (122) used a propane burner with an HRR of 16 kW underneath a five-cell array consisting of LFP pouch cells. By using LFP cells, oxygen production at higher SOC values was not an issue in this test. The cells were wrapped together with safety wire, and thermocouples were placed in-between each cell interface. By using oxygen calorimetry method to determine the HRR can be determined for this array. Additionally, the thermocouples establish the effects of failure from the top cell and how that failure propagates through the array. Models using this data were created to help estimate the effect of fire barriers in between the cell interfaces. The results of this review are tabulated in table 4.1 below.

Table 4.1: Summary of Cell Abuse Literature

Reference	**Type of Cell**	**Total Capacity**	**Cathode Chemistry**	**Electrolyte**	**Initial SOC (%)**	**Measurement Apparatus**	**Failure Test**
Ribiere (2012)	Pouch	2.9 Ah	LMO	EC:DEC: DMC	0/50/100%	Terwarson Calorimeter	Infrared Heater at 35 kW/m2
Somandepalli (2014)	Pouch	2.1 Ah	LCO	EC:DMC: DEC:PC	0/50/100%	Cone Calorimeter	Cone Heater at 35 kW/m2
Quintiere (2016)	18650	2.6/1.5/0.75 Ah	LCO/LMO	N/P	Varied from 0% to 100%	Cone & Slug Calorimeter	Cone Heater from 0 to 75 kW/m2
Fu (2015)	18650	2.6 Ah	LCO	N/P	0/50/65/70/100%	Cone Calorimeter	Cone Heater at 30/50/60 kW/m2
Liu (2015/2016)	18650	2.2 Ah	NMC/ LCO/LFP	N/P	0/25/50/100%	Cone Calorimeter	Copper Slug with Heating Elements
Ping (2015)	5 Prismatic Cell Array	50 Ah	LFP	N/P	0/50/100%	ISO 9705 Full-Scale Room Fire Test Apparatus	3 kW Radiation Heater
Larsson (2016)	5 Pouch Cell Array	35 Ah	LFP	N/P	0/75/100%	Oxygen Consumption Gas Analyzer	16 kW Propane Burner

4.3.1 Testing Setup and Procedures

Various tests were performed using lithium-ion pouch cells and ASTM E1354-17: Standard Test Method for Heat and Visible Smoke Release Rates for Materials and Products Using an Oxygen Consumption Calorimeter (123). The standard FTT Cone Calorimeter setup from Fire Testing Technology was used for this experiment. This system uses oxygen depletion calorimetry in order to understand the combustion process and the HRR can be determined from these measurements (116). The testing order went as follows:

1. Preliminary pouch cell cone calorimeter tests consisting of 500, 800, 1500 and 2000 mAh cells
2. Three single pouch cell tests at 0% SOC using 500 mAh and 800 mAh cells
3. Three single pouch cell tests at 0% SOC and electrolyte dried out for 72 hours using 500 mAh and 800 mAh cells
4. Three sets of five cell array at 0% SOC using 500 mAh and 800 mAh cells
5. Three sets of PMMA arrays using 5 3/16" samples with metalized moisture-resistant polyester film

All of the cells used Lithium cobalt oxide or LCO as the cathode chemistry. Preliminary tests were performed to gain an understanding of how the cells react in the cone calorimeter and to decide what changes should be made in order to test arrays of cells. One test of a single 500, 800, 1500 and 2000 mAh cell at 0% SOC and dried out cells were done just as a baseline. One of the main concern was the effect of jetting and gas production overwhelming the sensors. During preliminary testing, it was determined that the cells can be centered in the sample tray, but the tabs of the pouch cell would need to be placed such that they are on the back side or opposite side of the sample tray handle. It was noticed that the tab side would start to off-gas first and with the spark ignitor above would cause the sample to ignite. Placing the cell at the center of the sample tray with the tabs away from the handle of the tray such that the ignitor was above the tabs was used for both single and array tests. The 500 mAh cells were slightly off-set towards the ignitor due to the smaller size for the single cell tests.

The main reason for keeping the cells at a nominal charge of zero is due to the oxygen production associated with LCO cells. When oxygen consumption is the method used to measure the HRR in the cone calorimeter experiments, any material that produces oxygen will affect the measurement. While the total oxygen production can be established, understanding the rate of oxygen production while the cell is burning is difficult to understand and has not established. To the oxygen production for LCO cells has been established in

studies by MacNeil et al. (124), Yamaki et al. (125) and from Wang et al. (126) give the following suggested reaction for the decomposition of the delithiated LCO cells, Li_xCoO_2:

$$Li_xCoO_2 \rightarrow xLiCoO_2 + \frac{1}{3}(1-x)Co_3O_4 + \frac{1}{3}(1-x)O_2 \tag{4.4}$$

In equation 4.4 established by Wang, Yamaki and MacNeil, the oxygen generation from the breakdown of the cathode material releasing oxygen, enabling the burning of the electrolyte. The minimum value for x is 0.5 and the maximum value is 1. As the cell voltage or SOC decreases, the value for x increases, giving a lower oxygen production during failure. At a value of 1 for x, the oxygen production is either very little to none. This is important to consider when using oxygen consumption as a method to measure HRRs.

Table 4.2: Pouch Cell Specifications

Model Number	Dimensions: (HxWxL) mm	Major Cross Sectional Area (mm^2)	Volume (mm^3)	Nominal Capacity	Nominal Voltage	Nominal Energy	Discharge Current Used	Cutoff Voltage
PL-403144-2C	4.3 x 34.5 x 40.0	1380	5934	500 mAh±5%	3.70 V	1.85 Wh	250 mA	2.75 V
PL-383562-2C	3.9 x 35.5 x 63.5	2254	8792	800 mAh±5%	3.70 V	2.96 Wh	400 mA	2.75 V

The first set of tests performed was with 0% SOC cells under a heat flux of 50 kW/m^2 consistently for all tests. The cells were charged at 1 C to 100% SOC then discharged at 0.5 C to 2.75 volts or nominally 0% SOC. The tests were done using the standard ASTM E1354 sample tray, by placing the cell at the center of the tray and using kaowool to raise the top of the cell to nominally 25.4 mm below the conical heater.

The second set of tests were using the same cells, this time by drying cells out to remove the electrolyte. After discharging the pouch cells, the end opposite of the tabs was sliced open and the tape holding the separator sheets together was also sliced in half. The separator sheets were spread apart as much as possible and the cells were pulled opened without deforming the actual pouch. After being cut open, the cells were placed into a vacuum hot plate for 72 hours at approximately 176 °F (80 °C) while at 27.0 inHg (91.4 kPa) below ambient pressure. The intent of the lower the pressure and the raised temperature was to promote evaporation of the electrolyte.

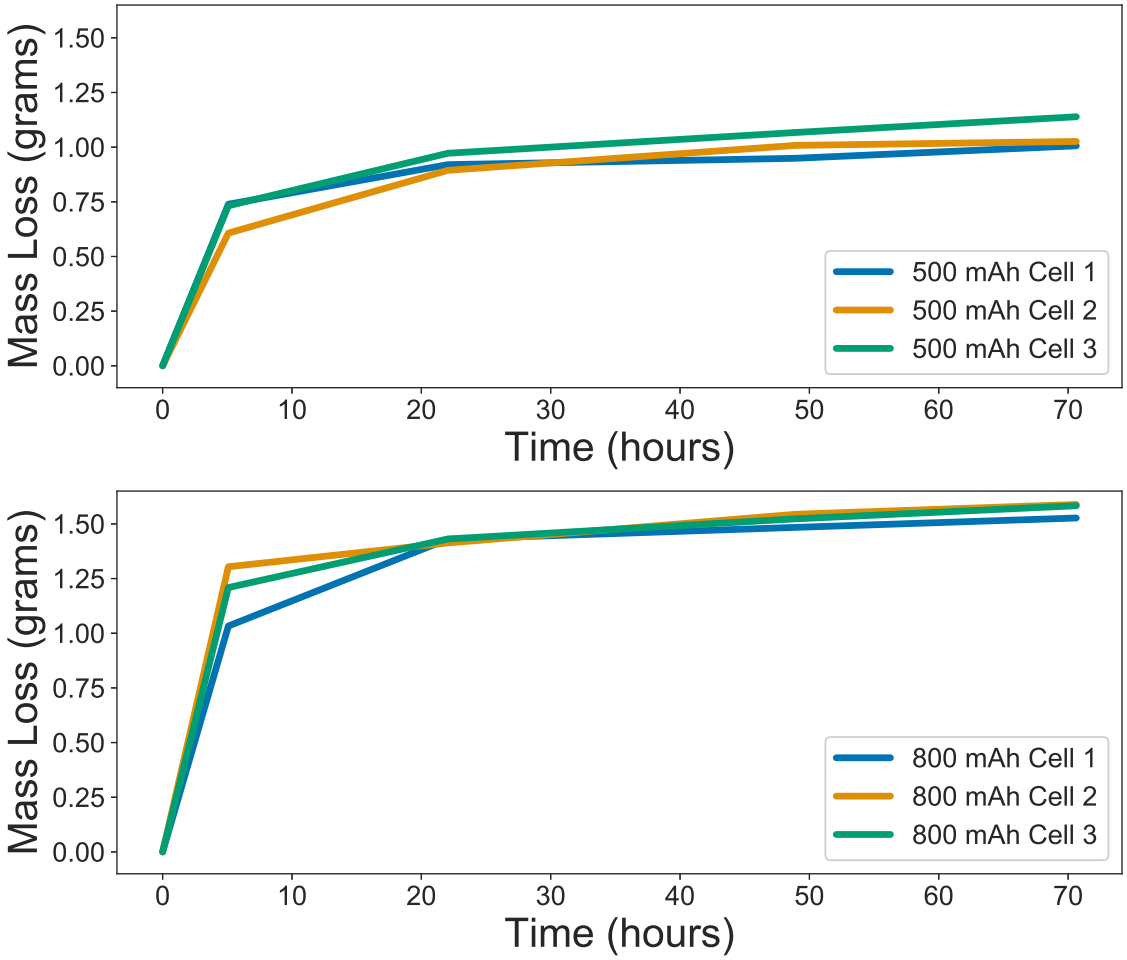

Figure 4.1: Mass Loss of Electrolyte from Dried Pouch Cells

Figure 4.1 above shows the total mass loss for both the 500 mAh and 800 mAh cells over time. The initial average mass of the 500 mAh cells was 10.08 grams and the 800 mAh cells had an initial mass of 16.95 grams. Over the 72 hours of drying, the 500 mAh cells lost an average of 1.06 grams and the 800 mAh cells lost an average of 1.58 grams. Based on the trends, might be a small amount of electrolyte left in the cells. The 800 mAh cells have a slightly steeper slope for the last data points than the 500 mAh cells. With the bigger pouch, more time may have been required to ensure the electrolyte in the cell was completely evaporated. This would need to be further investigated.

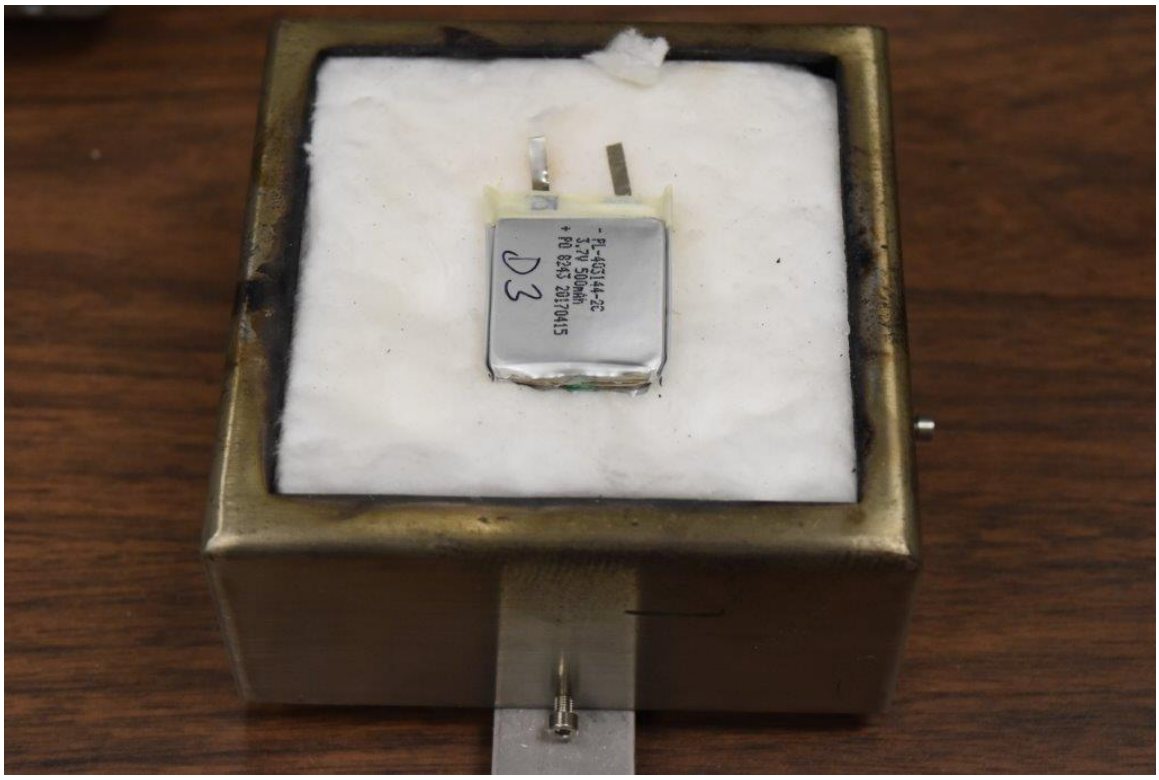

Figure 4.2: Dried Out Cells in Standard Sample Holder

Figure 4.2 above shows a 500 mAh cell that has been cut open and dried for approximately 72 hours. The standard sample holder is used along with kaowool to set the sample at 25.4 mm below the conical heater.

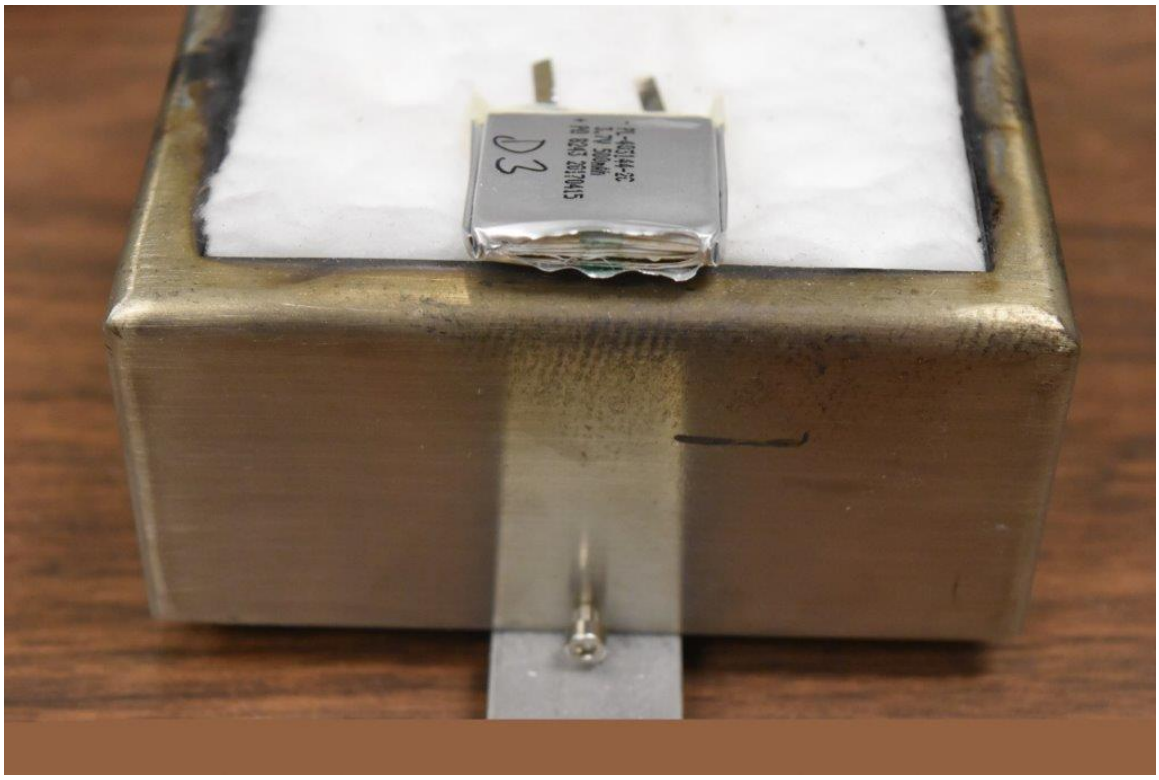

Figure 4.3: Dried Out Cell Cut Edge

Figure 4.3 shows an additional view of the dried-out cell, this time moved such that the cut open end can be seen. The end was frayed or spread open of the pouch after being sliced, along with the green tape holding the separation material together was cut. Once the pouch was sliced open, the end of the razor blade was used to help spread apart as much as possible without causing damage or tears. This step was to help promote additional evaporation of the electrolyte.

The third set of tests consisted of 500 mAh and 800 mAh array tests. The arrays consisted of a total of five pouch cells stacked on top of one another with type K thermocouples placed in between each cell. The size of the thermocouple wire used was 36 gauge. The small size of the thermocouple would affect the contact between each cell the least. This provided the temperature data and determined is used to determine the failure temperature effects between each cell. The test by Larsson et al. (122) performed a similar test in order to gain an understanding of HRR and modeling of a five-pouch cell array. The difference,

as mentioned in the literature review was that a propane burner was set underneath of the array rather than a conical heater set a specified heat flux. The HRR depends on the thermal thickness of the material. A thin material will see a large spike in the HRR whereas a thick material will see more of a steady-state or plateaued HRR (127). This gives the reason between understanding how a single pouch cell which is thin verse an array of cells which is thick might give different characterizations.

For the array tests, a custom ASTM E1354 sample holder was built. This was to help prevent gases and contents from ejecting from the sample tray. The with the potential of venting due to a small rupture in the pouch of the cell, contents could potentially be pushed outside of the air flow and not become entrapped and pulled into the exhaust stream. The height of the sample holder was set to stay below the shudders below the conical heater. Kaowool was used to set the top cell at nominally 1" or 25.4 mm below the base of the conical heater. Stainless steel was used, and the dimensions of the custom sample tray matched the ASTM E1354 sample tray. Vents were added at the bottom to prevent stagnation of fuel within the sample tray since the edges are higher than the standard sample tray. The FAA test by Quintiere et al. (118) modified a sample tray for 18650 cells and provided ventilation holes in a similar matter. The sample tray was sandblasted to prevent reflections of the heat flux from affecting the cells B through E.

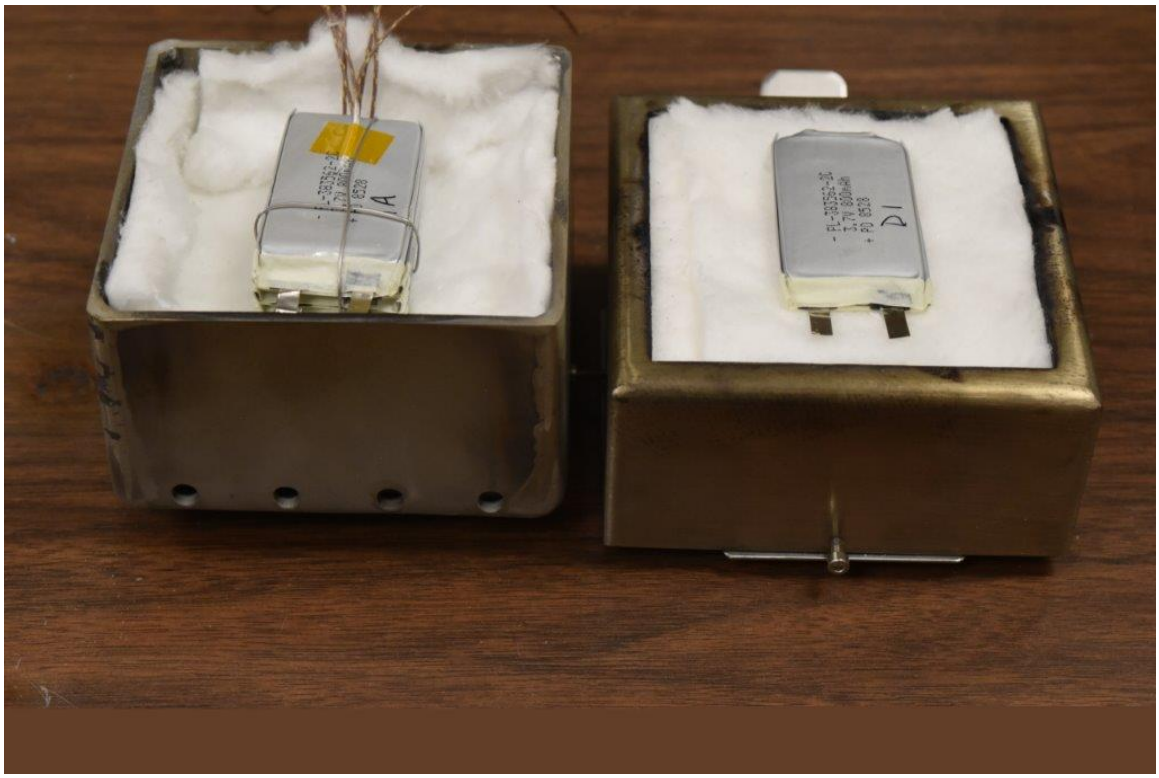

Figure 4.4: Side View of Custom Battery Array Sample Holder

Figure 4.4 shows the side view of the custom sample tray on the left and the standard sample tray on the right. The custom sample tray was fabricated using waterjet cutting and sheet metal bending techniques. The sides of the box were TIG welded together. At the bottom of the custom sample tray, four 0.25" (6.35 mm) holes are just above the crease in the material. All four sides have these ventilation holes.

Figure 4.5: Top View of Custom Battery Array Sample Holder

Figure 4.5 shows the top view of the custom sample tray on the left and the standard sample tray on the right. The dimensions are nominally the same, and as noted above, the custom sample holder is taller than the standard sample holder with the optional shroud.

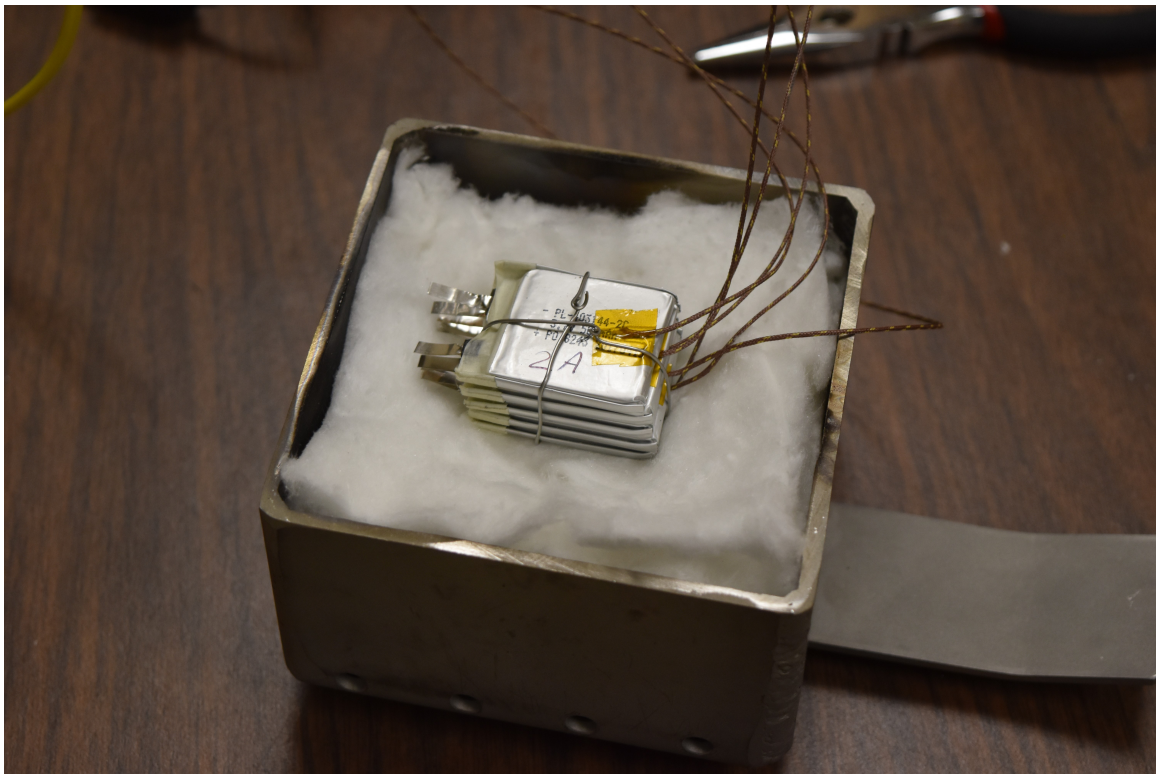

Figure 4.6: Pre-Burn View of 500 mAh Array

Figure 4.6 shows the 500 mAh array prior to testing. Note that the tabs are pointed to the end opposite of the handle and the array is centered in the sample tray. This again is to help ignite the cells with the standard ignitor on the cone calorimeter due to the first off-gassing occurring near the tabs/taped the end of the cells. Two separate sections of safety wire were used, both going underneath and tied together in the center of the cell. One piece along the lateral direction and the other along the longitudinal direction. This is similar to how Larsson et al. fastened pouch arrays together.

Figure 4.7: PMMA Array Test

In addition to battery arrays, an array using 3/16" thick Poly(methyl methacrylate) or PMMA with a metalized moisture resistant polyester film was used to help further characterize the array tests. This metal film has a silver reflective aluminum finish coating and is made from polyester. The array is shown in figure 4.7, with five sheets of PMMA stacked with the polyester film in between.

Figure 4.8: PMMA Array Test with Foil

Figure 4.8 shows how the sample was prepared, with a foil tray around it and the standard sample holder was used. The top of the array was set at nominally 25.4 mm below the conical heater. The intent of this additional test was to help show the effect of a layered medium, characterizing how the PMMA burns with a layer of film in between should show how the different individual samples of PMMA burn over the test period.

4.4 Test Observations

The first set of tests were single cells tests. A total of six samples, three 500 mAh and three 800 mAh, were used at 0% SOC. The cone calorimeter was calibrated, and the conical heater was set at nominally 50 kW/m^2. Once ready, the sample holder and one thin sheet of kaowool would be prepped. Right before starting the test, the cell would be placed on the fresh sheet of kaowool. The thought was that some of the gases ejected from the other cells might absorb into the kaowool, so a fresh top sheet would prevent any leftover

contents from burning in the next test. The sample holder would then be inserted under the conical heater and the igniter would be placed above the tab area of the cell.

Figure 4.9: Burning View of 800 mAh Single Cell Jetting

During testing, it was noted that the single cells at 0% SOC would begin to off-gas around the tab and taped side of the cell. Some swelling would occur in the pouch, followed by a rupture on the end of the cell with the tabs. This would cause some type of jetting effect, where gasses would expel from that end for a short period. This is seen in figure 4.9. It was noted that the jetting was not violent enough to eject any contents or gases that were noticed outside of the airstream pulling into the exhaust hood. This jetting effect was also noted by Ping (121) when testing prismatic cells at 0% SOC.

Figure 4.10: Burning View of 800 mAh Single Cell Post Jetting

Once the jetting effect diminished, the rest of the cell would begin to burn, with the whole pouch at this point burning. This is shown in figure 4.10, with the entire pouch at this point burning and the jetting on the tab end of the cell slowing to a stop.

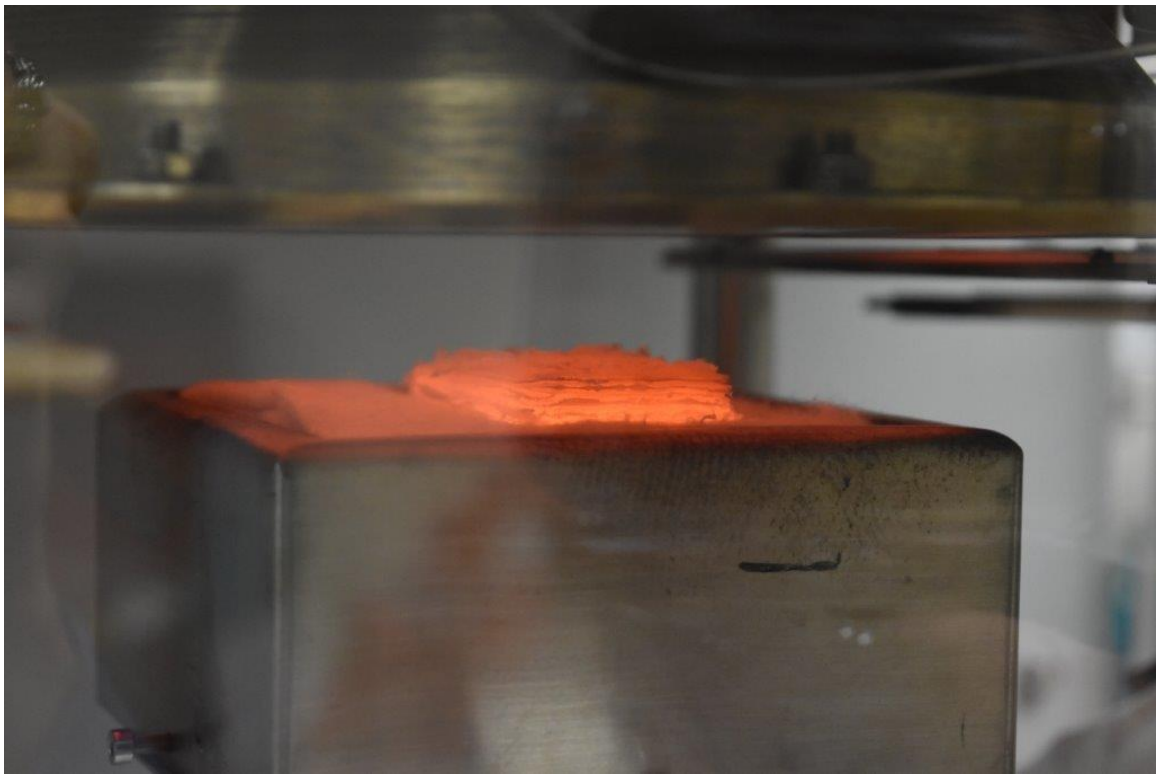

Figure 4.11: Burning View of 800 mAh Single Cell Extinguished

After the flame extinguished, the sample would sit under the conical heater for two minutes before the test ended. It was observed that the remaining components of the cell would begin to swell and glow orange.

The second set of tests were single cells tests. A total of six samples, three 500 mAh and three 800 mAh, were used at 0% SOC and slit open and dried out as shown in figure 4.1.

Figure 4.12: Burning View of 800 mAh Dried Cell

The dried cells burned differently compared to the cells with the electrolyte. While the end with the tabs would be the first point to ignite, the entire pouch would quickly begin burning. No jetting effect was observed with the dried cells. The burning of the dried cells looked like the post-jetting burning effect from the cells with the electrolyte.

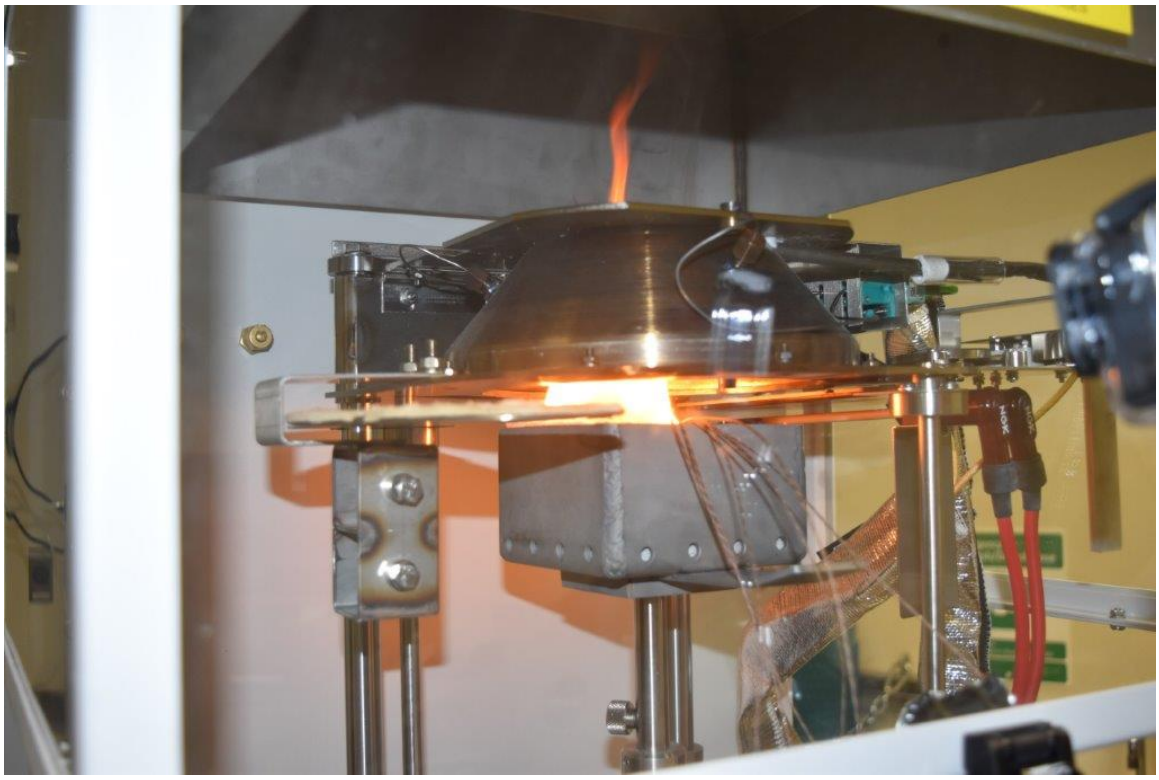

Figure 4.13: Burning View of 500 mAh Array

Figure 4.13 shows the 500 mAh array during the test. As stated previously, the tabs are located on the opposite end of the handle. The thermocouples were held up with safety wire to prevent unnecessary tension, though due to the thermocouple wires, mass data will have a larger uncertainty.

Figure 4.14: Burning View of 800 mAh Array

Figure 4.14 shows a close-up view of the 800 mAh cell array test burning. These tests were like that of the single cells at 0% SOC, with the first cell failing in the same matter. The difference was that the modified sample holder would help deflect the vent gases straight up. With the raised sample holder, it was more difficult to make observations. While the testing was conducted, it was observed with the Graphtec Data Logger that as the thermocouple measuring the temperature of the top surface of any given cell approached 170 °C, the temperature would suddenly be starting elevating quicker. On the third test using the 800 mAh cells, the fire self-extinguished a few seconds after ignition. The cause of this may have been due to vent gasses accumulating inside of the sample holder, causing a rich condition. The ignitor was re-positioned immediately, and ignition reoccurred. Even with the additional ventilation holes along the bottom of the custom sample holder, there may have been some stagnation inside of the box causing this rich condition.

Figure 4.15: PMMA Array Test Burning

The PMMA tests were unique in the sense that there was a time delay between each layer. The first test had a long time to ignition compared to the second and third. The top layer of separation material protected the first piece of PMMA from burning before finally off-gassing and burning. The complete array took roughly twenty minutes from ignition to being extinguished. Five very distinct peaks were shown in the data and can be seen in the results section below.

4.5 Cone Calorimetry Testing Results

In chapter three, various metrics such as lower flammability limit, flame speed, and overpressure were characterized for lithium-ion cells in order to compare with other similar deflagration hazards. To characterize the fire hazard and fuel load of Li-BESS quantitatively, the HRR can be measured compared with other hazards. With the pouch cells used in these tests and other literature have various cross-sectional areas and thicknesses. Analyzing the

HRR with units of kW and kW/m^3 will give the ability to compare results and trends with other pouch cells with different dimensions. Additionally, this will help quantify the fuel load of lithium-ion cells on a volume basis.

The data for times to ignition, flame extinction time, time to peak HRR, the mean HRR, THR along with the mass data will be presented with uncertainty analysis for all tests. With these exploratory experiments to determine the HRR of various cells and arrays, each test had three sets of data collected. This will give a baseline for what should be expected with uncertainty. By using the standard deviation and the student t-value, an uncertainty for these values can be shown.

$$s_{\mathrm{x}}{}^2 = \frac{\sum_{i=1}^{n}(x_i - \bar{x})^2}{(n-1)} \tag{4.5}$$

The standard deviation is calculated for a sample based on equation 4.5 above. Looking up the critical value for the Student's t Distribution based on the significance level, α, and degrees of freedom, ν. Based on standard practice, a confidence interval of 95% will be used. The degrees of freedom is based on ν=n-1, so ν=2. Using the two-tailed test, with ν=2 and α=0.05/2, looking up $t_{1\text{-}\alpha,\nu}$ which a t-value of 4.303 (128). Using this gives a large uncertainty based on the sample size being so small. As part of this exploratory method, additional testing in future work would need to be performed to further understand the uncertainty. Using this, the 95% confidence interval can be calculated from the following:

$$\mu = \bar{x} \pm t_{1\text{-}\alpha,\nu}\frac{s_{\mathrm{x}}}{\sqrt{n}} \tag{4.6}$$

Using equation 4.6, the range of uncertainty with 95% confidence can be estimated for each different measurement and presented. The various tables will include the mean value, standard deviation, and the upper and lower bound ($\pm$) with 95% confidence.

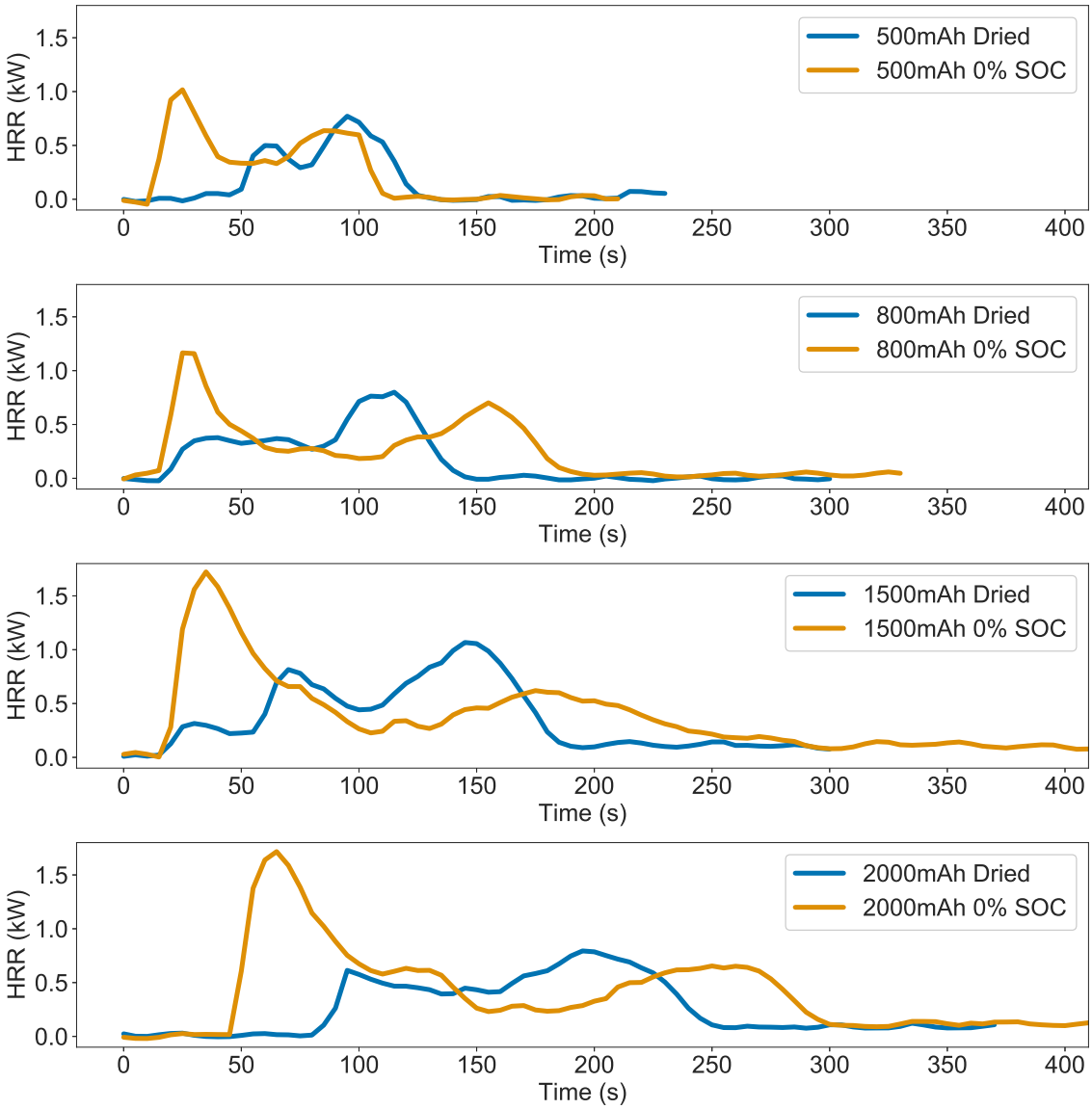

Figure 4.16: Preliminary Single Cell Cone Calorimeter Tests

Figure 4.16 shows the initial HRRs for the various cells tested initially. Note that the 1500 mAh dried cell was damaged during the drying process where a cut in the center of the pouch occurred. It was still burned to characterize how it may have changed and based on the third hump; this might be due to that damage. There is a large peak in the 0% SOC cells followed by one smaller peaked later in the burning process. The dried cells have a smaller initial peak followed by a second peak around the same magnitude as the

second peak on the 0% SOC cells. This was a good baseline to compare various cells and the characteristics are very similar, though also unique compared to other tests in a cone calorimeter.

Figure 4.17: Post-Burn of 800 mAh Single Cell

figure 4.17 shows a single 800 mAh cell after it was removed from the cone calorimeter. It is still glowing at the bottom. What is left is mainly the tabs, cathode and anode materials, with the pouch mostly burned away. The silver flakes on top of the cell are the aluminum material that was used to construct the pouch cell.

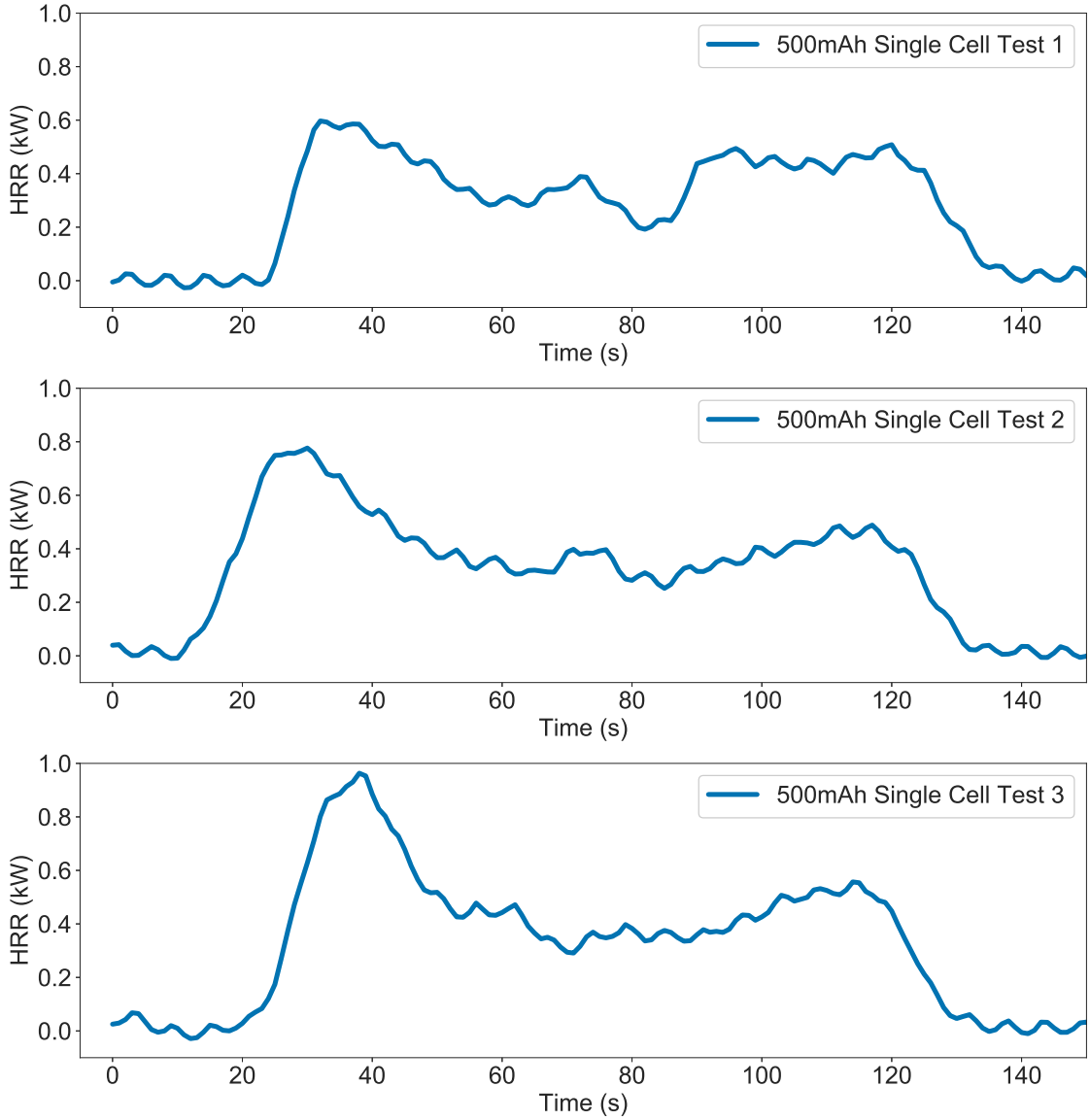

Figure 4.18: HRR Data for 500 mAh Cell Tests

The 500 mAh single cell tests established a general trend where there is a large initial peak after ignition, with a more plateaued HRR followed by one last smaller peak before the flame extinguishes. The small oscillations in the data are based on the area size being much smaller than the typical test sample. This is from the equipment and how it is measuring the HRR.

Table 4.3: Data for 500 mAh Single Cell Tests

	Time to Ignition (s)	Time to Flame Extinction (s)	Time to Peak HRR (s)	Peak HRR (W)	Mean HRR (W)	Total heat Release (kJ)	Initial Mass (g)	Mass Loss (g)
Test 1	26	132	32	597.05	392.78	41.63	10.06	4.03
Test 2	13	130	30	776.53	410.33	48.01	10.08	1.85
Test 3	24	134	38	963.24	449.11	49.40	10.24	2.08
Mean	21	132	33.33	778.94	417.41	46.35	10.13	2.65
Std. Dev.	7.0	2.0	4.2	183.10	28.83	4.14	0.10	1.20
Uncertainty (±)	17	5	10	454.89	71.61	10.29	0.24	2.99

Table 4.3 gives the test ignition time, test time, peak HRR, mean HRR, total energy, and mass loss data for the single cells. The time to the peak HRR is consistent at an average of 33 seconds. Looking at the mean peak release, the third test has a much higher peak heat release, yet the mean HRR is a lot closer when comparing each test. The average total heat release is consistent at 46.35 kJ.

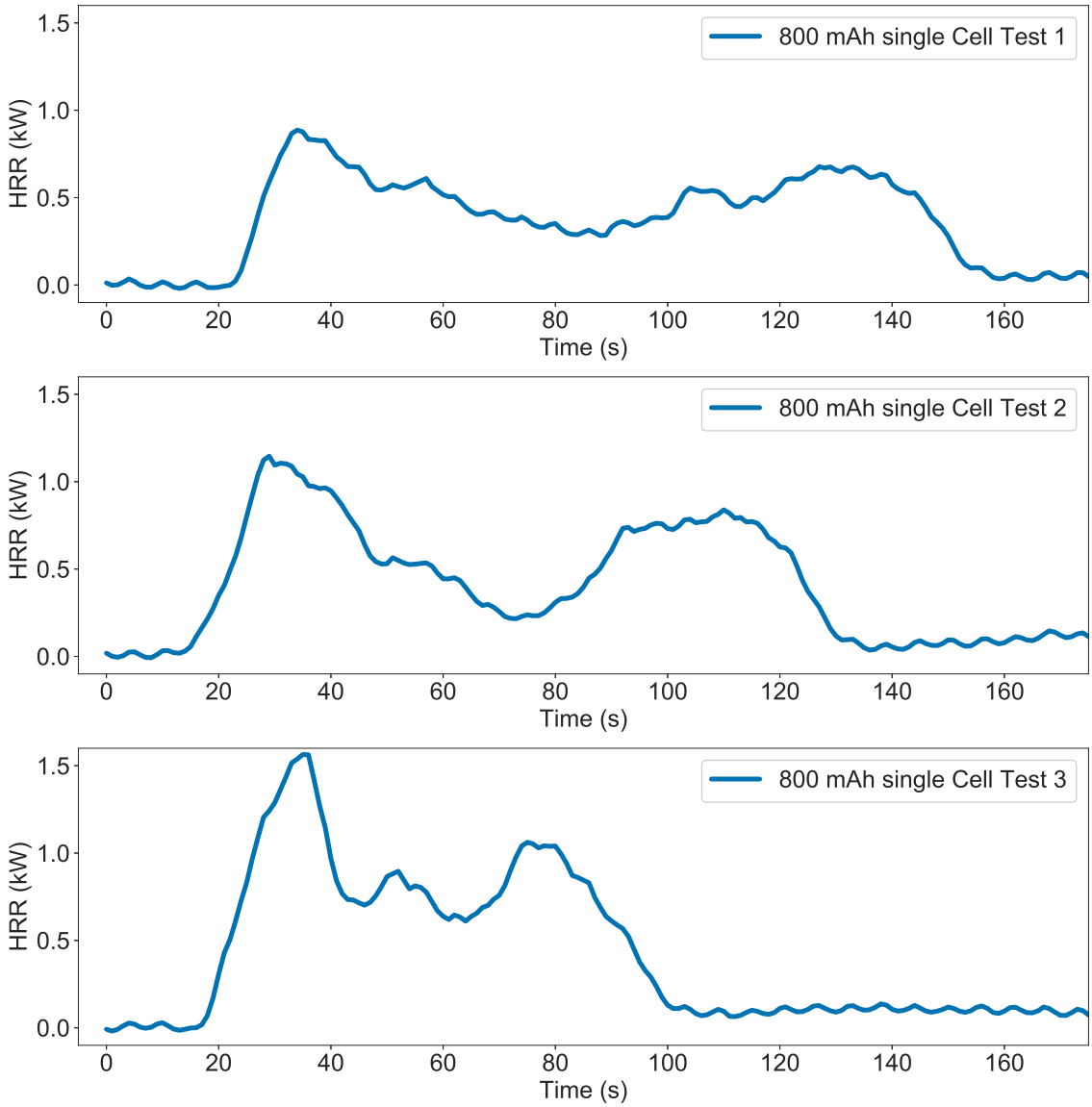

Figure 4.19: HRR Data for 800 mAh Cell Tests

The 800 mAh single cell tests have very similar HRR curves for the first and second test, yet the third test has the same overall shape, put over a shorter time. The first and second peaks are higher than those of the other two tests.

Table 4.4: Data for 800 mAh Single Cell Tests

	Time to Ignition (s)	Time to Flame Extinction (s)	Time to Peak HRR (s)	Peak HRR (W)	Mean HRR (W)	Total heat Release (kJ)	Initial Mass (g)	Mass Loss (g)
Test 1	24	160	34	888.48	484.81	65.93	16.89	3.67
Test 2	14	151	29	1148.01	509.09	69.75	16.92	3.82
Test 3	19	121	35	1567.34	675.80	68.93	16.94	5.16
Mean	19	144	33	1201.28	556.57	68.20	16.92	4.22
Std. Dev.	5	20	3	342.55	103.97	2.01	0.03	0.82
Uncertainty (±)	12	51	8	851.01	258.29	4.99	0.07	2.04

As shown in table 4.4, the third test has a peak HRR of 1567.34 W, much higher than test one and two. The time to the peak HRR is very close among each cell, at 33 seconds. Even with the higher peaks, all three tests have very close overall total heat release, with an average of 68.2 kJ.

Looking at the literature of similar tests, the paper by Somandepalli et al. (117) has very similar results for pouch cells at 0% SOC. There is an initial peak after ignition followed by a small peak before extinguishing. Observing their post-burn images shows more of a roll or folded up type cell construction, whereas the cells used in these experiments appear to be stacked rather than folded.

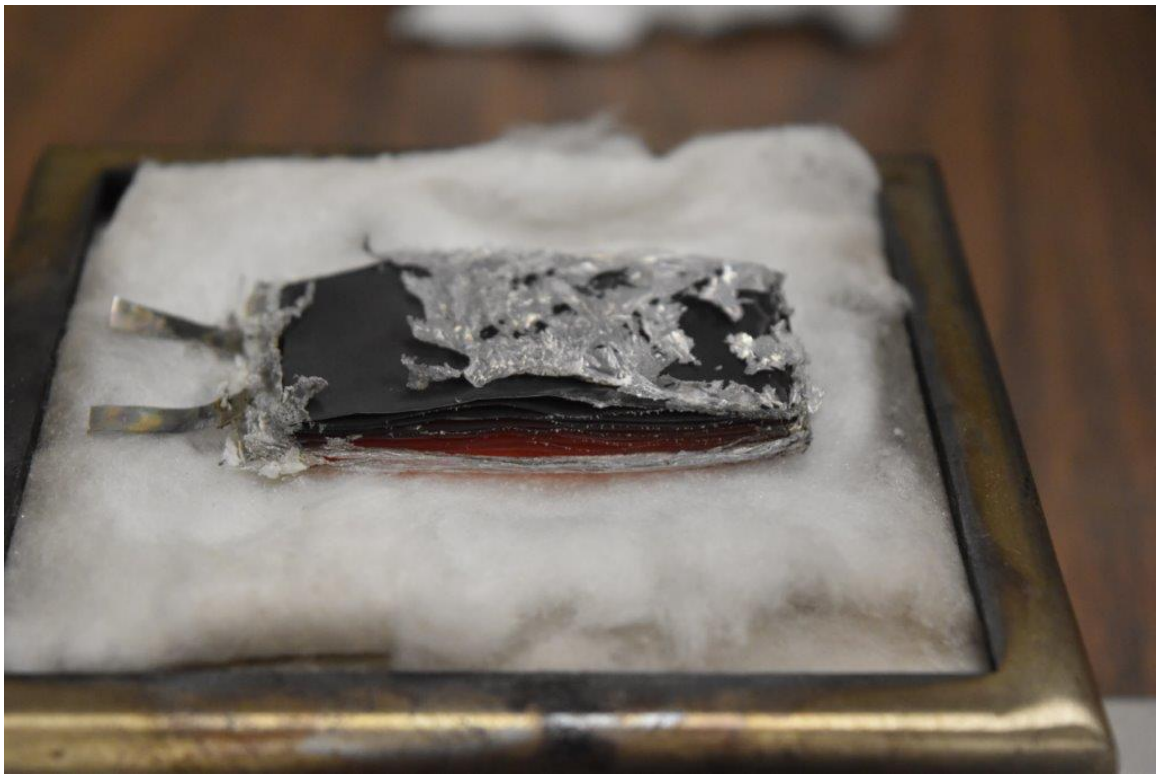

Figure 4.20: Post-Burn of 800 mAh Dried Cell

The next set of tests discussed will be the dried-out cells. Figure 4.20 is a dried out 800 mAh cell after it was removed from the cone calorimeter. The post-burning images are very similar to the 0% SOC cell as shown in figure 4.17, yet the data is a lot different.

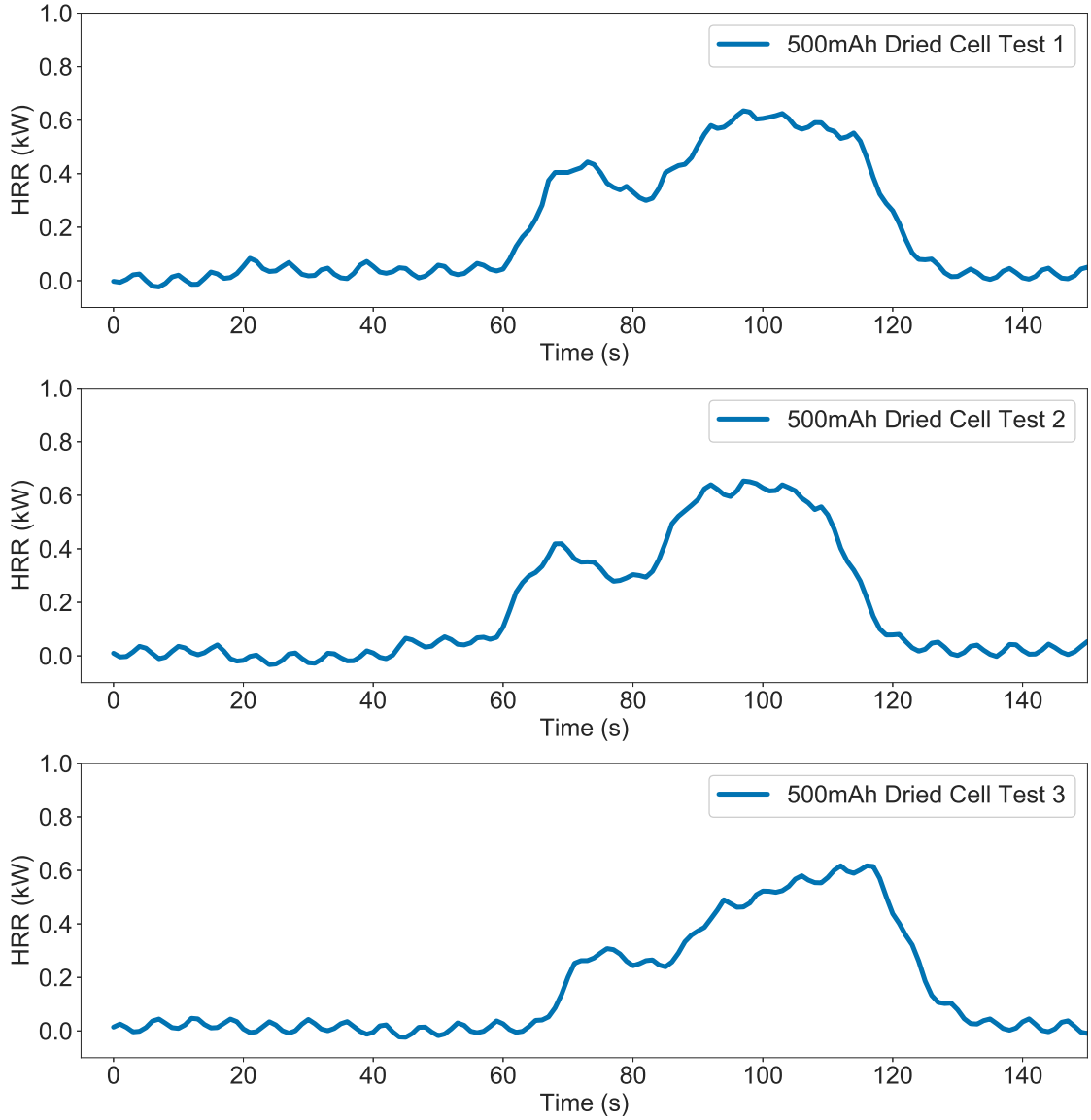

Figure 4.21: HRR Data for 500 mAh Dried Cell Tests

The 500 mAh dried cells have a much different overall trend than that of the 0% SOC cells. Rather than the major peak initially happening, there is one small peak, followed by a larger peak before the flame extinguished. All three tests have very similar trends with no large difference between them.

Table 4.5: Data for 500 mAh Dried Cell Tests

	Time to Ignition (s)	Time to Flame Extinction (s)	Time to Peak HRR (s)	Peak HRR (W)	Mean HRR (W)	Total heat Release (kJ)	Initial Mass (g)	Mass Loss (g)
Test 1	62	134	97	635.05	382.36	27.53	9.04	0.97
Test 2	60	135	97	653.26	346.15	25.96	9.00	0.83
Test 3	67	141	112	617.11	328.65	24.32	9.04	0.88
Mean	63	137	102	635.14	352.39	25.94	9.02	0.89
Std. Dev.	4	4	9	18.07	27.40	1.61	0.02	0.07
Uncertainty (±)	9	9	22	44.90	68.06	3.99	0.06	0.18

The time for the peak HRR is 102 seconds. Total test times are also very close, with an ignition time of 63 seconds and standard deviation of 4 seconds and a time to extinguished of 137 with a standard deviation of 4 seconds. The peak HRR are also very close at 635.14 W with a standard.

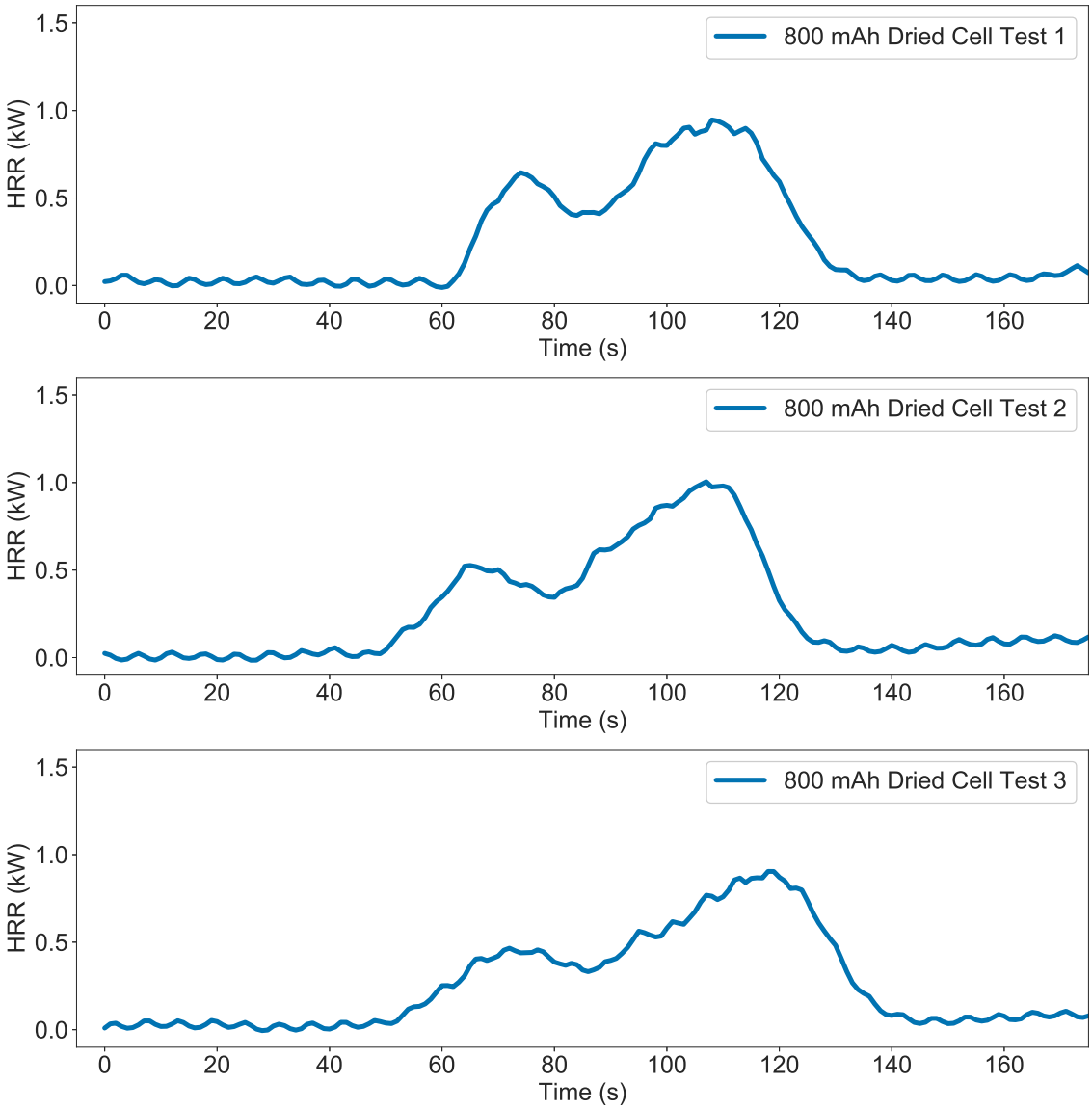

Figure 4.22: HRR Data for 800 mAh Dried Cell Tests

As with the 500 mAh dried cells, the 800 mAh dried cells also have a similar small peak followed by a large peak trend. The main difference noticed is that the first test has a maximum HRR for the first peak that is higher than the other two tests. The first peak in test one could be due to electrolyte still in the cell burning before the plastics making up the pouch burns.

Table 4.6: Data for 800 mAh Dried Cell Tests

	Time to Ignition (s)	Time to Flame Extinction (s)	Time to Peak HRR (s)	Peak HRR (W)	Mean HRR (W)	Total heat Release (kJ)	Initial Mass (g)	Mass Loss (g)
Test 1	50	143	107	1006.62	450.27	41.87	15.30	3.08
Test 2	64	144	108	948.36	493.23	39.46	15.45	1.62
Test 3	52	151	118	905.87	434.61	43.03	15.41	2.08
Mean	55	146	111	953.62	459.37	41.45	15.39	2.26
Std. Dev.	8	4	6	50.58	30.35	1.82	0.08	0.75
Uncertainty (±)	19	11	15	125.66	75.41	4.52	0.19	1.86

The time for the peak HRR is 111 seconds with a standard deviation of 6 seconds. Total test times are also very close, with an ignition time of 55 seconds and a standard deviation of 8 seconds and a time to extinguished of 146 with a standard deviation of 4 seconds. The total heat release is very close, with an average of 41.45 kJ.

Compared with the 0% SOC tests, the dried-out cells seem to be a lot more repeatable and have a lower overall deviation. The initial peak on the dried cells could be from a small amount of electrolyte remaining within the cell even after the drying process. With the jetting discussed earlier, this could have caused the variations in the HRR. The overall THR is very repeatable for all the tests so far. The HRR is less repeatable from test to test. This shows how much the lithium-ion cells have variations from cell to cell. By using the dry cell data and data at 0% SOC, comparison of the effect of the electrolyte can be determined. Additionally, the heat of combustion for the electrolyte can be estimated based on the difference in THR and the dried cell mass loss data.

The mass loss data is also an example of why more tests should be performed to better understand if some of the tests are outliers and why. Also, the load cell has a range of 0 to 275 grams, with the burning mass is less than 10 grams, might cause additional uncertainty. Additionally, this motivated the need to test cell arrays. The effect from individual cell variations should be reduced and have less of an effect when in a multi-cell array.

The next set of tests are the array tests. These involved five cells stacked inside of the custom sample holder with thermocouples on each surface of each cell. Figure 4.24 should be referred to for the thermocouple locations.

Figure 4.23: Post-Burn of 500 mAh Array

Figure 4.23 above shows the 500 mAh array test after the test was completed and it was removed from the cone calorimeter. The cells remained intact with the safety wire wrapped around them. It should be noted even the bottom cell is glowing, showing propagation through the whole array.

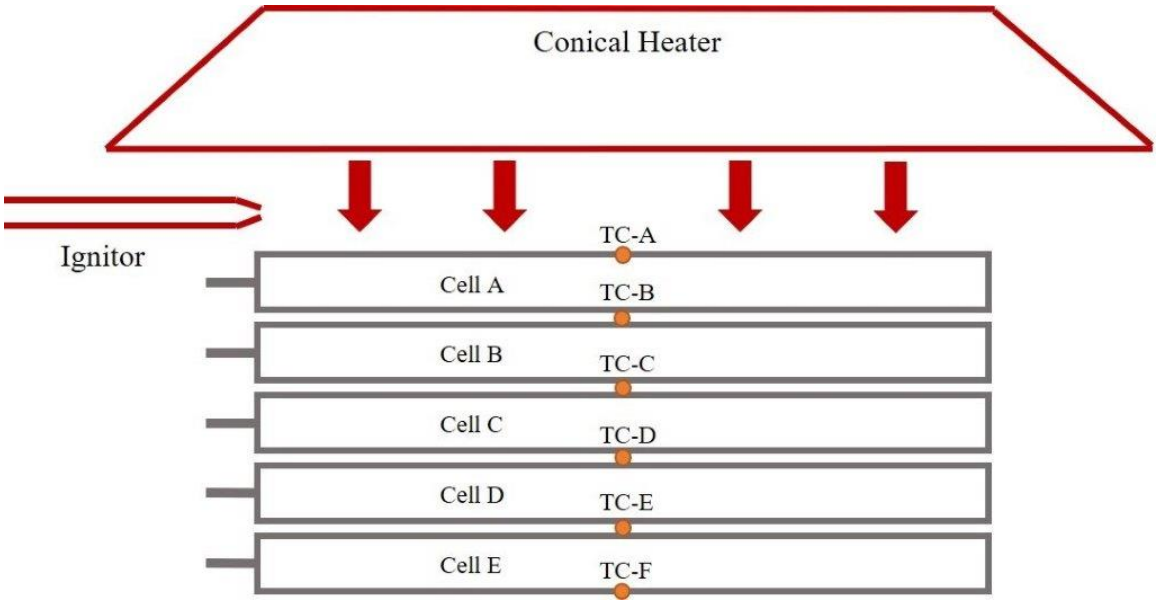

Figure 4.24: Five Cell Array Setup

Figure 4.24 above shows a diagram for how the array test was set up. Cells A-E were stacked, and safety wired together.

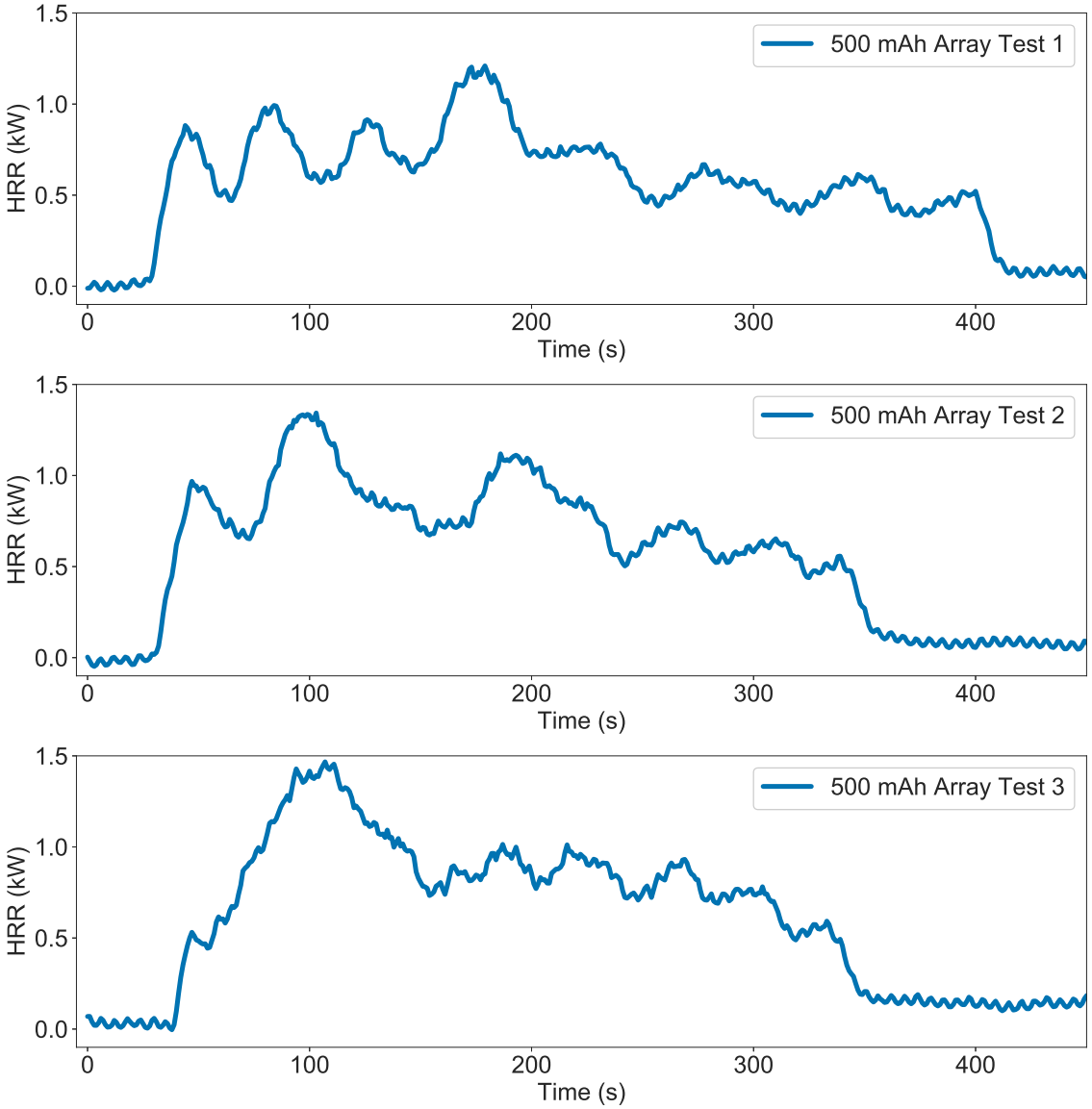

Figure 4.25: HRR Data for 500 mAh Array Tests

Unlike the single cell tests, the array tests are a lot more interesting and less predictable as shown in figure 4.25. The first test has eight very distinct peaks through the test. The second test had a total of six distinct peaks, though the second and third are a lot wider than the others. The third test has six distinct peaks, with the first peak being significantly larger than the others. The larger peaks on the second and third test have similar magnitudes and the last three to four peaks have very similar magnitudes and

shapes. The last three to four peaks prior to extinguishing have very similar characteristics and magnitudes.

Table 4.7: Data for 500 mAh Array Tests

	Time to Ignition (s)	**Time to Flame Extinction (s)**	**Time to Peak HRR (s)**	**Peak HRR (W)**	**Mean HRR (W)**	**Total heat Release (kJ)**
Test 1	29	428	179	1209.71	628.04	250.59
Test 2	35	354	103	1343.34	772.87	246.55
Test 3	41	349	107	1467.28	849.46	261.63
Mean	35	377	130	1340.11	750.12	252.92
Std. Dev.	6	44	43	128.82	112.45	7.81
Uncertainty ($\pm$)	15	110	106	320.02	279.35	19.40

With the first array tests, the deviations are a lot higher than that of the single cells tests as seen in table 4.7. Yet the total heat release has an average of 252.92 kJ. Taking the average of the heat release and dividing it by five gives a value of 50.58 kJ compared to the 46.35 kJ for the average single 500 mAh cell heat release. This shows that all five cells were completely burned when comparing with the single cell tests. The ignition time is on average 35 seconds compared to the 21 seconds it took for the single cells tests, this could be due to the thickness of the array effecting this.

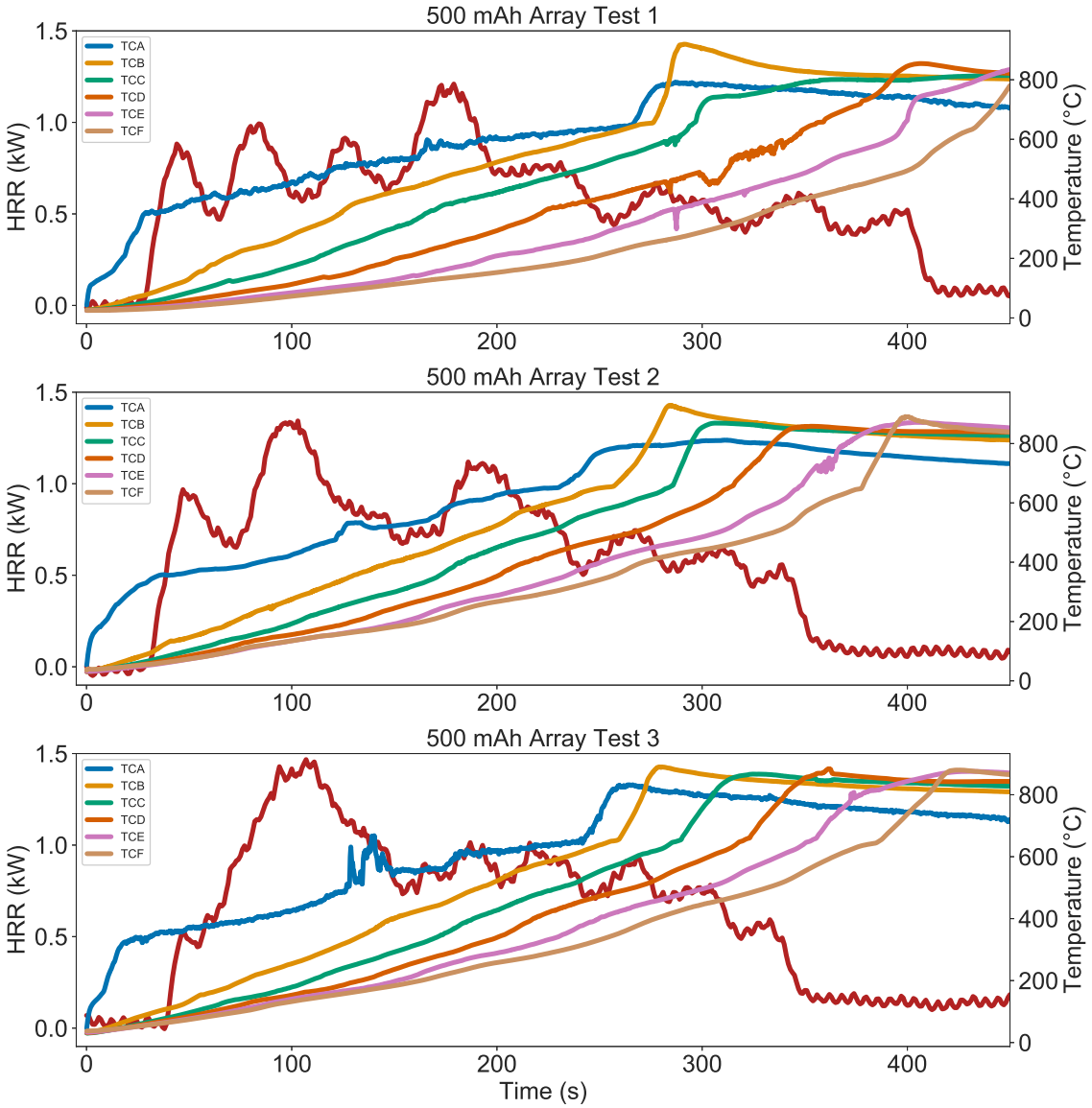

Figure 4.26: HRR Data for 500 mAh Array with Temperature Data

The temperature profiles in figure 4.26 are very similar. Thermocouple A has a temperature of about 350 °C when ignition occurs. This is relatively consistent with all the tests. From there, the temperatures all gradually rise with various slopes to about 650 °C where they suddenly ramp up to 850 °C, after the sample is completely burnt.

Figure 4.27: Post-Burn of 800 mAh Array

Figure 4.27 above shows the 800 mAh array test after the test was completed and it was removed from the cone calorimeter. Like the 500 mAh arrays, the cells stay intact, and all the cells appear glowing the same.

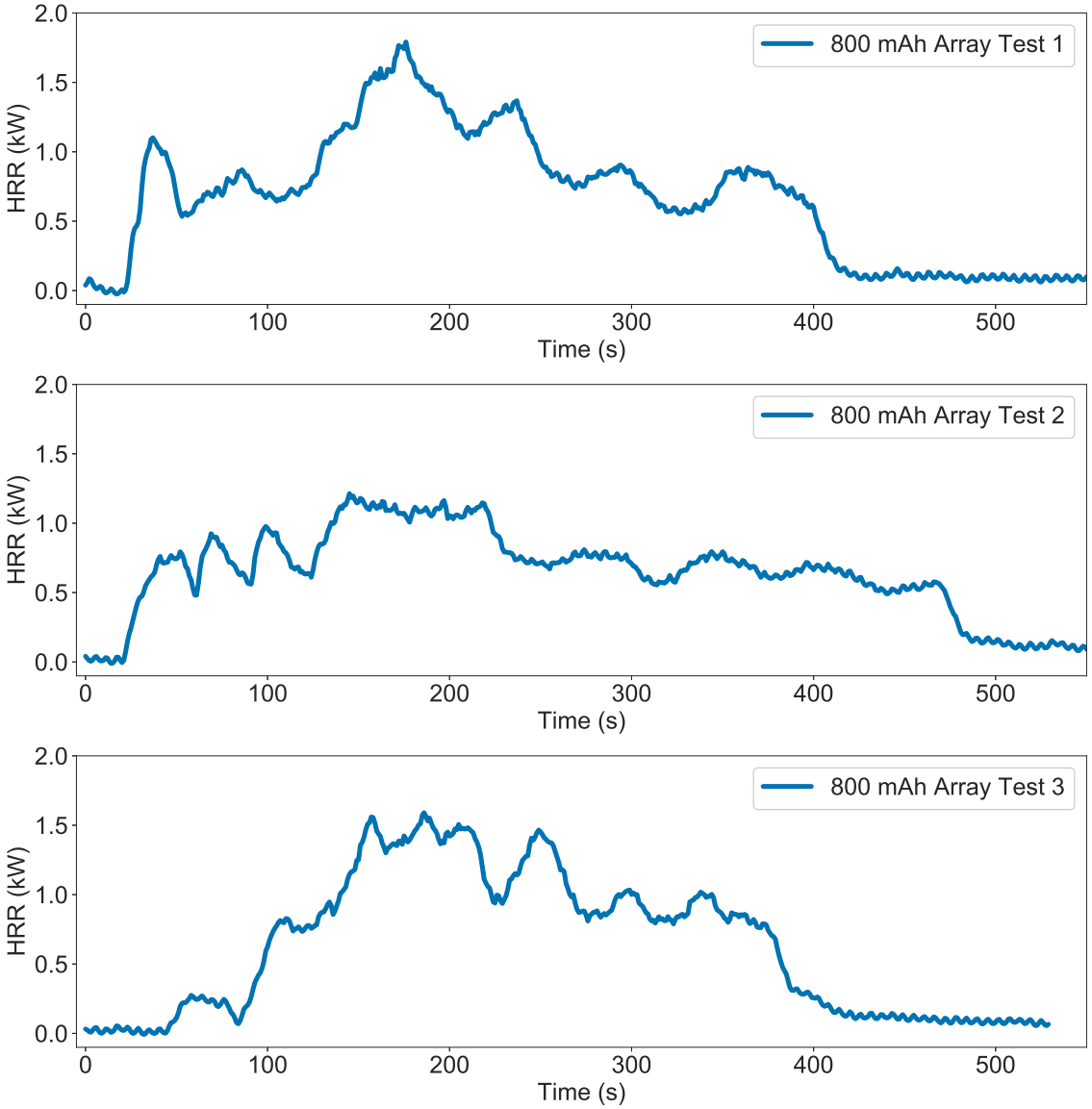

Figure 4.28: HRR Data for 800 mAh Array Tests

Figure 4.28 gives the HRR curves for the 800 mAh arrays. Like the 500 mAh arrays, these are a lot more complex than that of the single cell tests. The first test has six distinct peaks, with one very large peak at 180 seconds or so. Test two has eight different peaks, with one large test at about 150 seconds. The third test has six peaks, with one large peak at about 180 seconds. It should be noted the small peak very close to the initial time of ignition was due to the flame extinguishing just after initial ignition, where the igniter was

used to reignite the cells. This again as previously mentioned may have been due to the venting of the cells causing a rich mixture inside of the custom sample holder causing the flame to extinguish. The final peaks in all the tests have very similar characteristics, with the first and third tests having final peaks that are shaped nearly identically.

Table 4.8: Data for 800 mAh Array Tests

	Time to Ignition (s)	**Time to Flame Extinction (s)**	**Time to Peak HRR (s)**	**Peak HRR (W)**	**Mean HRR (W)**	**Total heat Release (kJ)**
Test 1	23	441	176	1791.21	858.30	358.77
Test 2	24	562	145	1213.46	663.42	356.92
Test 3	45	423	186	1590.49	853.05	322.45
Mean	31	475	169	1531.72	791.59	346.05
Std. Dev.	12	76	21	293.32	111.03	20.45
Uncertainty (±)	31	188	53	728.72	275.84	50.82

Shown in table 4.8 gives an average heat release of 346.05 kJ. The same approach as with the 500 mAh arrays, taking the THR over five gives 69.21 kJ compared with the average heat release of 68.20 kJ from the single cell data. The average ignition time and time to extinguish for the single 800 mAh cells is 19 seconds and 144 seconds, 31 seconds and 475 seconds for the array.

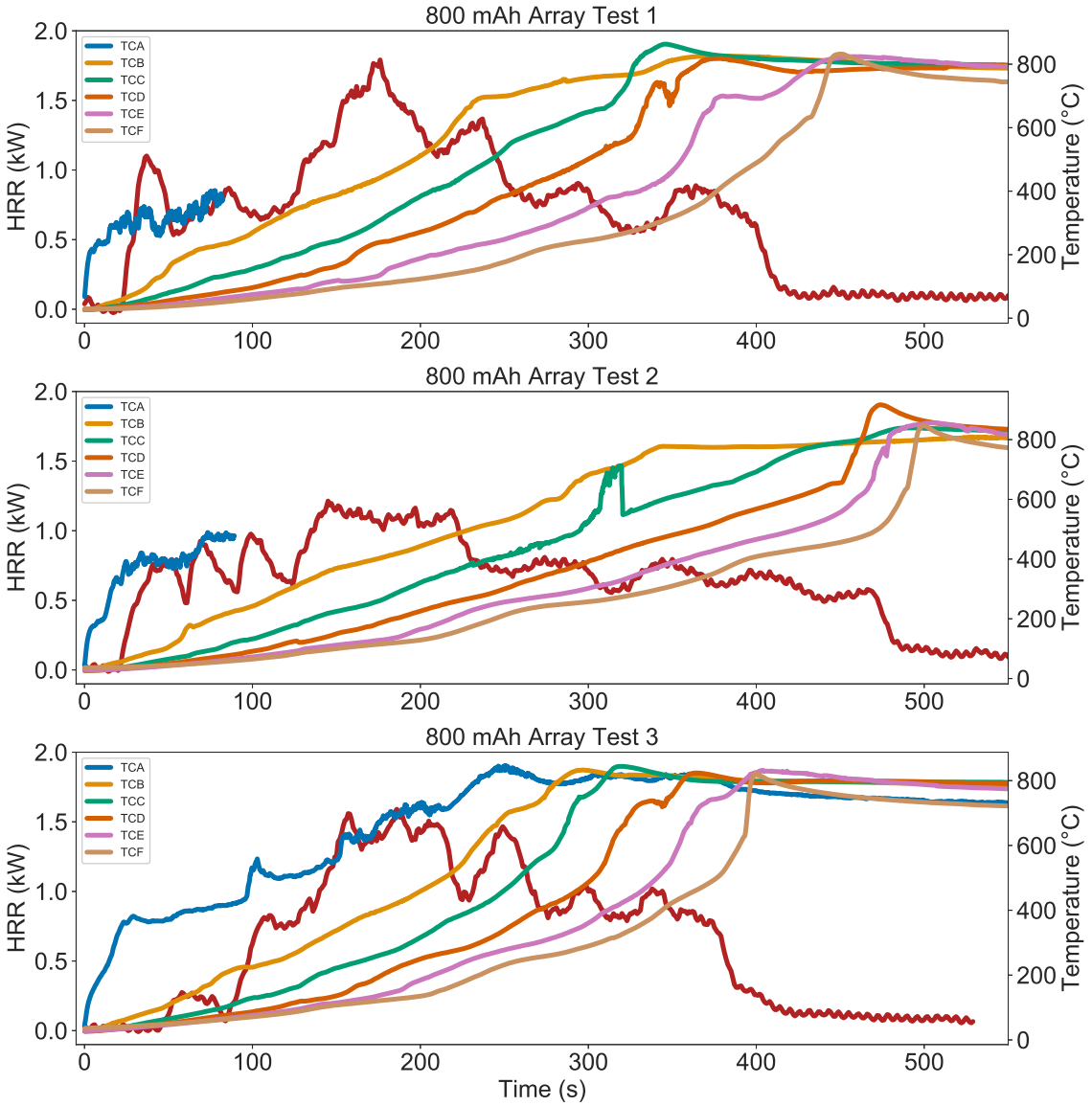

Figure 4.29: HRR Data for 800 mAh Array with Temperature Data

The temperature data for the 800 mAh cells as shown in figure 4.29 gives similar temperature profiles to that of the 500 mAh cells. During test one and two, the thermocouple on the top cell was detached. This caused the readings to be of the gases only and was removed in the figure above once this occurred. The other thermocouples had a similar general trend as with the 500 mAh arrays, with a rising slope to about 500 °C then a sudden jump up as the flame extinguished once the thermocouple F reached 800 °C.

Comparing to the literature, the paper by Larsson at al. (122) gives an example of a 0% SOC five cell array burning. The effects are almost mirrored, with the smaller peaks in the first half of the HRR and the larger peaks coming prior to the flame extinguishing.

Figure 4.30: PMMA Array Test Post Burn

The final set of tests consisted of the five stacked arrays of PMMA samples with metalized moisture resistant polyester film in between each face. Even with the film in between each sample, each of the samples still completely burned, as evident in figure 4.30. Additional photos of the testing will be placed in Appendix B.

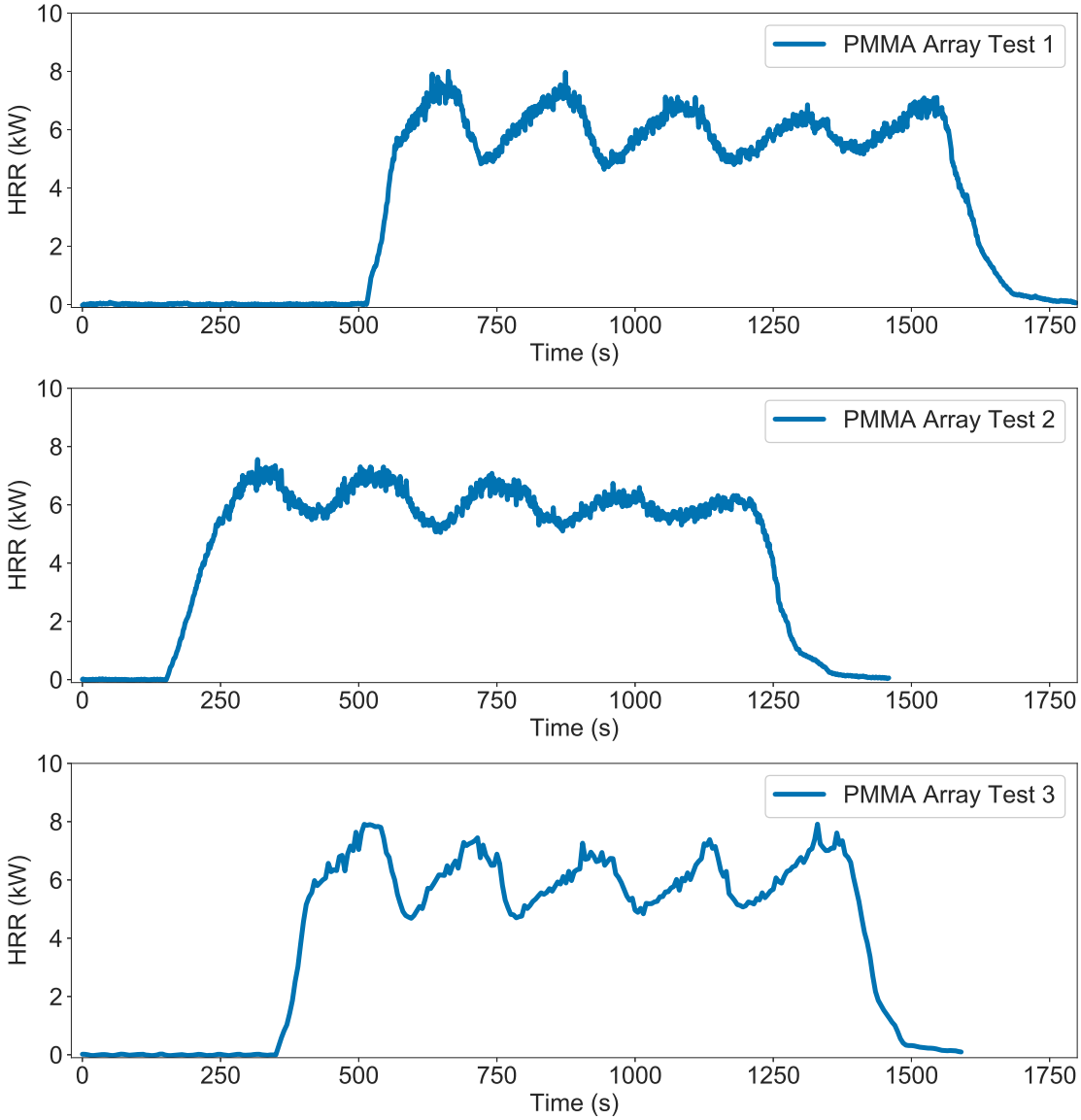

Figure 4.31: HRR Data for PMMA Array Tests

The figure above, 4.31, shows how the PMMA array burns with the film in between each piece. Test one and three have very similar peaks and dips with the same 6 to 8 kW range. the second test is almost more dampened out when comparing with the other two tests.

Table 4.9: Data for PMMA Array Tests

	Time to Ignition (s)	Time to Flame Extinction (s)	Time to Peak HRR (s)	Peak HRR (W)	Mean HRR (W)	Total heat Release (kJ)	Initial Mass (g)	Mass Loss (g)
Test 1	517	1687	662	7945.91	5548.79	6492.09	267.85	269.81
Test 2	155	1354	317	7555.62	5415.75	6493.49	267.22	269.42
Test 3	352	1490	1330	7914.52	5692.79	6462.01	264.25	266.40
Mean	341	1510	770	7805.35	5552.44	6482.53	266.44	268.55
Std. Dev.	181	167	515	216.84	138.55	17.78	1.92	1.87
Uncertainty (±)	450	416	1279	538.70	344.22	44.17	4.78	4.63

Table 4.9 gives the overall data for the PMMA arrays. The peak HRR average is 7805.35 W and the mean HRR is 5552.44 W and an average total heat release of 6482.53 kJ. The mass data shows there is an error between the scale used to measure the total mass compared to the load cell on the cone calorimeter.

Table 4.10: Single Cell Total Heat Release Data

Single Cell Test Data	Test #	Array Total Heat Release (kJ)	Average Total Heat Release (kJ)	Five Times the Average (kJ)
500 mAh Dried	1	27.53	25.94	129.69
	2	25.96		
	3	24.32		
800 mAh Dried	1	41.87	41.45	207.27
	2	39.46		
	3	43.03		
500 mAh 0% SOC	1	41.63	46.35	231.74
	2	48.01		
	3	49.40		
800 mAh 0% SOC	1	65.93	68.20	341.02
	2	69.75		
	3	68.93		

Table 4.10 shows the data for the total heat release for the single cell tests and five times the total heat release. This should help determine if the individual cell data matches with the array tests.

Table 4.11: Array Test Total Heat Release Data

Single Cell Test Data	Test #	Array Total Heat Release (kJ)	Average Total Heat Release (kJ)	One Fifth the Average (kJ)
500 mAh Array	1	250.59	252.92	50.58
	2	246.55		
	3	261.63		
800 mAh Array	1	358.77	346.05	69.21
	2	356.92		
	3	322.45		
PMMA Array	1	6492.09	6482.53	1296.51
	2	6493.49		
	3	6462.01		

As mentioned before, comparing one-fifth of the total heat release in table 4.11, the 500 mAh array gives 50.58 kJ compared to 46.35 kJ for the single cell average. The 800 mAh array gives a value of 69.21 kJ compared to 68.20 kJ for the single cells shown in table 4.10. Both the 500 mAh and 800 mAh data aligns showing that both arrays were completely burned.

In order to further quantify the results from the lithium-ion cells, numerical integration was used to compute the THR over time. The results can be found below in figures 4.32 and 4.33. Based on the tables above, all five cells did burn when comparing the THR with the array to the THR of the single cells. Unlike the PMMA array test with five distinct peaks, the pouch cells have varying peaks and trends. This could be due to the different materials throughout the cell burning at different rates, causing some of the variations in peaks. This causes the burning of each cell to overlap, unlike the PMMA array which distinctly would have the top piece burn before the next.

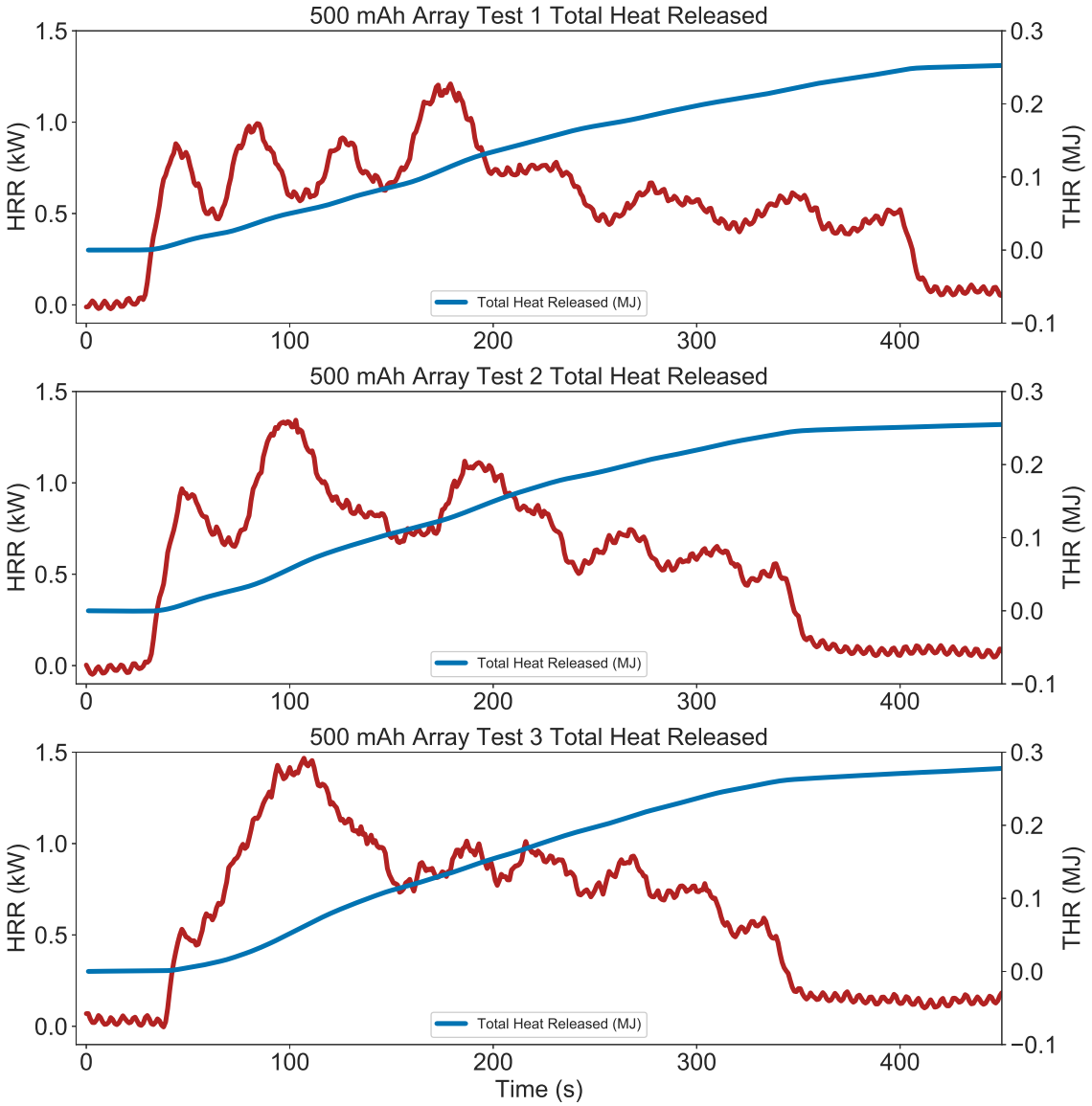

Figure 4.32: Total Heat Release Over Time 500 mAh Array

Looking at the THR in figure 4.32 shows very linear trends directly after ignition. As the array extinguishes, the THR begins to plateau, an indication that the sample is completely burnt. This shows as the HRR drops down and plateaus at the same time as the THR. Based on table 4.11, the average THR for a single 500 mAh cell is 46.35 kJ. Taking this into account, the table below shows the times that the THR for the array equals one, two, three, four and all five cells.

Table 4.12: Total Heat Released Data for 500 mAh Array

	One Fifth of the Total Heat Released (kJ)	1/5 of Total Heat Released (s)	2/5 of Total Heat Released (s)	3/5 of Total Heat Released (s)	4/5 of Total Heat Released (s)	Total Heat Released for Array (s)
Test 1	50.118	100	167	221	305	422
Test 2	49.309	94	141	199	263	352
Test 3	52.327	100	143	203	265	343
Average	50.585	98	150	208	278	372
Std. Dev.	1.562	3	14	12	24	43

Table 4.12 shows the time it takes for the THR to equal fifth increments of the total array heat release. This shows how long each array took to burn each battery. The 500 mAh cells burnt about 111 seconds on average from ignition to extinguishing. It only takes an average of 63 seconds to get to $1/5^{\text{th}}$ of the THR, or approximately one battery. With perhaps the second battery starting to burn the reason behind the array having a quicker time to a single cell this shows some of the reason behind the HRR data being so different between tests for the first 200 seconds or so. Then it takes an additional 52 and 58 seconds to achieve $2/5^{\text{th}}$ and $3/5^{\text{th}}$ of the THR. To reach $4/5^{\text{th}}$ and the complete burn of the array, it takes an average of 70 and 94 seconds longer. This all sums up to an average of 335 seconds from ignition to being extinguished to burn the complete array using an average ignition time of 35 seconds. The single cell takes 111 seconds, with the array test using 500 mAh cells taking three times as long. The cells are not burning individually like the PMMA, but rather they are burning at a quicker rate, with various materials within the cell such as the electrolyte burning quickly as seen in the first 200 seconds, then more distinct and repeatable components burning, shown in the last half of the HRR curves.

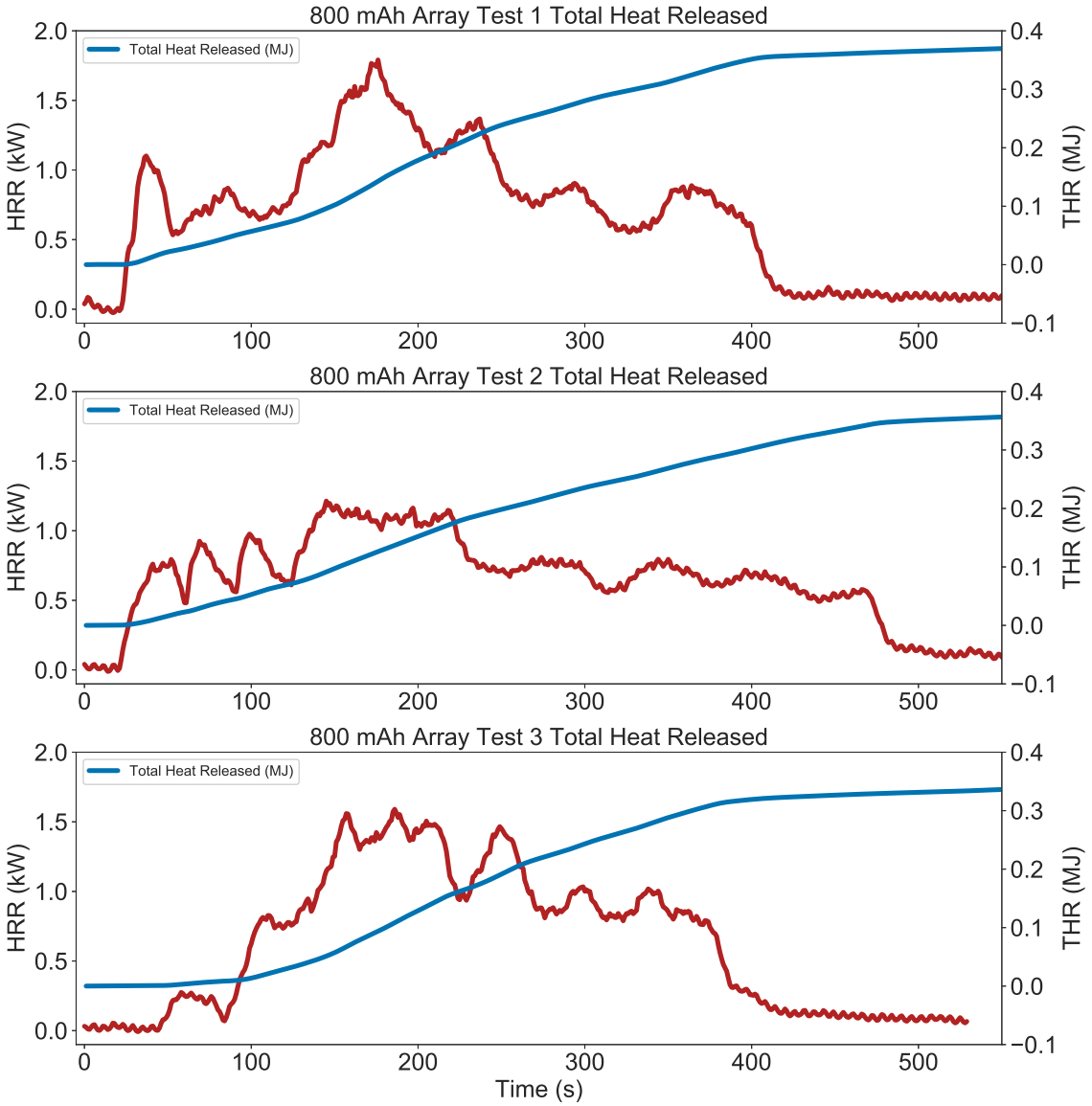

Figure 4.33: Total Heat Release Over Time 800 mAh Array

A similar comparison can be made with the 800 mAh array test. Figure 4.33 above gives the same linear trend for the THR over time as the 500 mAh array did. Again, as expected, when the sample is extinguished, the THR and the HRR both plateau.

Table 4.13: Total Heat Released Data for 800 mAh Array

	One Fifth of the Total Heat Released (kJ)	1/5 of Total Heat Released (s)	2/5 of Total Heat Released (s)	3/5 of Total Heat Released (s)	4/5 of Total Heat Released (s)	Total Heat Released for Array (s)
Test 1	71.754	121	176	231	309	434
Test 2	71.384	124	192	271	376	552
Test 3	64.490	155	200	251	316	414
Average	69.209	133	189	251	334	467
Std. Dev.	4.091	19	12	20	37	75

It takes an average time of 31 seconds for the 800 mAh arrays to ignite. Table 4.13 gives an average time to reach $1/5^{\text{th}}$ of the THR at 133 seconds or 102 seconds after ignition, compared to 125 seconds from ignition for a single 800 mAh cell to extinguish. It then takes 56 and 62 more seconds to reach $2/5^{\text{th}}$ and $3/5^{\text{th}}$ of the THR. To reach $4/5^{\text{th}}$ and the THR in the array test it takes an additional 83 and 133 seconds. Like the 500 mAh array test, to reach the last $2/5^{\text{th}}$ of the THR, it takes a lot more time than the first $3/5^{\text{th}}$ of the THR. This again shows how unlike separated medians of the same material; the cells are a lot more complex in terms of how they burn and what the effect of an array burning compared to single cell data is.

4.5.1 Discussion of Results

The single cell tests were overall repeatable, with some differences on the magnitudes of the first peak for the HRR. The dried-out cells were a lot more repeatable, with the HRR plots having very similar peaks in terms of shape and magnitude when comparing both the 500 mAh and 800 mAh cells. The array tests can be explained when first looking at the PMMA arrays. The tests showed that with an interface in between the layers of PMMA, there is a dampening effect as the top layer burns prior to the next layer. With the pouch cells, there are more materials used with the casing, cathode, anode, separator, and electrolyte. Once the PMMA array burns through the separating material, it burns like a single PMMA material. The peak HRR per area is an average of 780.54 kW/m^2. Looking at the results from Lindholm at al. (115) gives a peak of about 900 kW/m^2 and has a similar HRR curve for samples with various thickness values. The lower peak HRR could be due to heat flux, variations in samples, or a dampening effect from the separating material. The lithium-ion cells have more layers and variations in how each material burns.

This is apparent from the single cells tests that each has two peaks in the HRR curve, in contrast to the one single peak a material such as PMMA has. The cells are layered, with a pouch on the outside like that of the separating material used in the PMMA array test. But there is also the electrolyte and the fact that the pouch is sealed. This causes the off-gassing effect, that has been noted and shown in figure 4.9. The jetting effects are noted and believed to be captured in the first half or so of the HRR for the array tests. This is based on observation from the single cell tests and how the first half of the HRR curves vary with the arrays tests, where the last half of the data is a lot more repeatable.

Since the lithium-ion pouch cells are sealed, this has an effect on the results when burning. The point where the pouch ruptures and the heated gases eject and burn clearly varies more than the rest of the cell burning. The study by Zhang et al. (129) compares the HRR curves of various electrolyte mixtures. There is a large variation in the HRR curves, with some electrolyte mixtures having single peaks, other having multiple peaks. This can explain how both the array tests and how the single cell tests have such different characteristics to the dried cells. As observed and discussed, the electrolyte has a large effect on the overall HRR curves.

4.6 Understanding Lithium-ion Cells as a Commodity

As mentioned, with this data, the intent is to quantify and understand the metrics associated with the fire hazard and fuel load. There is a large amount of literature review that shows studies of the HRR and THR for both bench scale and large-scale testing of various commodities from bulk storage to standard living spaces. As listed before, NFPA 13 gives a list that describes the various classes of commodities and how to size sprinkler systems for each class. With increasing fuel, there is an increase in total sprinkler coverage and flow rates. To better understand the total fuel load of lithium-ion cells, tables with the heat of combustion are below.

$$\Delta h_c = -\frac{(H_2 - H_1)}{m_{F,r}} \tag{4.7}$$

The heat of combustion given in equation 4.7 gives the total change in enthalpy per volume of fuel reacted (87). The units of the heat of combustion is typical $MJ/kg_{F,r}$ or $kJ/g_{F,r}$.

Table 4.14: PMMA Heat of Combustion

	Mass Loss (g)	**Total heat Release (kJ)**	**Heat of Combustion (kJ/g)**
Test 1	269.81	6492.09	24.06
Test 2	269.42	6493.49	24.10
Test 3	266.40	6462.01	24.26
Mean	268.55	6482.53	24.14
Std. Dev.	1.87	17.78	0.10
Uncertainty (±)	4.63	44.17	0.26

The testing for the five-sample array of PMMA gave a total mass loss of an average of 268.55 grams and a total heat release of 6483 kJ shown in table 4.14. This gives a Δh_c calculated in this experiment of 24.14 $kJ/g_{F,r}$ compared to the literature value of 24.2 $kJ/g_{F,r}$. This same approach can be used in conjunction with lithium-ion cell testing.

Since the mass data for the array testing has a large error due to the thermocouple wires pulling down. The single cell data can be used to determine the heat of combustion for the single cells, and then scaled to the five-cell array. The values compared with the THR from the test data.

Table 4.15: 500 mAh Single Cell Heat of Combustion

	Initial Mass (g)	**Mass Loss (g)**	**Total heat Release (kJ)**	**Heat of Combustion (kJ/g)**
Test 1	10.06	4.03	41.63	10.32
Test 2	10.08	1.85	48.01	26.02
Test 3	10.24	2.08	49.40	23.80
Mean	10.13	2.65	46.35	20.05
Std. Dev.	0.10	1.20	4.14	8.49
Uncertainty (±)	0.24	2.99	10.29	21.10

Taking the single cell mass loss for the 500 mAh cells and the THR in table 4.15 gives an average heat of combustion of 20.05 kJ/g. Note that test one has a lot more mass loss than two and three. This is again due to the uncertainty in the mass loss data as previously discussed.

Table 4.16: 800 mAh Single Cell Heat of Combustion

	Initial Mass (g)	Mass Loss (g)	Total heat Release (kJ)	Heat of Combustion (kJ/g)
Test 1	16.89	3.67	65.93	17.98
Test 2	16.92	3.82	69.75	18.25
Test 3	16.94	5.16	68.93	13.36
Mean	16.92	4.22	68.20	16.53
Std. Dev.	0.03	0.82	2.01	2.75
Uncertainty (±)	0.07	2.04	4.99	6.83

Using the same approach, single cell mass loss for the 800 mAh cells and the THR in table 4.16 gives an average heat of combustion of 16.53 kJ/g. This is slightly lower than that of the 500 mAh single cells. This could be due to more electrolyte or a different electrolyte mixture associated with the 800 mAh cells. This needs to be further investigated, and the dried cell tests and cell deconstruction below will help understand this.

Table 4.17: 500 mAh Dried Cell Heat of Combustion

	Initial Mass (g)	Mass Loss (g)	Total heat Release (kJ)	Heat of Combustion (kJ/g)
Test 1	9.04	0.97	27.53	28.30
Test 2	9.00	0.83	25.96	31.16
Test 3	9.04	0.88	24.32	27.74
Mean	9.02	0.89	25.94	29.07
Std. Dev.	0.02	0.07	1.61	1.84
Uncertainty (±)	0.06	0.18	3.99	4.56

The dried cells have a heat of combustion that is actually higher than the non-dried cells. Table 4.17 gives an average heat of combustion of 29.01 kJ/g. This value is along the same magnitude of nylon (24.2 kJ/g) and polypropylene (30.8 kJ/g) (87). This makes sense, as the only part burning should be the plastics that are left in the dried cell.

Table 4.18: 800 mAh Dried Cell Heat of Combustion

	Initial Mass (g)	Mass Loss (g)	Total heat Release (kJ)	Heat of Combustion (kJ/g)
Test 1	15.30	3.08	41.87	13.59
Test 2	15.45	1.62	39.46	24.39
Test 3	15.41	2.08	43.03	20.73
Mean	15.39	2.26	41.45	19.57
Std. Dev.	0.08	0.75	1.82	5.49
Uncertainty (±)	0.19	1.86	4.52	13.65

Table 4.18 above gives the heat of combustion for the 800 mAh dried cells. The average heat of combustion is 19.57 kJ/g, which is much lower than the 500 mAh dried

cells. This might come from some of the electrolyte still being inside of the 800 mAh cell, lowering this heat of combustion. This could be due to some of the electrolyte still left inside of the cell, pulling the total heat of combustion down. This is apparent, as the heat of combustion is lower for the electrolyte compared to plastics. The electrolyte should have a heat of combustion ranging from 13.2 kJ/g to 20.9 kJ/g as measured by Zhang et al. (129). This could explain the lower over all heat of combustion for the 800 mAh cell compared ot the 500 mAh dried cells. Other dried cell tests would need to be performed in future work to investigate this.

Table 4.19: 500 mAh Array Computed Total Heat Released

	Mass Loss from Five Cells (g)	**Mass Loss times Heat of Combustion (kJ)**	**Calculated minus Measured Total Heat Released (kJ)**
Test 1	20.17	208.17	-44.75
Test 2	9.23	240.04	-12.88
Test 3	10.38	247.01	-5.91
Mean	13.26	231.74	-21.18

Using the heat of combustion and the mass loss data from the 500 mAh single tests, the THR for a five cell s can be computed and compared to the measured array THR to help verify the results in table 4.15. Since mass loss data for the array was not correct due to the thermocouples, this drove using five times the single cell data. The average 500 mAh array THR was subtracted from the computed THR to compare the difference. Based on table 4.19, the computed THR in the array is very close to the measured, with an average of 231.74 kJ compared to 252.92 kJ as measured with a difference of 21.18 kJ.

Table 4.20: 800 mAh Array Computed Total Heat Released

	Mass Loss from Five Cells (g)	**Mass Loss times Heat of Combustion (kJ)**	**Calculated minus Measured Total Heat Released (kJ)**
Test 1	18.34	329.67	-16.38
Test 2	19.10	348.73	2.68
Test 3	25.80	344.66	-1.39
Mean	21.08	341.02	-5.03

Applying the same method for the 800 mAh array, the THR for the 800 mAh cells can be computed and compared to the actual heat released to help verify the results in table 4.16. Based on table 4.20, the computed THR in the array is again very close to the measured, with an average of 341.02 kJ compared to 346.05 kJ as measured with a

difference of 5.03 kJ. This shows based on the single cell heat of combustion that it can be scaled to an array test and provide very close results.

4.6.1 Fuel Load on Volume Basis

To further develop an understanding of the fire hazard and fuel load for lithium-ion pouch cells, using the HRR and THR per volume will be the next approach. This will give the ability to compare bench-scale testing to larger scale fuel loads.

Table 4.21: 500 mAh Single Cell Total Heat Release Data per Volume

	Peak HRR (kW/m^3)	**Mean HRR (kW/m^3)**	**Total heat Release (MJ/m^3)**
Test 1	100615.72	66191.50	7016.30
Test 2	130861.08	69148.19	8090.34
Test 3	162325.15	75684.63	8325.31
Mean	131267.32	70341.44	7810.65
Std. Dev.	30856.72	4857.75	697.89
Uncertainty (±)	76658.52	12068.29	1733.79

Normalizing the THR with the volume of the single 500 mAh cell gives an average THR of 7811 MJ/m^3 shown in table 4.21.

Table 4.22: 800 mAh Single Cell Total Heat Release Data per Volume

	Peak HRR (kW/m^3)	**Mean HRR (kW/m^3)**	**Total heat Release (MJ/m^3)**
Test 1	101060.67	55144.74	7499.68
Test 2	130581.26	57907.00	7933.26
Test 3	178277.81	76868.62	7840.60
Mean	136639.92	63306.78	7757.85
Std. Dev.	38963.47	11825.82	228.33
Uncertainty (±)	96798.44	29379.34	567.24

Tables 4.21 and 4.22 gives the HRR and THR per unit volume from the single cell data. The volume of single 500 mAh cell is $5.934e^{-6}$ m^3 and the volume of a single 800 mAh cell is $8.792e^{-6}$ m^3. The total volume of the arrays is five times the single cell, with the 500 mAh array being $2.967e^{-5}$ m^3 and the volume of the 800 mAh array is $4.396e^{-5}$ m^3. The average total heat release for the 500 mAh array is 253 kJ and for the 800 mAh array its 346 kJ per table 4.11. Using the range for the THR per volume given by the single cells, at 7758 to 7811 MJ/m^3, this can be used to estimate the THR by multiplying the volume of

the array and then comparing it with the measured THR.

This approach can also be used with the peak HRR and mean HRRs. Compared with the 500 mAh cell data, the 800 mAh cells have a THR per volume of 7758 MJ/m^3 per table 4.22. This data is only slightly different, by less than 100 MJ/m^3. With the heat of combustion, values have a larger variation between cells, the density of each cell can be compared by referring to table 4.2. The 500 mAh cells have an average mass of 10.13 grams, giving a density of 0.0017 grams/mm^3. The 800 mAh cells have an average mass of 16.92 grams with a density of 0.0019 grams/mm^3. With similar total heats released per volume, but a large difference in the heat of combustion between the cells, this could be due to the 500 mAh cells being less dense but having about the same THR per volume.

To help further understand the fire hazard and the effect of electrolyte, the dried cells have also been analyzed on a per volume basis.

Table 4.23: 500 mAh Dried Cell Total Heat Release Data per Volume

	Peak HRR (kW/m^3)	**Mean HRR (kW/m^3)**	**Total heat Release (MJ/m^3)**
Test 1	107018.67	64436.12	4639.40
Test 2	110087.26	58332.61	4374.95
Test 3	103995.50	55384.20	4098.43
Mean	107033.81	59384.31	4370.93
Std. Dev.	3045.91	4616.70	270.51
Uncertainty (±)	7567.07	11469.44	672.03

Table 4.23 shows the THR per volume for the 500 mAh dried cells. Comparing with the cells at 0% SOC, the dried cells are nearly half, at 56% when comparing the averages.

Table 4.24: 800 mAh Dried Cell Total Heat Release Data per Volume

	Peak HRR (kW/m^3)	**Mean HRR (kW/m^3)**	**Total heat Release (MJ/m^3)**
Test 1	114498.46	51215.73	4763.06
Test 2	107870.96	56102.74	4488.22
Test 3	103038.79	49434.31	4894.00
Mean	108469.40	52250.93	4715.09
Std. Dev.	5753.23	3452.64	207.10
Uncertainty (±)	14292.96	8577.52	514.50

Table 4.24 shows the THR per volume for the 800 mAh dried cells. Comparing with

the cells at 0% SOC, the dried cells are nearly half, at 61% when comparing the averages. So overall, the electrolyte contributes a large amount to the THR. This shows the electrolyte in the cell is leading to a large part of the total fuel load. It leads to a large peak in the HRR initially, causing the total area under the HRR curve to be a lot larger.

Table 4.25: 500 mAh Array Total Heat Release Data per Volume

	Peak HRR (kW/m^3)	**Mean HRR (kW/m^3)**	**Total heat Release (MJ/m^3)**
Test 1	40772.04	21167.61	8445.88
Test 2	45275.92	26048.99	8309.63
Test 3	49453.30	28630.15	8818.09
Mean	45167.08	25282.25	8524.53
Std. Dev.	4341.65	3789.90	263.20
Uncertainty (±)	10786.13	9415.38	653.87

Additionally, the THR per volume can also be derived from the array tests and again compared with the single cell data. Taking five times the volume of the single cell and dividing the 500 mAh array peak HRR, mean HRR and THR can be seen in table 4.25. The peak heat release for the 500 mAh array is 8525 MJ/m^3 which is very similar to 500 mAh single cell data, with the average HRR per volume 7811 MJ/m^3.

Table 4.26: 800 mAh Array Total Heat Release Data per Volume

	Peak HRR (kW/m^3)	**Mean HRR (kW/m^3)**	**Total heat Release (MJ/m^3)**
Test 1	40748.27	19525.62	8161.71
Test 2	27604.99	15092.09	8119.55
Test 3	36182.12	19406.02	7335.48
Mean	34845.12	18007.91	7872.24
Std. Dev.	6672.87	2525.88	465.33
Uncertainty (±)	16577.65	6275.14	1156.04

Again, using the same method with the 800 mAh array, the THR per volume is 7872 MJ/m^3 per table 4.26. The range for the THR per volume is 7758 to 8525 MJ/m^3 between the single cell and array tests. Using this method makes sense and shows by the fact that the range by volume is consistent. This will help quantify and rank this hazard with well-known commodities.

4.6.2 Cell Deconstruction

Breaking the cells down, the mass of each component used to construct the cell can be determined. Comparing with other cells can help establish how different various cells are and how that can affect the overall results.

Table 4.27: Cell Tear Down

500 mAh Mass Breakdown (grams)					
Cathode	Anode	Packaging	Tabs	Separator and Separator Tape	Total Mass
4.53	3.24	0.68	0.13	0.53	9.11
800 mAh Mass Breakdown (grams)					
Cathode	Anode	Packaging	Tabs	Separator and Separator Tape	Total Mass
7.86	5.48	1.14	0.18	0.92	15.57

Table 4.27 gives the mass of each major component in the 500 mAh and 800 mAh cells. The cells were dried then sliced open along the sides. During the drying process, the side opposite of the tabs was sliced open, as previously mentioned. From there the tabs, package and tape were all removed in one piece, leaving the cathode, anode and separator sheet together. The separator was peeled open and the cathode and anode pieces were kept separate to determine the mass. As much of the loose carbon particulates were captured as possible when tearing down the cells.

Table 4.28: Cell Tear Down Comparison (% mass)

Reference	Form Factor	Nominal Capacity (Ah)	Cathode Chemistry	Cathode (%)	Anode (%)	Electrolyte (%)	Separator (%)	Packaging (%)	Total (%)
500 mAh Cell	Pouch	0.5	LCO	44.5	31.8	10.6	5.2	7.9	100.0
800 mAh Cell	Pouch	0.8	LCO	45.7	31.9	9.4	5.3	7.7	100.0
Ribiere (2012) (62)	Pouch	2.9	LMO	44.0	35.0	11.0	2.0	6.0	98.0
Somandepalli (2014) (117)	Pouch	2.1	LCO	42.4	34.9	9.5	6.4	6.8	100.0
Golubkov (2014) (72)	18650	2.6	LCO/NMC	45.1	24.8	10.4	2.7	16.9	100.0
Golubkov (2014) (72)	18650	1.5	NMC	33.4	31.8	10.2	3.2	21.3	100.0
Golubkov (2014) (72)	18650	1.1	LFP	30.3	23.3	16.4	3.1	26.9	100.0

Comparing the cell deconstruction results with other literature, the results are very similar. Table 4.28 above shows the 500 mAh and 800 mAh cells are very similar in terms of the overall constructions and mass fraction with the 2.9 Ah cells tore down by Ribiere et al.

(62) and with Somandepalli et al. (117). The cells by Golubkov et al. (72) are cylindrical rather than pouch cells with different chemistries.

The total heat release for the electrolyte can be determined from the difference in the THR from the dried cell compared to the non-dried cell. The 500 mAh cell had a difference of 20.41 kJ from the cell at 0% SOC to the dried cell. The average mass difference is 1.057 grams average across the three cells. Since the electrolyte for the specific cells is not specified by the vendor in terms of the exact fractions of each initial electrolyte species, this can be used to determine the overall heat of combustion. Taking the THR difference and dividing by the mass difference gives Δh_C of 18.92 kJ/g. Taking the same approach for the 800 mAh cells with a mass difference of 1.558 grams and a THR difference of 26.75 kJ, the total heat of combustion for the electrolyte is 17.33 kJ/g. The calculated heat of combustion for the electrolyte by Somandepalli et al. is 19.31 kJ/g. The heat of combustion for electrolytes from Zhang et al. (129) is 13.2 kJ/g for EC, 20.9 kJ/g for DEC and 14.5 kJ/g for DMC. The manufacturer does not break down the exact composition for the electrolyte, but it is clear the measured value is of a mix of the various electrolytes.

Table 4.29: 500 mAh Cell Tear Down Heat Release Rate: Ideal Δh_c

500 mAh Total Heat Released				
Component	Assumed Chemical Compound	Ideal Heat of Combustion (kJ/g)	Mass (grams)	Total Heat Released (kJ)
Packaging (Inner)	Polypropylene	42.66	0.22	9.59
Packaging (Outer)	Nylon	28.76	0.22	6.46
Separator	Polypropylene	42.66	0.53	22.40
Electrolyte	EC:DEC:DMC	18.92	1.08	20.49
Computed Total Heat Released				58.94
Average Measured Total Heat:				46.35
Percent Difference (%):				21.36

To further understand how the cell burned, the total heat of combustion for each material measured during the cell deconstruction was compared with the measured value. Table 4.29 gives the breakdown of the combustible materials, the electrolyte, and the heat of combustion values from Walters et al. (130). The separator is made from polypropylene, which is straightforward to understand the THR. The packaging is a bit more complicated. It is made from nylon, polypropylene and aluminum. It was assumed each material takes

approximately 1/3 of the total mass of the packaging. With this assumption, the heat of combustion from the computed THR compared to the measured is different, by just over 21% or 12.59 kJ. this could be due to some of the separator in the cell not completely burning, a different actual mass fraction of the packaging, or just tolerance error from cell to cell having slightly different mass fractions. Additionally, the heat of combustion for the electrolyte will have some uncertainty, as the complete electrolyte may have not been removed during the evaporation process.

Table 4.30: 800 mAh Cell Tear Down Heat Release Rate: Ideal Δh_c

800 mAh Total Heat Released				
Component	Assumed Chemical Compound	Ideal Heat of Combustion (kJ/g)	Mass (grams)	Total Heat Released (kJ)
Packaging (Inner)	Polypropylene	42.66	0.38	16.11
Packaging (Outer)	Nylon	28.76	0.38	10.86
Separator	Polypropylene	42.66	0.92	39.08
Electrolyte	EC:DEC:DMC	17.33	1.62	28.02
Computed Total Heat Released				94.06
Average Measured Total Heat:				68.20
Percent Difference (%):				27.49

The 800 mAh cell has a similar difference in the computed compared to measured THR as shown in table 4.30. The difference is 27.49% or 25.86 kJ which is a bit more of a difference than that 500 mAh comparison.

The percent error also could be so large due to the heat of combustion value not being ideal. When burning, if only carbon dioxide and water form, it is ideal. Yet most combustion processes are not quite ideal, as soot, carbon monoxide and other hydrocarbons are found in the product side. This can be taken into account by using the actual verse the ideal heat of combustion estimates for the different materials as shown below. The heat of combustion values are from The Fundamentals of Fire Phenomena (87).

Table 4.31: 500 mAh Cell Tear Down Heat Release Rate: Actual Δh_c

500 mAh Total Heat Released				
Component	Assumed Chemical Compound	Actual Heat of Combustion (kJ/g)	Mass (grams)	Total Heat Released (kJ)
Packaging (Inner)	Polypropylene	38.6	0.22	8.67
Packaging (Outer)	Nylon	27.1	0.22	6.09
Separator	Polypropylene	38.6	0.53	20.27
Electrolyte	EC:DEC:DMC	18.92	1.08	20.49
Computed Total Heat Released				55.52
Average Measured Total Heat:				46.35
Percent Difference (%):				16.52

The error using the actual heat of combustion is only 16.52% as shown in table 4.31 for the 500 mAh cell comparison. This error is about 5% less than the ideal heat of combustion case. This shows that the assumption of using 1/3 of the mass for the two combustible materials in the packaging is a good assumption and the computed compared to the measured values are very close.

Table 4.32: 800 mAh Cell Tear Down Heat Release Rate: Actual Δh_c

800 mAh Total Heat Released				
Component	Assumed Chemical Compound	Actual Heat of Combustion (kJ/g)	Mass (grams)	Total Heat Released (kJ)
Packaging (Inner)	Polypropylene	38.6	0.38	14.57
Packaging (Outer)	Nylon	27.1	0.38	10.23
Separator	Polypropylene	38.6	0.92	35.36
Electrolyte	EC:DEC:DMC	17.33	1.62	28.02
Computed Total Heat Released				88.18
Average Measured Total Heat:				68.20
Percent Difference (%):				22.66

Again, the error for the 800 mAh cell using the actual heat of combustion values is 22.66%. This is 5% or so less error than using the ideal heat of combustion. Further deconstructions and comparison would be needed to better understand the material breakdown. On such small cells, a small difference in the total measured mass of each component can have a large difference in the THR.

It has been established that the packaging for LCO pouch cells is very similar. Even with the 18650 formats, the packaging mass fraction is along with the same magnitude. The heat of combustion for the various electrolyte chemistries is all close. Yet with the cylindrical cell form factor, the different cathode chemistries have a lot different break down in terms

of the mass of each material. With the test by Larsson et al. (122) consisting of a five-cell array burning at 0% SOC, the THR per volume can be compared from the results with the 800 mAh and 500 mAh array. This can help further understand how the results vary.

At 0% SOC, the five cell LFP array had a THR of 8.314 MJ in the study by Larsson et al. The nominal dimensions of each cell are 220 mm by 145 mm by 4.5 mm. This gives a total volume of $1.44e^{-4}$ m^3 per cell and an array volume of $7.18e^{-4}$ m^3. Taking the THR and dividing it by the total volume gives 11583 MJ/m^3. This is higher than the 8525 MJ/m^3 for the 500 mAh array and 7872 MJ/m^3 for the 800 mAh array. In the deconstruction results by Somandepalli, the packaging materials, separator, and tapes are made from chemicals compounds such as nylon, polypropylene, and polyester terephthalate. The heat of combustion for these materials ranges from 28.76 kJ/g to 42.66 kJ/g per the study by Walters et al. (130). With the 18650 LFP cell having a lot more packaging material compared to the LCO/NMC cell, this might be similar in the pouch cells too. Yet it should be noted the 18650 packaging has an aluminum casing rather than a plastic pouch. The heat of combustion for the packaging materials involved is a lot higher than that of the electrolytes, and this could cause the fire hazard for the LFP cells to be higher than that of the LCO.

When understanding lithium-ion cells as a commodity, it is important to understand the variations in different electrolytes, form factor type, and packaging to understand what the fire hazard is. Additionally, the volume to area effect can change how much plastics per volume there is in a single pouch cell. This will directly affect the fire load. Additional analysis using the total cell energy in kWh will be in Appendix C.

4.7 Comparing with other Fuel Loads & Hazards

In chapter three, the vent gases from lithium-ion cells were compared with other well-known flammable gases. This helped quantify the deflagration hazard of this vent gas with well-known hazards. Using a similar comparison approach, understanding well-known

commodities and referring to NFPA 13 can understand documented design guidance for sprinkler systems. This will help give further understanding and guidance on how to protect from lithium-ion cells in a stored commodity and additionally shed light on how to protect Li-BESS. The following will give examples of various commodities defined in NFPA 13 Annex A:

1. Wood- Particle Board
2. Group B: Cellulosic Paper Products
3. Group A Expanded: Polystyrene
4. Group A Non-Expanded: Polypropylene

From NFPA 13 Annex A table A.5.3.1.1, the definitions of how the commodities listed fit into a commodity class will help give a better understanding of each of these fuel loads. Wood products, not in any containers are considered a class III, so the first commodity is a stack of particle board. Taking the Group B plastic into account, a non-containerized pallet of this is considered a class IV commodity. Group A plastics that are exposed are considered either exposed expanded or non-expanded Group A plastics. Lastly, a mixed group commodity of 25% by volume expanded, non-expanded group A plastics, particle board and group B plastic will be used as well.

1. Class III: Exposed Wood- Particle Board
2. Class IV: Exposed Cellulosic Paper Products
3. Group A Exposed Expanded Plastic: Polystyrene
4. Group A Exposed Non-Expanded Plastic: Polypropylene
5. Mixed Group A Exposed: Polypropylene, Polystyrene, Cellulosic Paper Products, and Particle Board

The example used to show how the lithium-ion cells compare with the commodities listed above is by tabulating the THR from a 1 m^3 cube of material. From there, design criteria in NFPA 13 can give a better understanding for how to approach this commodity.

Table 4.33: Commodity Comparison

Commodity	**Volume (m^3)**	**Total Heat Release per Volume (MJ/m^3)**		**Fuel Load (MJ)**
500 mAh LCO Pouch Cell	1	7811		7811
800 mAh LCO Pouch Cell	1	7758		7758
Commodity	**Density (kg/m^3)**	**Mass (kg)**	**Heat of Combustion (MJ/kg)**	**Fuel Load (MJ)**
Class III: Exposed Wood-Particle Board	190	190	18	3325
Class IV: Exposed Cellulosic Paper Products	1500	1500	20	30000
Group A Exposed Expanded Plastic: Polystyrene	25	25	40	1000
Group A Exposed Non-Expanded Plastic: Polypropylene	900	900	27	24390
Mixed Group A Exposed: Polypropylene, Polystyrene, Cellulosic Paper Products and Particle Board	654	654	22	14679

Table 4.33 shows the various commodities and what the total fuel load for each compared to the same volume of lithium-ion pouch cells. Based on table 5.6.3.3.3 in NFPA 13, with a mixed un-expanded volume fraction of 25% and an expanded group A plastic of 25%, the mixed commodity is considered a group A unexpanded commodity. The method used for the mixed commodity is based on the following from the SFPE 2016 Handbook (31):

$$\bar{H}_{\mathrm{L}} = \frac{1}{M_{\mathrm{tot}}} \sum_{i=1} M_{\mathrm{i}} * H_{\mathrm{u,i}} \tag{4.8}$$

Equation 4.8 shows how the averaged heat of combustion for mix materials which is based on the mass fraction of each individual material heat of combustion. The heat of combustion values come from Structural Design for Fire Safety chapter three (131) and the densities from the engineering toolbox (132). The fuel load for this mixed commodity is very similar to the battery fuel load.

The design guidelines are found in chapter 11-22 of NFPA 13 to determine the sprinkler coverage requirements based on storage height and commodity type. Various figures throughout NFPA 13 gives the total gallons per minute per square foot (GPM/ft^2) based on the coverage area of the sprinklers and the commodity classification. The assumption here is solid piled commodities that are stored at ground level. Using an assumed sprinkler coverage area of 3000 ft^2 or 279 m^2, according to NFPA 13 Ch. 13, the class III and IV use the OH1 (Ordinary Hazard 1) design curve. This would give a sprinkler density of 0.17 GPM/ft^2. Continuing, the exposed group A plastics require a design curve for OH1 design curve. For all these low piled commodities, use the same design curve and in an area of sprinkler operation of 3000 ft^2, this gives a flow of 510 GPM. As the storage height increases, the different commodities require increasing sprinkler flow rates. When class A plastics are stored at a height above five feet, the design jumps to the EH2 (Extra Hazard 2) design curve. This requires a density of 0.38 GPM/ft^2 or 1140 GPM. Compared to the class III and IV, the OH1 design curve allows for a storage height of 12 feet for the class II and 10 feet for the class IV. Per NFPA 13, the heat released for class I through IV is considered moderate whereas group A plastics have a heat release to be considered high. Based on table 4.33, the lithium-ion cells have a total heat release that is somewhere between class III and group A expanded plastic at a 0% SOC.

The test by FM Global (59) compares lithium-ion batteries with unexpanded plastics and class II commodities in terms of testing. Based on the packaging ratio, or fill density of lithium-ion cells or batteries in a shipping box, for example, the commodity classification could change. This is important to understand and can be used as a means to establish guidance on sprinkler design. Additionally, at a low SOC, lithium-ion cells or batteries similar to plastics in terms of the fuel load. The electrolyte, as determined from this study and other literature, actually has a lower heat of combustion than the plastics constructing the pouch cell. Establishing and ranking lithium-ion cells at low SOC as a commodity has been done through this bench-scale testing, and the fuel loads for specific cases can be computed using the data from these tests. Where the fire hazard associated with lithium-ion cells becomes more challenging is when used in Li-BESS at higher SOC. The fuel load is

understood at a low SOC, and as mentioned in chapter two, discharging during an error state might make the system safer. At a SOC of 0%, the method to obtain the fuel load has been outlined in this chapter. This can provide further development and quantitative reasoning for designing fire safety systems and failure responses for Li-BESS.

Chapter 5

Conclusions

With the unique hazard associated with lithium-ion battery energy storage systems, research and development are critical to understand and provide methodologies to safely develop and integrate these systems. As the means to produce and use Li-BESS increase, so will the potential consequences of failure. Previous emerging technologies have shown this issue, with hot water boilers having multiple failure incidents prior to the formation of codes and standards to provide safety guidance. This shows the absolute need to proactively develop and enforce safety codes and standards rather than reacting to an incident before safety becomes a focus. While the potential for lithium-ion cells to store energy is not at all questioned, how to safely use these systems needs to be further understood. With complex systems, failures can occur on many levels. In the case of Li-BESS, failures can occur at a cell, module or rack level, within systems such as battery management, thermal management, or with the quality control, design and use of the system. Understanding this can help more effectively develop and write codes and standards for the safety community to effectively manage and control Li-BESS installations.

The incidents in chapter two show that failure of lithium-ion cells occurs at all levels. Small-scale consumer electronics such as phones, laptops, and e-cigarettes have numerous reports and instances of failure. Transportation of lithium-ion cells has led to numerous accidents while being transported by air, which has led the US FAA to ban air transportation of bulk cells. Electric vehicle failures have led to fires that require a large amount of time and resources from first responders. As more all-electric vehicles are produced, means of protecting them from such volatile failures will need to be targeted. Large scale Li-BESS have numerous failures which have led to fires and/or deflagration events. Yet these failures are not captured in a centralized location, leading to speculation and assumptions on the causes and consequences.

Research of the failures at a cell level has been performed for over twenty years. This data needs to be utilized to provide guidance and design criteria for safer Li-BESS. Numerous experiments have shown the breakdown of the gas species that are vented during failure of a lithium-ion cell. When venting, the various cathode chemistries produce similar species compositions. The vent gas contains carbon-dioxide, carbon monoxide, hydrogen, and various hydro- carbons. The quantity of each species varies by the cathode chemistry and state of charge. Taking these different flammable gas mixtures, models created with Cantera were used to estimate the lower flammability limit, laminar flame speed, and maximum overpressure shown in chapter three. These metrics help understand and characterize the explosion hazard associated with lithium-ion cells. Known explosion hazards such as methane, hydrogen, propane and combustible dusts have been researched and safety practices have been established using standards such as NFPA 68 and 69. By applying the prescribed guidance to size deflagration vents and using the models for flame speed and maximum overpressure, a means to further characterize the hazard of lithium-ion cells was further established. The vent gas explosion metrics have a similar magnitude as class 1-3 dusts, propane, methane, and even hydrogen.

Using the modeled laminar flame speed and overpressure with the prescribed method in NFPA 68 to size deflagration vents further helped rank lithium-ion cell vent gas with known explosion hazards. What was concluded from this study was that the LFP cathode chemistry has a lower hazard compared to LCO and NCA at 100% SOC. Additionally, guidance on how to apply NFPA 68 can help the safety community verify their own safety systems. This method of using the vent gas model results with a well-known prescribed standard such as NFPA 68 helps understand and rank Li-BESS vent gas with other well-known hazards. The benefit of the models and methodologies provided in chapter three is they are all open source and can be used by other members of the safety community.

In addition to the deflagration and explosion hazards which are associated with lithium-ion cells and Li-BESS, the fire hazard and fuel loads were researched. Testing using

a bench-scale oxygen consumption cone calorimeter measured the products of burning cells, dried cells, and arrays at 0% SOC. As discussed in chapter four, LCO cells produce oxygen at a high state of charge when burning due to the electrolyte reactions. At a low state of charge, this oxygen production significantly reduces. Testing was done for nominally 0% SOC LCO pouch cells to prevent uncertainties from this oxygen production. The intent of the single cell and array studies was to help further development and understanding of lithium-ion cells and help characterize how the associated fuel load.

Key metrics in fire hazards are the heat release rate, total heat released, the heat of combustion and mass loss. Through these metrics, analysis and comparison of the fuel load between all three tests were performed. The total heat released for the dried cell is about 30% to 40% less than the non-dried cells. A five cell array was also burnt and the results analyzed. The data when normalized by the volume of the array gives a total heat release per volume of 7800 to 8500 MJ/m^3. The single cells give a range from 7700 to 7800 MJ/m^3. This shows that the single cell data scales up with the five cell array on a volume basis. Additionally, the PMMA array was tested to draw further conclusions of the effects of burning separated layers of the same material.

The heat of combustion for the electrolyte was calculated through the difference in the total heat released and mass for the dried verse non-dried cells. The total heat released for the dried cells might be less than the non-dried cells, but the heat of combustion is actually larger. This is due to the electrolyte having a lower heat of combustion than the plastics constructing the cell. Single cells were deconstructed in order to determine the mass of each component constructing the pouch cell. Using the individual heat of combustion values from the literature, the computed total heat released from the deconstruction was established to be roughly 20% higher than the measured heat release. With some uncertainty due to measurement and assumptions on exactly what portions of the cell is what material, this validates the measured results. The heat of combustion from the PMMA samples matches with the literature, validating the method and measurements.

Taking the data from the lithium-ion cells, it was determined that placing them between a class III and a mixed group A exposed commodity per NFPA 13 definitions can be used for sprinkler designs. As more data and testing is available, this can be updated. With no formal guidance, designing sprinkler systems around lithium-ion cells requires a performance-based approach. By testing and establishing various metrics such as the heat of combustion and the total heat released per volume for lithium-ion cells, work to improve fire safety system design guidance has been accomplished.

5.1 Future Work

A single repository of failure events involving lithium-ion cells and Li-BESS would benefit the safety community. With scattered reports and no clear understanding of failures around the world, there is a lack of data to help understand and show stakeholders some of the safety gaps and issues. With this emerging technology, it is important to realize the unknown phenomena and address them quickly.

With the models for lower flammability limits, laminar flame speed, and maximum overpressure, validation studies should be performed just to help understand any uncertainties. Additionally, with so many different methods to compute LFL, some studies with various mixtures of the vent gas species just to help validate some of the LFL models. This can provide guidance on which models are appropriate based on the specific gas composition. Additionally, specific chemistries, capacities, form factors, and failure tests should be tested and ranked to further determine the effects of different parameters on the vent gas compositions and overall gas production and rate. Then better design guidelines can be established for sizing Li-BESS ventilation systems. The other concern is the fact that during failure, the gases emitted are hot. Studies can be done to help show the effects on flame speed, but from the theory shown in equation 3.4 as temperature increases, so does the flame speed.

Obstructions, which cause flame speeds to increase due to turbulence effects, cause deflagration vent sizes to increase. With NFPA 68 using the surface area rather than a

blockage ratio or cross-sectional area that other literature uses, this needs to be investigated and updated. Additionally, smaller scale models on a rack-level should be done to understand the limitations of NFPA 68. Perhaps looking at deflagration vent sizing for dust collectors can be used to further develop methods to size vents at the rack level.

For the oxygen consumption calorimeter tests, the effects of oxygen production can be mitigated by using LFP cells. This cathode chemistry does not produce oxygen as discussed by Doughty at al. (133). These cells can be used to understand the heat release rate and the effect of higher states of charge. Also, the total heat released can be computed without having to account for the oxygen produced by LCO or another cell chemistry. Additional testing using dried cells in arrays, larger capacity cells and various chemistries, state of charge and even different electrolytes can even further help develop and rank the hazards while accounting for these different parameters. Perhaps a larger cell in terms of both capacity and volume would take longer to burn. This might dampen out some of the effects noted in the array testing and better establish times between each cell burning. Compared to the PMMA array test, which took about 1100 seconds to completely burn giving distinct peaks for each sample, the 500 mAh and 800 mAh arrays about 330 and 450 seconds to completely burn. Perhaps using larger cells will help prevent as much overlap in terms of burning and help paint a clearer picture of how the arrays burn. From the literature, the electrolyte heat release rate curve varying based on the mixture composition and species. It is clear that varying and understanding the electrolyte effect is important. More testing with lower heat flux from the conical heater might slow down the combustion process, showing different results on how lithium-ion cell arrays burn.

Additionally, cone calorimeter testing using cells with different volume to surface area ratios, states of charge, and cathode chemistries can help establish what specific variables change the results the most. Collecting more data can help resolve uncertainties that were discussed in chapter four. Array testing by configuring the cells such that the thin side of each cell is faced up can help determine how the fire characteristics change and how each cell fails. Also, dried cells need to be further investigated. As mentioned in chapter four,

the dried 800 mAh cells had a smaller overall heat of combustion than the 500 mAh cells. This is hypothesized to be due to the electrolyte in the 800 mAh dried cells to have not completely evaporated.

Overall, studies and analysis provided in this thesis help provide methodologies that can help increase the safety and understanding of Li-BESS. As more data is collected and analyzed, proactive updates to codes and standards can help the safety community understand and enforce Li-BESS safety.

Appendices

Appendix A

NFPA 68 Deflagration Calculator

```
#NFPA 68 Gas Deflagration Vent Calculator
#Disclamer- Use of this code is solely the responsibility of the user
import cantera as ct
import math
#User input function
#Laminar Flame Speed (m/s):
Su = 2.7
#Maximum overpressure (bar-g):
Pmax = 7.85
#Equivalence Ratio
phi = 1.33
#Unburned Gas-Air Mixture Speed of Sound (m/s):
def equilSoundSpeeds(gas, rtol=1.0e-6, maxiter=5000):

    # Set the gas to equilibrium at its current T and P
    gas.equilibrate('TP', rtol=rtol, maxiter=maxiter)
    # save properties
    s0 = gas.s
    p0 = gas.P
    r0 = gas.density
    # Perturb the pressure
    p1 = p0*1.0001
    # Set the gas to a state with the same entropy and composition but
    # The perturbed pressure
    gas.SP = s0, p1
    # Now equilibrate the gas holding S and P constant
```

```
    gas.equilibrate('SP', rtol=rtol, maxiter=maxiter)
    # Equilibrium sound speed
    aequil = math.sqrt((p1 - p0)/(gas.density - r0))
    return aequil,
gas = ct.Solution('gri30.xml','gri30_mix')
# Calls Gas Properties from Gri-MECH
carbon = ct.Solution('graphite.xml')
mix_phases = [(gas, 1.0),(carbon, 0.0)]     # Burned Mixture
gas.set_equivalence_ratio(phi, 'H2:1', 'O2:1,N2:3.76')
T = 300.0
gas.TP = T, ct.one_atm
#Unburned gas-air mixture speed of sound (m/s):
au = equilSoundSpeeds(gas)[0]
#Ratio of Specific Heats for Burned gas-air mixture
gas_b = ct.Solution('gri30.xml','gri30_mix')
#Calls Gas Properties from Gri-MECH
carbon = ct.Solution('graphite.xml')
mix_phases_b = [(gas_b, 1.0),(carbon, 0.0)]
#Burned Mixture
Pi = 101000 #Initial pressure Pa
Ti = 300 #Initial unburned gas temperature K
gas_b.TP = Ti,Pi
gas_b.set_equivalence_ratio(phi, 'H2:1', 'O2:1.0, N2:3.76')
#Mass Density of Unburned Gas-Air Mixture (kg/m^3):
rho_u = gas_b.density
#Unburned gas-air mixture dynamic viscosity (kg/m-s):
mu_u = gas_b.viscosity
#Suppress the next two lines for unburned data
burned = ct.Mixture(mix_phases_b)
#Equilibrate the mixture adiabatically at constant P
```

```
burned.equilibrate('HP', solver='gibbs', max_steps=1000)
gamma_b = gas_b.cp/gas_b.cv #Suppress for unburned data
#Structure Surface Area (m^2):
#Length (m):
L = 6.1
#Depth (m):
D = 2.44
#Height (m):
H = 2.44
#Side Walls
Aw1 = L*H
#Front and Rear Walls
Aw2 = D*H
#Roof and Floor:
Aw3 = D*L
#Total Surface Area
As = 2*Aw1 + 2*Aw2 + Aw3
#Reduced Pressure 2/3 structure ultimate strength (bar-g):
Pred = 0.1
#Intial Pressure (bar-g):
Po = 0.01325
#Static activation pressure of the venting device (bar-g):
Pstat = 0.1
#Unburned Gas-Air Mixture Sonic Flow Mass Flux(kg/m^2-s)
Gu = 230.1
#Vent flow discharge coefficient
#Assume 0.7 if vent area is no bigger than wall area, other wise 0.8:
Cd = 0.7
#Hydraulic Diameter (m):
Dhe = 4*(Aw2/(2*D+2*H))
```

```
print(Dhe)
#Determining Turbulent Factor:
#Vent diameter: Needs to be iterated based off of
#Assumed number of vents and vent area
#Initial assumption 10 vents with a total area of 90% of wall
def ventarea(Av1):
    Dv = math.sqrt((Av1/Vent_Number))
#Reynolds number of flame through structure:
    Re_flame = rho_u*Su*(0.5*Dhe)/mu_u
#Phi 1: Based on Reynolds Number of Flame Front:
    phi_1 = max(1, (Re_flame/4000)**0.39)
    #Maximum Velocity through Vent (m/s):
    uv = min(math.sqrt(Pred*2*10**5/rho_u),au)
    #Reynolds number through vent
    Re_vent = 0.5*rho_u*uv*Dv/mu_u
    #Phi 2: Based on Reynolds Number through Vent:
    beta1 = 1.23
    beta2 = 2.37*10**-3
    phi_2 = max(1, beta1*(Re_vent/10**6)**((beta2/Su)**0.5))
    #Lambda 0:
    Lambda_0=phi_1*phi_2
    #Lambda 1 Based on Obstructed surface area (m^2):
    Aobs = 0.1*As
    #Obstruction Correction Factor
    if Aobs < 0.2*As:
        Lambda_1=Lambda_0
    elif Aobs >= 0.2*As:
        Lambda_1=Lambda_0*math.exp(math.sqrt((Aobs/As)-0.2))
    #L/D
    L_D = L/Dhe
```

```
    #Solving for Lambda:
    if L_D < 2.5:
        Lambda = Lambda_1
    elif L_D >= 2.5:
        Lambda = Lambda_1*(1+((L_D/2.5)-1)**2)
    #L/D Correction Factor
    if L_D > 5:
        print ("L/D Above 5 see NFPA 68 Chapter 9")
    elif Pmax > 10:
        print ("Pmax Above 10 bar-g see NFPA 68")
    #Solving for vent size:
    C = (0.5*Su*rho_u*Lambda/(Gu*Cd))*(((Pmax+1)/(Po+1))*
    *(1/gamma_b)-1)*(Po+1)**0.5
    delta = (((Pstat+1)/(Po+1))**(1/gamma_b)-1)/
    (((Pmax+1)/(Po+1))**(1/gamma_b)-1)
    #Pred Corrction Factor
    if Pred <= 0.5:
        Avo = As*C/math.sqrt(Pred)
    elif Pred > 0.5:
        Avo = (As*Su*rho_u*Lambda/(Gu*Cd))*(1-((Pred+1)/(Pmax+1))*
        *(1/gamma_b))/(((Pred+1)/(Pmax+1))**(1/gamma_b)-delta)
    return(Avo)
#Initial vent area (m^2):
Vent_Number = 8
Vent_Percent = 0.9
Av1 = Vent_Percent*(Aw1)
print("Av1", Av1)
Avg = 0.001
Avo = 0
while 100*abs(Avo-Avg)/(0.5*(Avo+Avg)) > 1:
```

```
        Avo = ventarea(Av1)
        Avg = Av1
        Av1 = Avo
        print("Avo", Avo)
    print("Vent Size Required", Avo, "m^2")
    print("Available Surface Area", As, "m^2")
    if Avo > 0.5*As:
        print("Warning: Vent Size Exceeds Available Surface Area")
```

Appendix B

Additional Lithium-Ion Battery Cone Calorimeter Images

The intent of Appendix B is to give additional images and photos of the cone calorimeter testing.

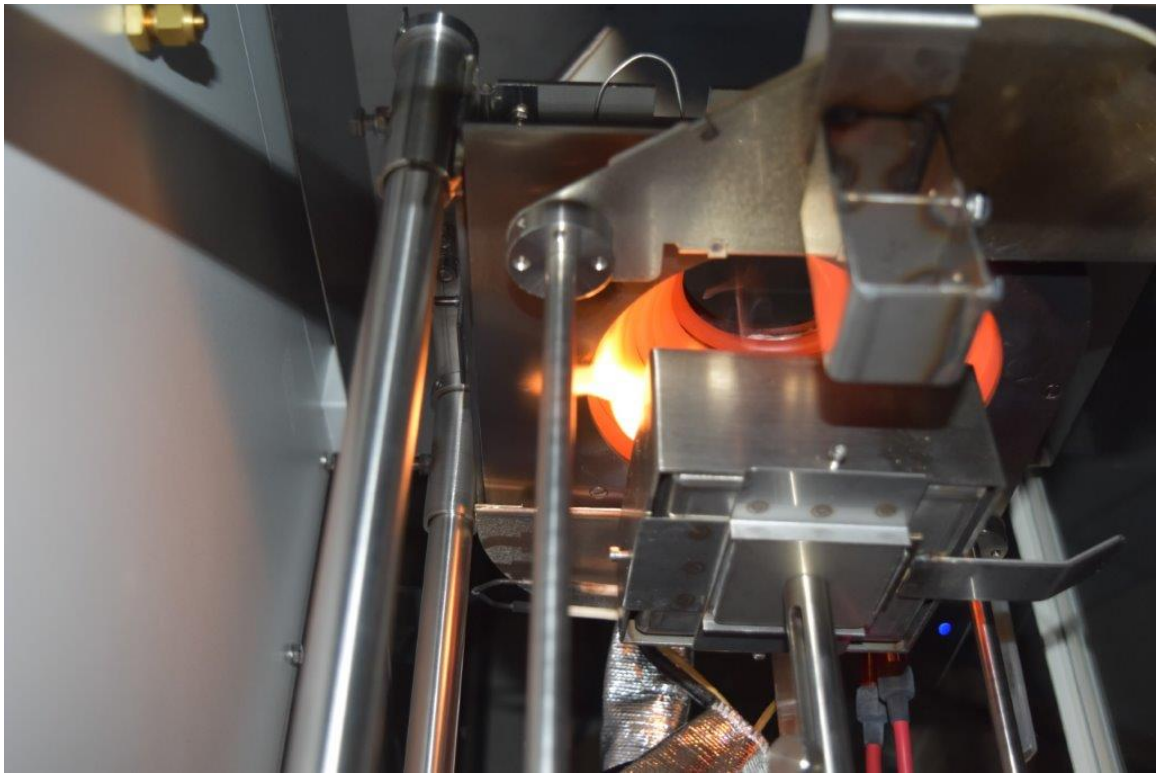

Figure B.1: Single 800 mAh Cell Smaller Jet

Figure B.1 above shows a smaller effect from a single 800 mAh cell jetting. Only a few pictures were captured of this effect due to how difficult it is to see at other angles.

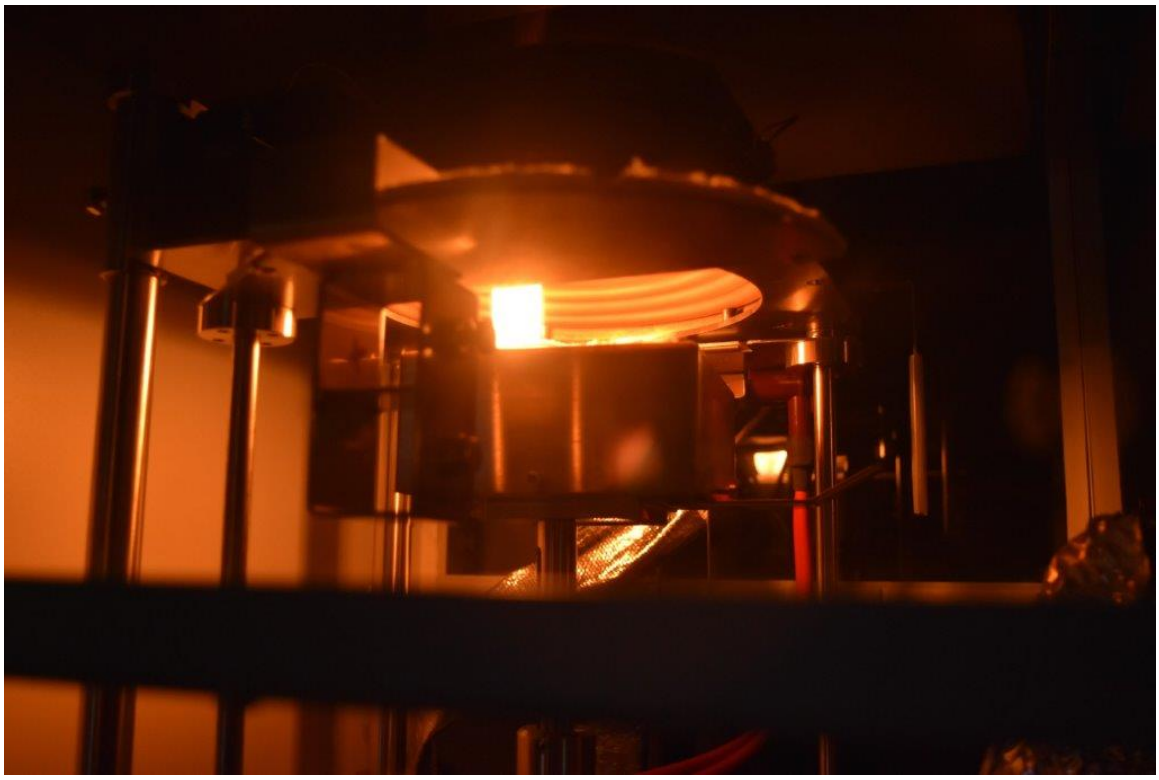

Figure B.2: Single 500 mAh Cell Smaller Jet

Figure B.2 above shows a smaller effect from a single 500 mAh cell jetting. With the 500 mAh cell being smaller in size, rather than ejecting off the side of the sample holder, the jetting is more captured in the exhaust stream and pulled straight up.

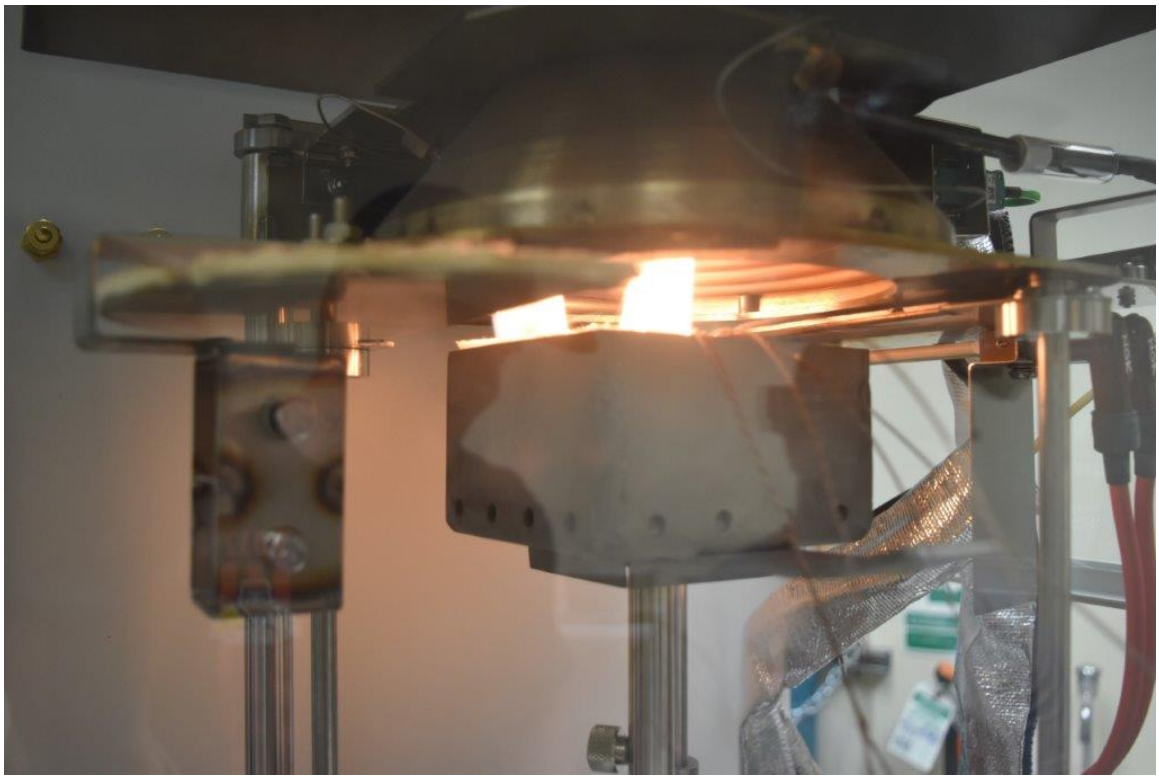

Figure B.3: 500 mAh Array Burning with Small Jet Effect

Figure B.3 shows the jetting effect from the 500 mAh array test. There are two distinct flames, with the top of the cell burning along with the jetting coming from the tabbed area that is facing away from the sample holder handle.

Figure B.4: Post Burn of 500 mAh Array in Modified Sample Holder

Figure B.4 shows another example of the 500 mAh array test after completely burning and bring removed from the cone calorimeter.

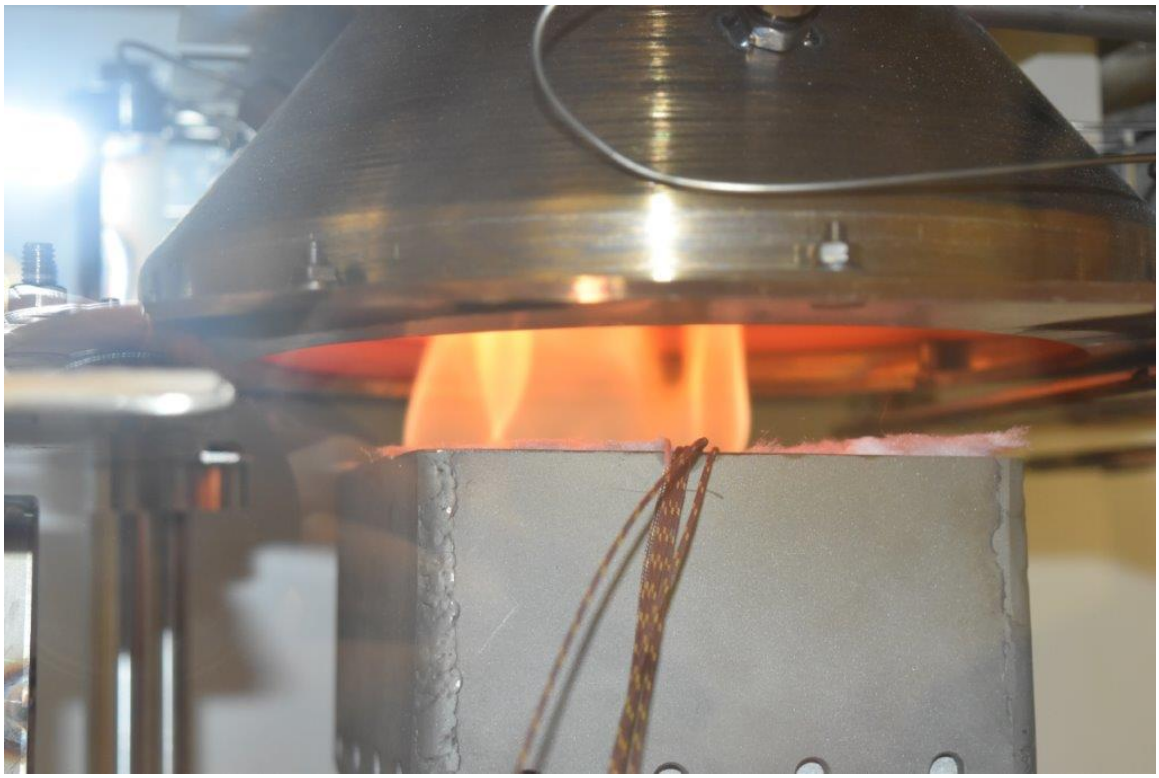

Figure B.5: Jetting of 800 mAh Array

Like the 500 mAh array, figure B.5 shows the burning and jetting effects for the 800 mAh array. The flame is more of a jet and the differences can be noted below.

Figure B.6: Burning of 800 mAh Array Post Jetting Effect

Figure B.6 shows the 800 mAh array burning after the jetting effect is gone. Comparing with figure B.5, the flames are a lot different in terms of color and shape.

Appendix C

Heat Release Rate per Nominal kWh

The intent of Appendix C is to show another to quantify the cone calorimeter tests by using the nominal energy for each cell. Table 4.2 gives a nominal energy of 1.85 Wh for the 500 mAh cell and 2.96 Wh for the 800 mAh cell. The five cell arrays have a nominal energy of 9.25 Wh for the 500 mAh array and 14.8 Wh for the 800 mAh array.

Table C.1: 500 mAh Single Cell Total Heat Release Data per kWh

	Peak HRR (kW/kWh)	**Mean HRR (kW/kWh)**	**Total heat Release (MJ/kWh)**
Test 1	322.73	212.31	22.51
Test 2	419.75	221.80	25.95
Test 3	520.67	242.76	26.70
Mean	421.05	225.62	25.05
Std. Dev.	98.98	15.58	2.24
Uncertainty (±)	245.89	38.71	5.56

The single cell data gives a total heat released average of 25.05 MJ/kWh per table C.1.

Table C.2: 800 mAh Single Cell Total Heat Release Data per kWh

	Peak HRR (kW/kWh)	**Mean HRR (kW/kWh)**	**Total heat Release (MJ/kWh)**
Test 1	300.16	163.79	22.28
Test 2	387.84	171.99	23.56
Test 3	529.51	228.31	23.29
Mean	405.84	188.03	23.04
Std. Dev.	115.73	35.12	0.68
Uncertainty (±)	287.50	87.26	1.68

Compared with the 500 mAh single cell, table C.2 gives the overall total heat released of 23.04 MJ/kWh on average, slightly lower than that of the 500 mAh single cell.

Table C.3: 500 mAh Array Total Heat Release Data per kWh

	Peak HRR (kW/kWh)	**Mean HRR (kW/kWh)**	**Total heat Release (MJ/kWh)**
Test 1	130.78	67.90	27.09
Test 2	145.23	83.55	26.65
Test 3	158.62	91.83	28.28
Mean	144.88	81.09	27.34
Std. Dev.	13.93	12.16	0.84
Uncertainty (±)	34.60	30.20	2.10

The single cell data gives a total heat released average of 27.34 MJ/kWh per table C.3. This is even slightly higher than that of the single cell tests.

Table C.4: 800 mAh Array Total Heat Release Data per kWh

	Peak HRR (kW/kWh)	**Mean HRR (kW/kWh)**	**Total heat Release (MJ/kWh)**
Test 1	121.03	57.99	24.24
Test 2	81.99	44.83	24.12
Test 3	107.47	57.64	21.79
Mean	103.49	53.49	23.38
Std. Dev.	19.82	7.50	1.38
Uncertainty (±)	49.24	18.64	3.43

Table C.4 gives the 800 mAh array test data per kWh. Compared with the 500 mAh array, the 800 mAh as an overall total heat released of 23.38 MJ/kWh on average, slightly lower than that of the 500 mAh single cell and very similar to the single cell data.

A couple of ways this data can be used is by comparing with other literature and further helping understand the MAQ value of 600 kWh value from NFPA 1 Ch. 52.

The 0% SOC array test by Larsson et al. (122) using five LFP cells gives a total heat release of 8.314 MJ. With 5 cells at nominally 22.4 Wh each, this gives a total heat release per kWh of 74.23 MJ/kWh. This is about three times the values from the 500 mAh and 800 mAh tests. The effect from other electrolytes might need to be investigated and how the characteristics change at different states of charge.

Additionally, the maximum allowable quantity per NFPA 1 Ch. 52 is 600 kWh which effects the required documentation or requirements per NFPA 101. From the test data, the

total heat released for a 600-kWh system would be 13824 MJ to 16404 MJ. The total heat release from the test by Larsson would be 44538 MJ. This is drastically different and how this value was obtained should be further investigated and understood with these types of tests.

According to Hua et al. (134) the gravimetric energy density (Wh/kg) of the LFP cell is about 40% of the LCO cell. The volumetric energy density (Wh/L) of the LFP cell is about 35% of the LCO cell. In comparing the array test data with the data from Larsson, the total heat released per kWh for the LCO cell is about 32% compared with the LFP cell. So, the energy density for the LFP cell is a bit more than one-third of the energy density, yet the total heat released per kWh is about three times that of the LCO cell. If the energy density is inverted and the heat of combustion is assumed to be about the same, this actually matches up with measured total heat release per kWh in terms of the difference of the LCO and LFP cells.

Bibliography

[1] "History of ASME Standards." [Online]. Available: https://www.asme.org/about-asme/standards/history-of-asme-standards

[2] "Deadly Historical Fires That Shaped Fire Codes Today|Strike First," Jul. 2016. [Online]. Available: http://www.strikefirstusa.com/2016/07/trial-fire-5-fires-ultimately-improved-world/

[3] D. Toplikar, "MGM Grand, Hilton fires led to improved safety codes - Las Vegas Sun Newspaper," Nov. 2012. [Online]. Available: https://lasvegassun.com/news/2012/nov/21/mgm-grand-hilton-fires-led-improved-safety-codes/

[4] "Dont Repeat A History Of Combustible Dust Explosions," Oct. 2015. [Online]. Available: https://hughesenv.com/history-of-combustible-dust-explosions/

[5] "NFPA 68: Explosion Protection using Deflagration Venting - IEP Technologies." [Online]. Available: https://www.ieptechnologies.com/knowledge-center/faqs-links/nfpa-68

[6] "Combustible Dust National Emphasis Program (Reissued) | Occupational Safety and Health Administration." [Online]. Available: https://www.osha.gov/enforcement/directives/cpl-03-00-008

[7] G. E. Blomgren, "The Development and Future of Lithium Ion Batteries," *Journal of The Electrochemical Society*, vol. 164, no. 1, pp. A5019–A5025, Jan. 2017. [Online]. Available: http://jes.ecsdl.org/content/164/1/A5019

[8] N. Bensalah and H. Dawoud, "Review on synthesis, characterizations, and electrochemical properties of cathode materials for lithium ion batteries," *Journal of Material Science Engineering*, vol. 5, 01 2016. [Online]. Available: https://www.researchgate.net/publication/307531502_Review_on_Synthesis_Characterizations_and_Electrochemical_Properties_of_Cathode_Materials_for_Lithium_Ion_Batteries

[9] K. Kreder, K. Marr, J. Viegra, K. Stalder, and O. Ezekoye, "Lithium Ion Battery Thermal Hazard and Fire Safety," University of Texas at Austin.

[10] D. W. CNN, "A man dies after his e-cigarette explodes in his face." [Online]. Available: https://www.cnn.com/2019/02/05/health/exploding-vape-pen-death-trnd/index.html

[11] M. Zhou, "Samsung phone catches fire and destroys car, says Detroit woman." [Online]. Available: https://www.cnet.com/news/samsung-phone-catches-fire-destroys-car-says-detroit-woman/

[12] C. Kwan, "HP expands laptop battery recall due to fire and burn hazards." [Online]. Available: https://www.zdnet.com/article/hp-expands-laptop-battery-recall-due-to-fire-and-burn-hazards/

[13] "Chevrolet Volt Battery Incident Overview Report." [Online]. Available: https://www.nhtsa.gov/search

[14] "Tesla fire - Electrek." [Online]. Available: https://electrek.co/guides/tesla-fire/

[15] F. Lambert, "Tesla Model S catches on fire after being towed to a garage, Tesla is investigating," Dec. 2018. [Online]. Available: https://electrek.co/2018/12/19/tesla-model-s-fire-towing/

[16] "Watch a Tesla Model S explode in a parking garage." [Online]. Available: https://futurism.com/the-byte/tesla-fire-shanghai-parking-garage

[17] H. Ranter, "ASN Aircraft accident Boeing 747-44af (SCD) N571up Dubai Airport (DXB)." [Online]. Available: https://aviation-safety.net/database/record.php?id=20100903-0

[18] K. Staff, "Neighborhood residents concerned following train car explosion," Apr. 2017. [Online]. Available: https://www.khou.com/article/news/local/neighborhood-residents-concerned-following-train-car-explosion/285-433810198

[19] S. Beausoleil, "Lithium batteries causes train car explosion in NE Houston," Apr. 2017. [Online]. Available: https://www.click2houston.com/news/train-catches-fire-in-ne-houston

[20] J. Deign, "Engie Investigates Source of Belgian Battery Blaze," Dec. 2017. [Online]. Available: https://www.greentechmedia.com/articles/read/engie-investigates-source-of-belgian-battery-blaze

[21] N. Hyun-woo, "Frequent fire raising concerns over safety of solar energy," Jan. 2019. [Online]. Available: https://www.koreatimes.co.kr/www/tech/2018/12/133_260560.html

[22] "Explosions Threatening Lithium-Ion's Edge in a Battery Race," Apr. 2019. [Online]. Available: https://www.bloomberg.com/news/articles/2019-04-23/explosions-are-threatening-lithium-ion-s-edge-in-a-battery-race

[23] "Injured firefighters identified from substation battery explosion in Surprise | Arizona News | azfamily.com." [Online]. Available: https://www.azfamily.com/news/firefighters-hospitalized-after-power-substation-battery-explosion-in-surprise/article_c28a7f1e-631c-11e9-9bf1-bfa00f273619.html

[24] "Eight AZ Firefighters Hurt, One Critically, in Explosion." [Online]. Available: https://www.firehouse.com/safety-health/news/21077221/eight-az-firefighters-injured-one-critically-in-a-large-utility-battery-explosion

[25] "'Reasons that are still unknown': 30 experts investigate Surprise battery explosion that injured 9." [Online]. Available: https://www.azcentral.com/story/money/business/energy/2019/04/23/arizona-public-service-provides-update-investigation-battery-fire-aps-surprise/3540437002/

[26] H. Mai, "APS storage facility explosion raises questions about battery safety," Apr. 2019. [Online]. Available: https://www.utilitydive.com/news/aps-storage-facility-explosion-raises-questions-about-battery-safety/553540/

[27] "Designing applications with Li-ion batteries - Battery Management | Richtek Technology." [Online]. Available: https://www.richtek.com/battery-management/en/designing-liion.html

[28] "Beckett battery module demonstrates 10-year cycle life." [Online]. Available: https://www.oemoffhighway.com/electronics/press-release/12117948/beckett-battery-module-demonstrates-10year-cycle-life

[29] "Ofgem moves to amend electricity licencing for storage by summer 2018." [Online]. Available: https://www.current-news.co.uk/news/ofgem-moves-to-amend-electricity-licencing-for-storage-by-summer-2018

[30] P. C. Cole and D. R. Conover, "Energy Storage System Safety: Plan Review and Inspection Checklist," Tech. Rep. SAND2017-3066R, 1365458, Mar. 2017. [Online]. Available: http://www.osti.gov/servlets/purl/1365458/

[31] M. J. Hurley, *SFPE Handbook of Fire Protection Engineering*, fifth edition ed. Springer, vol. Volume I.

[32] "Energies | Free Full-Text | Li-Ion Battery Fire Hazards and Safety Strategies." [Online]. Available: https://www.mdpi.com/1996-1073/11/9/2191

[33] P. Cole and D. Conover, "Energy Storage System Guide for Compliance with Safety Codes and Standards," p. 108.

[34] "NFPA 1: Fire Code." [Online]. Available: https://www.nfpa.org/codes-and-standards/all-codes-and-standards/list-of-codes-and-standards/detail?code=1

[35] "NFPA 13: Standard for the Installation of Sprinkler Systems." [Online]. Available: https://www.nfpa.org/codes-and-standards/all-codes-and-standards/list-of-codes-and-standards/detail?code=13

[36] "NFPA 68: Standard on Explosion Protection by Deflagration Venting." [Online]. Available: https://www.nfpa.org/codes-and-standards/all-codes-and-standards/list-of-codes-and-standards/detail?code=68&year=1974

[37] "NFPA 69: Standard on Explosion Prevention Systems." [Online]. Available: https://www.nfpa.org/codes-and-standards/all-codes-and-standards/list-of-codes-and-standards/detail?code=69

[38] "NFPA 70: National Electrical Code." [Online]. Available: https://www.nfpa.org/codes-and-standards/all-codes-and-standards/list-of-codes-and-standards/detail?code=70

[39] "NFPA 72: National Fire Alarm and Signaling Code." [Online]. Available: https://www.nfpa.org/codes-and-standards/all-codes-and-standards/list-of-codes-and-standards/detail?code=72

[40] "nfpa 1620 - Google Search." [Online]. Available: https://www.google.com/search?q=nfpa+1620&oq=nfpa+1620&aqs=chrome..69i57.1709j0j4&sourceid=chrome&ie=UTF-8

[41] "NFPA 855: Standard for the Installation of Stationary Energy Storage Systems." [Online]. Available: https://www.nfpa.org/codes-and-standards/all-codes-and-standards/list-of-codes-and-standards/detail?code=855

[42] "NFPA 5000: Building Construction and Safety Code." [Online]. Available: https://www.nfpa.org/codes-and-standards/all-codes-and-standards/list-of-codes-and-standards/detail?code=5000

[43] "IFC," Mar. 2015. [Online]. Available: https://www.iccsafe.org/codes-tech-support/codes/2018-i-codes/ifc/

[44] "The International Building Code," Mar. 2015. [Online]. Available: https://www.iccsafe.org/codes-tech-support/codes/2018-i-codes/ibc/

[45] "UL - 489 Molded-Case Circuit Breakers, Molded-Case Switches, and Circuit-Breaker Enclosures | Standards Catalog." [Online]. Available: https://standardscatalog.ul.com/standards/en/standard_489_13

[46] "UL - 810a Standard for Electrochemical Capacitors | Standards Catalog." [Online]. Available: https://standardscatalog.ul.com/standards/en/standard_810a_1

[47] "UL - 1642 Standard for Lithium Batteries | Standards Catalog." [Online]. Available: https://standardscatalog.ul.com/standards/en/standard_1642_5

[48] "UL - 1741 Standard for Inverters, Converters, Controllers and Interconnection System Equipment for Use With Distributed Energy Resources | Standards Catalog." [Online]. Available: https://standardscatalog.ul.com/standards/en/standard_1741_2

[49] "UL - 1973 Standard for Batteries for Use in Stationary, Vehicle Auxiliary Power and Light Electric Rail (LER) Applications | Standards Catalog." [Online]. Available: https://standardscatalog.ul.com/standards/en/standard_1973_2

[50] "UL - 9540 Standard for Energy Storage Systems and Equipment | Standards Catalog." [Online]. Available: https://standardscatalog.ul.com/standards/en/standard_9540_1

[51] "UL - 9540a Test Method for Evaluating Thermal Runaway Fire Propagation in Battery Energy Storage Systems | Standards Catalog." [Online]. Available: https://standardscatalog.ul.com/standards/en/standard_9540a_3

[52] "IEEE-SA - The National Electrical Safety Code (NESC)." [Online]. Available: https://standards.ieee.org/products-services/nesc/index.html

[53] "IEEE 1375-1998 - IEEE Guide for the Protection of Stationary Battery Systems." [Online]. Available: https://standards.ieee.org/standard/1375-1998.html

[54] "IEEE 1547-2018 - IEEE Standard for Interconnection and Interoperability of Distributed Energy Resources with Associated Electric Power Systems Interfaces." [Online]. Available: https://standards.ieee.org/standard/1547-2018.html

[55] "IEEE 1679.1-2017 - IEEE Guide for the Characterization and Evaluation of Lithium-Based Batteries in Stationary Applications." [Online]. Available: https://standards.ieee.org/standard/1679_1-2017.html

[56] "IEEE 1635-2012 - IEEE/ASHRAE Guide for the Ventilation and Thermal Management of Batteries for Stationary Applications." [Online]. Available: https://standards.ieee.org/standard/1635-2012.html

[57] "UFC 3-520-05 Stationary Battery Areas, with Change 1 | WBDG - Whole Building Design Guide." [Online]. Available: http://www.wbdg.org/ffc/dod/unified-facilities-criteria-ufc/ufc-3-520-05

[58] Q. Wang, L. Jiang, Y. Yu, and J. Sun, "Progress of enhancing the safety of lithium ion battery from the electrolyte aspect," *Nano Energy*, vol. 55, pp. 93–114, Jan. 2019. [Online]. Available: http://www.sciencedirect.com/science/article/pii/S2211285518307614

[59] F. M. Global, "FM Global conducts new large-scale fire tests on warehoused lithium-ion batteries." [Online]. Available: https://newsroom.fmglobal.com/releases/fm-global-conducts-new-large-scale-fire-tests-on-warehoused-lithium-ion-batteries

[60] C. L. Campion, W. Li, W. B. Euler, B. L. Lucht, B. Ravdel, J. F. DiCarlo, R. Gitzendanner, and K. M. Abraham, "Suppression of Toxic Compounds Produced in the Decomposition of Lithium-Ion Battery Electrolytes," *Electrochemical and Solid-State Letters*, vol. 7, no. 7, pp. A194–A197, Jul. 2004. [Online]. Available: http://esl.ecsdl.org/content/7/7/A194

[61] A. Hammami, N. Raymond, and M. Armand, "Runaway risk of forming toxic compounds," *Nature*, vol. 424, no. 6949, p. 635, Aug. 2003. [Online]. Available: https://www.nature.com/articles/424635b

[62] P. Ribire, S. Grugeon, M. Morcrette, S. Boyanov, S. Laruelle, and G. Marlair, "Investigation on the fire-induced hazards of Li-ion battery cells by fire calorimetry," *Energy & Environmental Science*, vol. 5, no. 1, pp. 5271–5280, Jan. 2012. [Online]. Available: http://pubs.rsc.org/en/content/articlelanding/2012/ee/c1ee02218k

[63] "NFPA - Energy Storage Systems." [Online]. Available: https://www.nfpa.org/News-and-Research/Resources/Emergency-Responders/High-risk-hazards/Energy-Storage-Systems

[64] "Using Foam to Protect WUI Structures." [Online]. Available: http://www.firerescuemagazine.com/articles/print/volume-5/issue-2/wildland-urban-interface/using-foam-to-protect-wui-structures.html

[65] K. Kumai, H. Miyashiro, Y. Kobayashi, K. Takei, and R. Ishikawa, "Gas generation mechanism due to electrolyte decomposition in commercial lithium-ion cell," *Journal of Power Sources*, vol. 81-82, pp. 715–719, Sep. 1999. [Online]. Available: http://linkinghub.elsevier.com/retrieve/pii/S0378775398002341

[66] T. Ohsaki, T. Kishi, T. Kuboki, N. Takami, N. Shimura, Y. Sato, M. Sekino, and A. Satoh, "Overcharge reaction of lithium-ion batteries," *Journal of Power Sources*, vol. 146, no. 1-2, pp. 97–100, Aug. 2005. [Online]. Available: http://linkinghub.elsevier.com/retrieve/pii/S0378775305005112

[67] W. Kong, H. Li, X. Huang, and L. Chen, "Gas evolution behaviors for several cathode materials in lithium-ion batteries," *Journal of Power Sources*, vol. 142, no. 1, pp. 285–291, Mar. 2005. [Online]. Available: http://www.sciencedirect.com/science/article/pii/S037877530401078X

[68] D. H. Doughty, E. P. Roth, C. C. Crafts, G. Nagasubramanian, G. Henriksen, and K. Amine, "Effects of additives on thermal stability of Li ion cells," *Journal of Power Sources*, vol. 146, no. 1, pp. 116–120, Aug. 2005. [Online]. Available: http://www.sciencedirect.com/science/article/pii/S0378775305005057

[69] D. Abraham, E. Roth, R. Kostecki, K. McCarthy, S. MacLaren, and D. Doughty, "Diagnostic examination of thermally abused high-power lithium-ion cells," *Journal of Power Sources*, vol. 161, no. 1, pp. 648–657, Oct. 2006. [Online]. Available: https://linkinghub.elsevier.com/retrieve/pii/S0378775306006768

[70] E. P. Roth, "Abuse Response of 18650 Li-Ion Cells with Different Cathodes Using EC:EMC/LiPF6 and EC:PC:DMC/LiPF6 Electrolytes," *ECS Transactions*, vol. 11, no. 19, pp. 19–41, Mar. 2008. [Online]. Available: http://ecst.ecsdl.org/content/11/19/19

[71] V. Somandepalli, K. Marr, and Q. Horn, "Quantification of Combustion Hazards of Thermal Runaway Failures in Lithium-Ion Batteries," *SAE International Journal of Alternative Powertrains*, vol. 3, pp. 98–104, May 2014.

[72] A. W. Golubkov, D. Fuchs, J. Wagner, H. Wiltsche, C. Stangl, G. Fauler, G. Voitic, A. Thaler, and V. Hacker, "Thermal-runaway experiments on consumer Li-ion batteries with metal-oxide and olivin-type cathodes," *RSC Advances*, vol. 4, no. 7, pp. 3633–3642, 2014. [Online]. Available: https://pubs.rsc.org/en/content/articlelanding/2014/ra/c3ra45748f

[73] F. Larsson, P. Andersson, P. Blomqvist, A. Lorn, and B.-E. Mellander, "Characteristics of lithium-ion batteries during fire tests," *Journal of Power Sources*, vol. 271, pp. 414–420, Dec. 2014. [Online]. Available: http://www.sciencedirect.com/science/article/pii/S0378775314012828

[74] N. S. Spinner, C. R. Field, M. H. Hammond, B. A. Williams, K. M. Myers, A. L. Lubrano, S. L. Rose-Pehrsson, and S. G. Tuttle, "Physical and chemical analysis of lithium-ion battery cell-to-cell failure events inside custom fire chamber," *Journal of Power Sources*, vol. 279, pp. 713–721, Apr. 2015. [Online]. Available: http://www.sciencedirect.com/science/article/pii/S0378775315000804

[75] Y. Fu, S. Lu, K. Li, C. Liu, X. Cheng, and H. Zhang, "An experimental study on burning behaviors of 18650 lithium ion batteries using a cone calorimeter," *Journal of Power Sources*, vol. 273, pp. 216–222, Jan. 2015. [Online]. Available: http://www.sciencedirect.com/science/article/pii/S0378775314014475

[76] Q. Yuan, F. Zhao, W. Wang, Y. Zhao, Z. Liang, and D. Yan, "Overcharge failure investigation of lithium-ion batteries," *Electrochimica Acta*, vol. 178, pp. 682–688, Oct. 2015. [Online]. Available: http://www.sciencedirect.com/science/article/pii/S0013468615302140

[77] A. W. Golubkov, S. Scheikl, R. Planteu, G. Voitic, H. Wiltsche, C. Stangl, G. Fauler, A. Thaler, and V. Hacker, "Thermal runaway of commercial 18650 Li-ion batteries with LFP and NCA cathodes impact of state of charge and overcharge," *RSC Advances*, vol. 5, no. 70, pp. 57 171–57 186, Jun. 2015. [Online]. Available: http://pubs.rsc.org/en/content/articlelanding/2015/ra/c5ra05897j

[78] J. Sun, J. Li, T. Zhou, K. Yang, S. Wei, N. Tang, N. Dang, H. Li, X. Qiu,

and L. Chen, "Toxicity, a serious concern of thermal runaway from commercial Li-ion battery," *Nano Energy*, vol. 27, pp. 313–319, Sep. 2016. [Online]. Available: http://www.sciencedirect.com/science/article/pii/S2211285516302130

[79] Y. Zheng, K. Qian, D. Luo, Y. Li, Q. Lu, B. Li, Y.-B. He, X. Wang, J. Li, and F. Kang, "Influence of over-discharge on the lifetime and performance of LiFePO4/graphite batteries," *RSC Advances*, vol. 6, no. 36, pp. 30 474–30 483, Mar. 2016. [Online]. Available: http://pubs.rsc.org/en/content/articlelanding/2016/ra/c6ra01677d

[80] T. Maloney, "Home : FAA Fire Safety," Oct. 2016. [Online]. Available: https://www.fire.tc.faa.gov/systems/lithium-batteries

[81] M. Lammer, A. Knigseder, and V. Hacker, "Holistic methodology for characterisation of the thermally induced failure of commercially available 18650 lithium ion cells," *RSC Advances*, vol. 7, no. 39, pp. 24 425–24 429, May 2017. [Online]. Available: http://pubs.rsc.org/en/content/articlelanding/2017/ra/c7ra02635h

[82] F. Larsson, P. Andersson, P. Blomqvist, and B.-E. Mellander, "Toxic fluoride gas emissions from lithium-ion battery fires," *Scientific Reports*, vol. 7, no. 1, p. 10018, Aug. 2017. [Online]. Available: https://www.nature.com/articles/s41598-017-09784-z

[83] Y. Fernandes, A. Bry, and S. de Persis, "Identification and quantification of gases emitted during abuse tests by overcharge of a commercial Li-ion battery," *Journal of Power Sources*, vol. 389, pp. 106–119, Jun. 2018. [Online]. Available: https://linkinghub.elsevier.com/retrieve/pii/S0378775318302581

[84] D. G. Goodwin, H. K. Moffat, and R. L. Speth, "Cantera: An Object-Oriented Software Toolkit For Chemical Kinetics, Thermodynamics, And Transport Processes. Version 2.3.0," Jan. 2017.

[85] M. Frenklach, T. Bowman, and G. Smith, "GRI-MECH." [Online]. Available: http://www.me.berkeley.edu/gri_mech/

[86] H. Le Chatelier, "Estimation of firedamp by flammability limits," *Annals of Mines*, vol. 19, no. 8, pp. 388–395, 1891.

[87] J. G. Quintiere, "Fundamentals of Fire Phenomena," in *Fundamentals of Fire Phenomena*. John Wiley & Sons, 2006, pp. 77–115.

[88] I. A. Zlochower, "Experimental flammability limits and associated theoretical flame temperatures as a tool for predicting the temperature dependence of these limits," *Journal of loss prevention in the process industries*, vol. 25, no. 3, pp. 555–560, May 2012. [Online]. Available: https://www.ncbi.nlm.nih.gov/pmc/articles/PMC4676578/

[89] H. Le, Y. Liu, and M. S. Mannan, "Lower Flammability Limits of Hydrogen and Light Hydrocarbons at Subatmospheric Pressures," *Industrial & Engineering Chemistry Research*, vol. 52, no. 3, pp. 1372–1378, Jan. 2013. [Online]. Available: https://doi.org/10.1021/ie302504h

[90] T. Ma, "A thermal theory for estimating the flammability limits of a mixture," *Fire Safety Journal*, vol. 46, no. 8, pp. 558–567, Nov. 2011. [Online]. Available: http://www.sciencedirect.com/science/article/pii/S0379711211001263

[91] O. US EPA, "Review & Peer Review of Parameters for Properly Designed and Operated Flares Documents," Jun. 2016. [Online]. Available: https://www.epa.gov/stationary-sources-air-pollution/review-peer-review-parameters-properly-designed-and-operated-flares

[92] G. W. Jones, *Inflammability of mixed gases /*. Washington, D.C. :, 1929. [Online]. Available: http://hdl.handle.net/2027/mdp.39015078543314

[93] R. Bounaceur, P.-A. Glaude, B. Sirjean, R. Fournet, P. Montagne, M. Vierling, and M. Molire, "Prediction of Flammability Limits of Gas Mixtures Containing Inert Gases Under Variable Temperature and Pressure Conditions." American Society of Mechanical Engineers, Jun. 2017, pp. V04AT04A072–V04AT04A072. [Online]. Available: https://proceedings.asmedigitalcollection.asme.org/proceeding.aspx?articleid=2649966

[94] M. Terpstra, "Flammability limits of hydrogen-diluent mixtures in air," Thesis,

University of Calgary, Aug. 2012. [Online]. Available: https://prism.ucalgary.ca/handle/11023/164

[95] M. Vidal, W. Wong, W. J. Rogers, and M. S. Mannan, "Evaluation of lower flammability limits of fuelairdiluent mixtures using calculated adiabatic flame temperatures," *Journal of Hazardous Materials*, vol. 130, no. 1, pp. 21–27, Mar. 2006. [Online]. Available: http://www.sciencedirect.com/science/article/pii/S0304389405004218

[96] F. Zhao, "_USInert Gas Dilution Effect on the Flammability Limits of Hydrocarbon Mixtures," Thesis, Feb. 2012. [Online]. Available: https://oaktrust.library.tamu.edu/handle/1969.1/ETD-TAMU-2011-12-10569

[97] M. Huth and A. Heilos, *Modern Gas Turbine Systems*. Woodhead Publishing, 2013. [Online]. Available: https://www.sciencedirect.com/topics/chemistry/laminar-flame

[98] V. Jain, "Slow and Fast Hydrogen Deflagration A validation study," Thesis, Delft University of Technology, Oct. 2013. [Online]. Available: https://d1rkab7tlqy5f1.cloudfront.net/LR/Organisatie/Afdelingen/Aerodynamics__Wind_Energy__Flight_Performance_and_Propulsion/Aerodynamics/MSc_Theses/2013/Jain__V..pdf

[99] P. Dirrenberger, H. Le Gall, R. Bounaceur, O. Herbinet, P.-A. Glaude, A. Konnov, and F. Battin-Leclerc, "Measurements of Laminar Flame Velocity for Components of Natural Gas," *Energy and Fuels*, vol. 25, no. 9, pp. 3875–3884, 2011. [Online]. Available: https://hal.archives-ouvertes.fr/hal-00776646

[100] M. C. Krejci, O. Mathieu, A. J. Vissotski, S. Ravi, T. G. Sikes, E. L. Petersen, A. Krmons, W. Metcalfe, and H. J. Curran, "Laminar Flame Speed and Ignition Delay Time Data for the Kinetic Modeling of Hydrogen and Syngas Fuel Blends," *Journal of Engineering for Gas Turbines and Power*, vol. 135, no. 2, pp. 021 503–021 503–9, Jan. 2013. [Online]. Available: http://dx.doi.org/10.1115/1.4007737

[101] J. Johnplass, M. Henriksen, K. Vaagsaether, J. Lundberg, and D. Bjerketvedt,

"Simulation of burning velocities in gases vented from thermal run-a-way lithium ion batteries," *Linkping University Electronic Press*, no. 138, pp. 157–161, Sep. 2017.

[102] T. Hirasawa, C. Sung, A. Joshi, Z. Yang, H. Wang, and C. Law, "Determination of laminar flame speeds using digital particle image velocimetry: Binary Fuel blends of ethylene, n-Butane, and toluene," *Proceedings of Combustion Institute*, vol. 29, no. 2, pp. 1427–1434, 2002.

[103] A. Kelley, A. Smallbone, D. Zhu, and C. Law, "Laminar flame speeds of C5 to C8n-alkanes at elevated pressures: Experimental determination, fuel similarity, and stretch sensitivity," *Proceedings of Combustion Institute*, vol. 33, no. 1, pp. 963–970, 2011.

[104] D. Li, Q. Zhang, Q. Ma, and S. Shen, "Comparison of explosion characteristics between hydrogen/air and methane/air at the stoichiometric concentrations," *International Journal of Hydrogen Energy*, vol. 40, no. 28, pp. 8761–8768, Jul. 2015. [Online]. Available: http://www.sciencedirect.com/science/article/pii/S0360319915011829

[105] F. Wu and G. Yushin, "Conversion cathodes for rechargeable lithium and lithium-ion batteries," *Energy & Environmental Science*, vol. 10, no. 2, pp. 435–459, Feb. 2017. [Online]. Available: http://pubs.rsc.org/en/content/articlelanding/2017/ee/c6ee02326f

[106] T. Skjold, H. Hisken, S. Lakshmipathy, G. Atanga, L. Bernard, M. van Wingerden, K. L. Olsen, M. N. Holme, N. M. Tury, M. Mykleby, and K. van Wingerden, "Vented hydrogen deflagrations in containers: Effect of congestion for homogeneous and inhomogeneous mixtures," *International Journal of Hydrogen Energy*, vol. 44, no. 17, pp. 8819–8832, Apr. 2019. [Online]. Available: http://www.sciencedirect.com/science/article/pii/S0360319918331598

[107] C. M. R. Vendra and J. X. Wen, "Vented hydrogen deflagations in an ISO container," Hamburg, Germany, Jun. 2017. [Online]. Available: https://www.hysafe.info/ichs2017/

[108] D. Bjerketvedt, J. R. Bakke, and K. van Wingerden, "Gas explosion handbook," *Journal of Hazardous Materials*, vol. 52, no. 1, pp. 1–150, Jan. 1997. [Online]. Available: http://www.sciencedirect.com/science/article/pii/S0304389497816202

[109] "Explosion Vents & Pressure Relief | Suppression | Fire Protection Technologies." [Online]. Available: http://www.fire-protection.com.au/product-menu/explosion-protection/pressure-relief-vents

[110] A. M. Nainna, H. N. Phylaktou, and G. E. Andrews, "Effects of Obstacle Separation Distance on Gas Explosions: The Influence of Obstacle Blockage Ratio," *Procedia Engineering*, vol. 84, pp. 306–319, Jan. 2014. [Online]. Available: http://www.sciencedirect.com/science/article/pii/S1877705814017603

[111] B. Ditch, "UPDATE: DEVELOPMENT OF SPRINKLER PROTECTION FOR LIB ENERGY STORAGE SYSTEMS," Nov. 2018. [Online]. Available: https://www.nfpa.org/-/media/Files/News-and-Research/Resources/Research-Foundation/Symposia/2018-SUPDET/Presentations/SUPDET2018Ditch.ashx?la=en

[112] "Firefighters Drop Smoking BMW i8 Into a Giant Tub of Water." [Online]. Available: https://jalopnik.com/firefighters-drop-smoking-bmw-i8-into-a-giant-tub-of-wa-1833582453

[113] "First Responders | Tesla." [Online]. Available: https://www.tesla.com/firstresponders

[114] W. Chow and S. Han, "(16) Heat release rate calculation in oxygen consumption calorimetry | Request PDF," 2011. [Online]. Available: https://www.researchgate.net/publication/251667490_Heat_release_rate_calculation_in_oxygen_consumption_calorimetry

[115] J. Lindholm, A. Brink, and M. Hupa, "CONE CALORIMETER A TOOL FOR MEASURING HEAT RELEASE RATE," 2009.

[116] "Fire Testing Technology | Cone Calorimeter." [Online]. Available: http://www.fire-testing.com/cone-calorimeter-dual

[117] V. Somandepalli and H. Biteau, "Cone Calorimetry as a Tool for Thermal Hazard Assessment of Li-Ion Cells," *SAE International Journal of Alternative Powertrains*, vol. 3, no. 2, pp. 222–233, 2014. [Online]. Available: https://www.jstor.org/stable/26169055

[118] "Reports:FAA Fire Safety." [Online]. Available: https://www.fire.tc.faa.gov/reports/listresults.asp?searchList=DOT%2FFAA%2FTC-TN15%2F17

[119] X. Liu, S. I. Stoliarov, M. Denlinger, A. Masias, and K. Snyder, "Comprehensive calorimetry of the thermally-induced failure of a lithium ion battery," *Journal of Power Sources*, vol. 280, pp. 516–525, Apr. 2015. [Online]. Available: http://www.sciencedirect.com/science/article/pii/S037877531500141X

[120] X. Liu, Z. Wu, S. I. Stoliarov, M. Denlinger, A. Masias, and K. Snyder, "Heat release during thermally-induced failure of a lithium ion battery: Impact of cathode composition," *Fire Safety Journal*, vol. 85, pp. 10–22, Oct. 2016. [Online]. Available: http://www.sciencedirect.com/science/article/pii/S0379711216301023

[121] P. Ping, Q. Wang, P. Huang, K. Li, J. Sun, D. Kong, and C. Chen, "Study of the fire behavior of high-energy lithium-ion batteries with full-scale burning test," *Journal of Power Sources*, vol. 285, Jul. 2015.

[122] F. Larsson, J. Anderson, P. Andersson, and B.-E. Mellander, "Thermal Modelling of Cell-to-Cell Fire Propagation and Cascading Thermal Runaway Failure Effects for Lithium-Ion Battery Cells and Modules Using Fire Walls," *Journal of The Electrochemical Society*, vol. 163, no. 14, pp. A2854–A2865, Jan. 2016. [Online]. Available: http://jes.ecsdl.org/content/163/14/A2854

[123] "ASTM E1354-17: Standard Test Method for Heat and Visible Smoke Release Rates for Materials and Products Using an Oxygen Consumption Calorimeter," 2017. [Online]. Available: https://www.astm.org/Standards/E1354.htm

[124] D. D. MacNeil and J. R. Dahn, "The Reaction of Charged Cathodes with Nonaqueous Solvents and Electrolytes: I. Li0.5coo2," *Journal of The Electrochemical*

Society, vol. 148, no. 11, pp. A1205–A1210, Nov. 2001. [Online]. Available: http://jes.ecsdl.org/content/148/11/A1205

[125] J.-i. Yamaki, Y. Baba, N. Katayama, H. Takatsuji, M. Egashira, and S. Okada, "Thermal stability of electrolytes with LixCoO2 cathode or lithiated carbon anode," *Journal of Power Sources*, vol. 119-121, pp. 789–793, Jun. 2003. [Online]. Available: http://www.sciencedirect.com/science/article/pii/S0378775303002544

[126] Q. Wang, P. Ping, X. Zhao, G. Chu, J. Sun, and C. Chen, "Thermal runaway caused fire and explosion of lithium ion battery," *Journal of Power Sources*, vol. 208, pp. 210–224, Jun. 2012. [Online]. Available: http://www.sciencedirect.com/science/article/pii/S0378775312003989

[127] R. Zalosh, "Flammable Gas and Vapor Explosions," in *SFPE Handbook of Fire Protection Engineering*, M. J. Hurley, D. Gottuk, J. R. Hall, K. Harada, E. Kuligowski, M. Puchovsky, J. Torero, J. M. Watts, and C. Wieczorek, Eds. New York, NY: Springer New York, 2016, pp. 2738–2765. [Online]. Available: https://doi.org/10.1007/978-1-4939-2565-0_69

[128] "1.3.6.7.2. Critical Values of the Student's-t Distribution." [Online]. Available: https://www.itl.nist.gov/div898/handbook/eda/section3/eda3672.htm

[129] W. Zhang, X. Chen, Q. Chen, C. Ding, J. Liu, M. Chen, and J. Wang, "Combustion calorimetry of carbonate electrolytes used in lithium ion batteries," *Journal of Fire Sciences*, vol. 33, no. 1, pp. 22–36, Jan. 2015. [Online]. Available: https://doi.org/10.1177/0734904114550789

[130] R. N. Walters, S. M. Hackett, and R. E. Lyon, "Heats of combustion of high temperature polymers," *Fire and Materials*, vol. 24, no. 5, pp. 245–252, 2000. [Online]. Available: http://onlinelibrary.wiley.com/doi/abs/10.1002/1099-1018%28200009/10%2924%3A5%3C245%3A%3AAID-FAM744%3E3.0.CO%3B2-7

[131] A. H. Buchanan and A. K. Abu, "Fires and Heat," in *Structural Design for Fire Safety*, 2nd ed. John Wiley & Sons, Ltd, 2016, pp. 35–83. [Online]. Available: http://onlinelibrary.wiley.com/doi/abs/10.1002/9781118700402.ch3

[132] E. ToolBox, "Densities of Solids," 2009. [Online]. Available: https://www.engineeringtoolbox.com/density-solids-d_1265.html

[133] D. H. Doughty and E. P. Roth, "A General Discussion of Li Ion Battery Safety," *The Electrochemical Society Interface*, vol. 21, no. 2, pp. 37–44, Jan. 2012. [Online]. Available: http://interface.ecsdl.org.ezproxy.lib.utexas.edu/content/21/2/37

[134] Y. Hua, M. Xu, M. Li, C. Ma, and C. Zhao, "Estimation of State of Charge for Two Types of Lithium-Ion Batteries by Nonlinear Predictive Filter for Electric Vehicles," *Energies*, vol. 8, no. 5, pp. 3556–3577, May 2015. [Online]. Available: https://www.mdpi.com/1996-1073/8/5/3556

Vita

Austin Ronald Baird was born in Albuquerque, NM. In 2017 he graduated from the University of New Mexico with his B.S.M.E with a minor in mathematics. Austin began his career at Sandia National Laboratories over seven years ago. During high school, he interned at SNL as a facilities student intern working with HVAC and fire protection maintenance personnel. Throughout his time working on his undergraduate degree, he interned for the facilities mechanical engineering department and fire protection engineering departments. One of his projects was to study building air filtration to help determine performance-based change out frequencies. He published some of this work in 2017 while graduating under the guidance of Dr. Peter Vorbieff from UNM and Casiano Armenta from SNL. At the same time, he worked under Dr. John Russell and Mr. Mike Arnold as the chief systems engineer for LOBOmotorsports as part of the UNM FSAE program. Upon graduating, he transitioned to a critical skills masters student at SNL. Through that program, he began working on his M.S.M.E. at the University of Texas at Austin in the UT Fire Research Group under the guidance of Dr. Ofodike Ezekoye and Dr. Kevin Marr. There he studied battery energy storage systems to help characterize and understand the associated hazards. Upon graduation, Austin will return to Sandia National Laboratories to work and pursue his professional engineering license.

Austin's Email Address: arbaird@sandia.gov

This thesis was typed by Austin Ronald Baird.